SEARCHING FOR GRAVITATIONAL-WAVES FROM COMPACT BINARY COALESCENCES WHILE DEALING WITH CHALLENGES OF REAL DATA AND SIMULATED WAVEFORMS

By

WADUTHANTHREE THILINA DAYANGA

A dissertation submitted in partial fulfillment of
the requirements for the degree of

DOCTOR OF PHILOSOPHY

WASHINGTON STATE UNIVERSITY
Department of Physics and Astronomy

DECEMBER 2013

To the Faculty of Washington State University:

    The members of the Committee appointed to examine the dissertation of WADUTHANTHREE THILINA DAYANGA find it satisfactory and recommend that it be accepted.

                            _____-
                            Sukanta Bose, Ph.D., Chair

                            _____-
                            Matthew Duez, Ph.D.

                            _____-
                            Gregory Mendell, Ph.D.

                            _____-
                            Guy Worthey, Ph.D.

work.

SEARCHING FOR GRAVITATIONAL-WAVES FROM COMPACT BINARY

COALESCENCES WHILE DEALING WITH CHALLENGES

OF REAL DATA AND SIMULATED WAVEFORMS

Abstract

by Waduthanthree Thilina Dayanga, Ph.D.
Washington State University
December 2013

Chair: Sukanta Bose

Albert Einstein's general theory of relativity predicts the existence of gravitational waves (GWs). Direct detection of GWs will provide new information about physics, astronomy and cosmology. In this thesis we focus on the quest for detecting GWs from compact binary coalescence (CBC) systems. Since CBC waveforms are accurately modelled and because CBCs result from the motion of large compact masses and, thus, can be seen to great distances, they are the most promising source for the first direct detection of GWs.

In this thesis we address several challenges associated with detecting CBC signals buried in ground-based GW detector data that were experienced in past searches and are anticipated for future searches. The data analysis techniques we employ to detect GW signals assume that detector noise is Gaussian and stationary. However, in reality, it is neither Gaussian nor stationary. To estimate the performance loss due to these deviations from ideal conditions, we compare the efficiencies of detecting CBC signals in simulated Gaussian data with that in real

data.

As we move towards the advanced detector era, to begin in 2015, it is important to be prepared for future CBC searches. In this thesis we investigate the performances of non-spinning binary black hole searches in simulated Gaussian data using advanced detector noise curves predicted for 2015-2016. In the same study, we analyze the GW detection probabilities of the latest post-Newtonian-Numerical-Relativity hybrid waveforms submitted to the second edition of the Numerical Injection Analysis project.

Many authors suggested and demonstrated that coherent searches are the most optimal in detecting GW signals when using a network of detectors. Owing to computational expenses in recent searches of LIGO and Virgo we did not employ coherent search methods. In this thesis we demonstrate how to employ coherent searches for current CBC searches in a computationally feasible way. Additionally, we thoroughly investigate many aspects of coherent searches using an all-sky, all-time hierarchical coherent search pipeline. Most importantly we present some powerful insights extracted from running the this pipeline on LIGO-Virgo data. This also includes the challenges we need to address before moving to fully coherent searches.

To my daughter Thihansa, wife Darshani and my parents...

PREFACE

The thesis focuses on the efforts to detect gravitational waves from compact binary coalescences using LIGO and Virgo interferometer data. The work presented in this thesis stems from my participation in the LIGO Scientific Collaboration (LSC) and the second version of Numerical Injection Analysis (NINJA-2) Collaboration. This work does not reflect the scientific opinion of the LSC and it was not reviewed by the collaboration.

The mathematical form of the blind hierarchical coherent search pipeline presented in chapter 2 is based on:

Bose, S., Dayanga, T., Ghosh, S., and Talukder, D., "A blind hierarchical coherent search for gravitational-wave signals from coalescing compact binaries in a network of interferometric detectors," Class. Quantum Grav., 28, 134009 (2011)

Chapter 3 is based on results presented in:

Dayanga, T., and Bose, S., "Preparations for detecting and characterizing gravitational-wave signals from binary black hole coalescences," arXiv:1311.4986 (2013)

Chapter 4 is based on results presented in:

The LIGO Scientific Collaboration, The Virgo Scientific Collaboration and The NINJA-2 Collaboration, "The NINJA-2 project: Detecting and characterizing gravitational wave signals from numerical binary black hole simulation," LIGO-P1300199 (2013)

Chapter 5 is based on results presented in:

Abadie, J. et al., "Search for Gravitational Waves from Low Mass Compact Binary Coalescence in LIGO's Sixth Science Run and Virgo's Science Runs 2 and 3," Phys. Rev., D85, 082002 (2012)

and

Aasi, J. et al., "Search for Gravitational Waves from Binary Black Hole Inspiral, Merger and Ringdown in LIGO-Virgo Data from 2009-2010," Phys. Rev., D87, 022002 (2013)

The results related to blind injection recovery presented in chapter 5 is a collaborative work between the author and Sukanta Bose.

The author was one of the data analyst on multiple fortnights of this data, and contributed to data quality studies and the results presented therein.

Contents

List of Figures

List of Tables

Chapter 1

Introduction

1.1 Gravitational-waves

Albert Einstein's general theory of relativity (GR) predicts the existence of gravitational waves (GWs)[12, 13]. Gravitational waves are fluctuations in the curvature of space-time that propagate with the speed of light. Einstein's theory predicts that two massive objects revolving around each other in bound orbits, such as binary neutron stars (BNSs), binary black holes (BBHs) or neutron star black hole (NSBH), emit gravitational radiation. Gravitational waves carry away energy, momentum, and angular momentum at the expense of the orbital decay of the binary, thereby causing the stars to gradually spiral towards each other and giving rise to increasingly shorter wave periods. This anticipated decrease of the orbital period of a binary pulsar was first observed in PSR 1913+16 by Hulse and Taylor [14]. The observation matched the predictions of general theory of relativity to within 2%. As a result the Nobel Prize for Physics in 1993 was awarded to Hulse and

Taylor. This and subsequent discoveries of double neutron star systems remain the strongest indirect evidence for the existence of GWs.

The direct detection of GWs is yet to happen and will open a new window on to the universe. The GW spectrum of observations will unravel an entirely new set of phenomena that will complement those discovered via the electromagnetic (EM) spectrum.

Gravitational wave amplitude is inversely proportional to the distance from the source. The very weak interaction of GW with matter allows to travel very large distances with little any absorption or distortion. While this feature is helful in extracting information from GWs that are coming from cosmological distances, nevertheless at the same time this will make the direct detection very challenging for the current GW detectors. The direct detection of GWs will allow us to explore regions of the universe that are not accessible to optical telescopes, radio antennas and other electromagnetic detectors or particle detectors. Furthermore it will also open avenues to study properties of black holes, equation of state of neutron starts, strong gravity regions of the universe etc. Joint detection of GW with EM radiation can also play critical role by providing enough information to understand the progenitors of short-hard gamma-ray bursts (GRBs) [15].

1.2 Gravitational-wave Detectors

The main challenge in the direct detection of GWs is the extraordinarily small effect that GWs produce in a detector. First attempts to detect GWs used bar detectors introduced by Joseph Weber [16]. The most sensitive detectors today are in-

terferometric detectors. There are two such detectors located in the United States of America, which belong to what is known as the Laser Interferometer Gravitational Wave Observatory (LIGO), in Richland, WA and Livingston, LA [17]. In addition to these there is a French-Italian detector called Virgo located at Cascina, Italy [18]. Both LIGO detectors have arm lengths of 4 km and Virgo has arm length of 3 km. To-date LIGO has completed six science runs and Virgo participated in three science runs. The fifth Science run of LIGO had design sensitivity of what is known, as *initial* LIGO and the latest (sixth) run S6 reached sensitivity termed as *enhanced* LIGO. The fifth Science run (S5) lasted from November 2005 to September 2007. While Virgo's first science run (VSR1) overlapped with LIGO S5, latest two runs VSR2 and VSR3 overlapped with LIGO's S6 run. Both LIGO and Virgo detectors are expected to come back on-line in the near future (2015-2016) with advanced detector technologies in place [19]. Additionally, there is a 600 m interferometer located near Hannover, in Germany called GEO600. The Japanese detector KAGRA and the LIGO-India detector are also expected to operate as advanced detectors in the next few to several years.

1.3 Sources of Gravitational Waves

Depending on their nature GW signals can be divided into four main categories. Our ability to model the waveform from compact binary coalescence (CBC) makes them the most promising source for direct detection of GWs. Sources such as core-collapse supernovae and long duration Gamma-Ray Bursts (GRBs) that produce transient GW signals are not modelled well enough to enable us to predict

their GW waveforms with the desired accuracy. This category of signals is known as *Burst* signals. Additionally it is possible to detect GWs from sources such as Pulsars or spinning non-asymmetric neutron stars that make *Continuous* GW signals. Final category comprises *Stochastic* the signals coming from early universe. Based on this categorization data analysis sub-groups of LIGO-Virgo Collaboration (LVC) also search for four different type of sources in their data analysis efforts. The work presented in this thesis focuses on GW signals from CBCs. The author participated in both *highmass* and *lowmass* searches of latest LIGO-Virgo signal searches. The lowmass analysis searches for GW signals from BNS, BBH and NS-BH sources with total mass between $2M_\odot$ and $25M_\odot$. The highmass analysis searches for GW signals from total mass of $25M_\odot$ to $100M_\odot$ [9, 7].

1.4   Searching for Gravitational Waves

Owing to very small amplitudes of GWs, detecting such a signal in the presence of interferometer noise is challenging. Although we use signal detection techniques based on Gaussian and stationary data models, real detector noise is far from that. With every science run, over the last several years, search methods for CBC detection algorithms have significantly improved. This thesis presents some results from the latest science runs of LIGO and Virgo detectors. These runs used LIGO, Virgo CBC *ihope* search pipeline [20] as the primary search algorithm and software. The ihope pipeline first analyses data from GW detectors individually, followed by identification of coincidences of triggers from the different detectors in end-time, mass and amplitude of the GW signal using a method that

checks for overlapping ellipsoids in the 3D parameter space for the two masses and the end-time [21]. Due to nature of this algorithm it is also known as a *coincident* search. Theoretically, a *coherent* search is expected to be the most sensitive analysis technique for GW signals. The coherent search method and results have been presented by many authors in searching for variety of GW sources [22, 23, 24, 25, 26, 27, 8, 28, 29, 30, 31, 32, 33]. Unlike in coincident searches, a coherent search combines data streams from all detectors before searching for GW signals. Owing to the demand of a larger computational power by the latter, many data analysis groups have employed a coincident search method in past searches especially when no prior information about the source is available.

To achieve higher detection efficiency in advanced detector era (ADE) searches it is important to run all-sky all-time fully coherent searches. Although coincident searches can achieve sensitivity of such "blind" coherent searches for some cases, in general this will not be the case. To study the effect of coherent searches with available computational resources, we introduced a hierarchical version of a coherent search that runs as an addition to the ihope coincident search pipeline [8]. This way the coherent part of the search pipeline analyses only the GW triggers passed by the coincident test and, therefore, is computationally feasible.

Recent efforts of coherent searches for GRBs showed promising results motivating us to continue developing all-sky all-time hierarchical coherent searches for CBC GW signals [24, 33]. This thesis reports results from the first large scale GW simulation study conducted employing the blind hierarchical coherent search pipeline. In the same study we identify the main challenges of all-sky all-time coherent searches with GW simulation studies. Previous studies focused more on

5

developing methods than studying large scale simulations [8]. Additionally we present how much of a performance improvement can be gained with fully coherent searches in the early advanced detector era. Another advantage of coherent searches is that they allow us to combine data streams of different detectors such way that GW signal cancel in the combination. This is also known as the *null-stream* [34]. In this work we study the use of null-stream as a multi-detector signal consistency test. Our results show promise for the possibility of using null-stream in other related areas such as GW trigger clustering algorithms and data quality studies.

One important feature to note is that, we used public GW waveforms submitted in the second version of the Numerical Injection Analysis (NINJA-2) project for our simulation studies of the coherent search pipeline. This allowed us to study the systematics between NINJA-2 waveforms and waveforms available in current LIGO Algorithm Library (LAL) such as *Effective One Body-Numerical Relativity* (EOBNR) and Phenomenological waveforms [35]. In addition to studies related to the coherent searches this thesis also presents overview of the results of LIGO's S6 and Virgo's VSR2/3 low and highmass searches [9, 7]. We also present some results from parameter estimation studies conducted in Gaussian and stationary data. Moving towards the next phase of ground-based GW searches, parameter estimation will play an important role for joint GW detection plans such as GW-EM searches. Fast and accurate parameter estimation will help to localize the source and make a joint GW detection possible.

Although some of the results presented in the next few chapters are based on simulated Gaussian and stationary data, they played a critical role in identifying

important issues and challenges confronting future all-sky all-time fully coherent searches. One key feature of the hierarchical coherent search is that it uses data from all detectors even if it is a subset of them that produces an event in the coincident pipeline and regardless of the Signal Noise Ratios (SNRs) of the triggers in the individual detectors. This allows one to include information about even those GW triggers that did not pass the matched filtering step in the coincident search owing to the presence of SNR thresholds.

1.5 Thesis layout

The layout of this thesis is as follows. In Chapter 2 we introduce basic data analysis techniques used for CBC searches. Here we present the main data analysis pipeline, namely, *ihope,* employed for examining recent LIGO Virgo Science data. Additionally, we present the fundamentals of multi-detector coherent searches and details of that algorithm. In most of our studies presented here we use both of the above ideas to build the blind hierarchical coherent data analysis pipeline.

In chapter 3 we present main results of running the blind hierarchical coherent pipeline and original ihope pipeline together on Gaussian and stationary data with GW simulation signals submitted to the NINJA-2 public waveform catalog. One main feature of this analysis is the use of early advanced LIGO and early advanced Virgo noise curves, as predicted, to generate Gaussian data sets. In addition for direct comparison of coincident and coherent pipelines we compare the performance of different waveform families such as the EOBNR and latest post Newtonian-Numerical Relativity (pN-NR) hybrid waveforms submitted to the

NINJA-2 project. Parameter estimation of the GW sources is as important as detecting them. Therefore this chapter also presents parameter estimation results for pN-NR hybrid waveforms based on maximum likelihood method [22, 23].

Chapter 4 focuses on one of the main exercises of the NINJA-2 binary black hole project, namely, the NINJA-2 mock data challenge [6, 36]. The author was one of the lead analysts of this work and focused on the highmass ihope search part of the project. This chapter presents details of the analysis starting from NINJA-2 waveforms. The data analysis pipeline used here was very similar to the version used in recent highmass search of LIGO Virgo data. The parameters of the simulated blind injections signals used in these data sets are presented here and compared with the results obtained by running the highmass version of the ihope pipeline. As the last part of the analysis we present the background estimation method used for this analysis.

In chapter 5 we summarize the results of LIGO S6 and Virgo VSR2/3 lowmass and highmass results. Two different searches focused on making direct detection of GWs of lower and higher masses, respectively, are determined by the total mass of the binary system. Despite not making direct detection in either analyses there were important developments in the data analysis software and techniques. Also this analysis was very important in identifying potential issues moving towards ADE.

Finally in chapter 6 we discuss main hurdles we needed to overcome in building the blind hierarchical coherent analysis. However, the studies presented in this thesis will be very helpful in building all-sky all-time fully coherent searches. Also we discuss other future improvements that can be made to CBC searches to

enhance the detection probabilities.

Chapter 2

Searching for Gravitational Waves from Compact Binary Coalescences

2.1 Introduction

Interferometric GW detectors such as, LIGO and Virgo are capable of recording the GWs emitted by different sources such as BNSs and BBHs. In this chapter, we describe the algorithms we use to extract GW signals buried in noisy detector data. The main data analysis technique we employ to detect GW signals is known as *Matched Filtering*. Matched filtering is a well studied technique in the area of signal processing [2]. The LIGO, Virgo CBC data analysis search pipeline is a hierarchical pipeline that employs matched filtering to identify GW triggers based on a match between detector data and GW signal templates. In addition to the standard data analysis search pipeline (ihope) that was employed in recent science runs, we also discuss features of a coherent search algorithm in this chapter. Although coherent

searches are expected to perform better than current standard search method, which is also known as a coincident search, due to computational expenses, we only relatively recently searched for GW signals in LIGO, Virgo science data with the coherent search pipeline.

2.2   The Optimal Filter

Matched filtering is an effective way to search for signals with known patterns buried in noisy data. Let us denote detector noise as $n(t)$ and the GW signal we are searching for as $h(t)$. Then the output of a GW detector can be represented as [37, 38]

$$x(t) = n(t) + h(t), \tag{2.1}$$

which is a function of time, t.

We assume interferometric GW detector noise to be *Gaussian* and *stationary* with the mean of $n(t)$ equal to zero. The noise is characterized by two-sided power spectral density (PSD) $S_n(f)$ as

$$\langle \widetilde{n}(f)\widetilde{n}(f') \rangle \equiv \delta(f - f')S_n(f), \tag{2.2}$$

where $\langle ... \rangle$ denotes the expectation value.

The inner product

$$(h|x) = \int_{-\infty}^{\infty} \frac{\widetilde{h}^*(f)\widetilde{x}(f)}{S_n(f)}\,\mathrm{d}f \tag{2.3}$$

is used to define the matched-filter $(h|x)$. Above, $\widetilde{h}(f)$ denotes the Fourier transform of $h(t)$.

By factorizing the denominator of Eq. (2.3) noise PSD $S_n(f)$ in to two Amplitude Spectral Density (ASD) [1] factors, $\sqrt{S_n(f)}$, and associating them with data and template separately, we can re-express the integrand as, $\frac{\widetilde{h}^*(f)}{\sqrt{S_n(f)}}\frac{\widetilde{x}(f)}{\sqrt{S_n(f)}}$ [37]. In this form effectively the ASD factors are weighting the data and template inversely in the before mentioned inner product.

2.3 Searching for gravitational wave signals in noisy data

As noted above the detector output $x(t)$ may or may not have a GW signal present. These two cases constitute the two hypotheses used to calculate the probability of detecting a GW signal in a noisy data stream:

$$x(t) = \begin{cases} n(t) + h(t), & \text{signal present}, \\ n(t), & \text{signal absent}. \end{cases} \quad (2.4)$$

Starting with Baye's law of conditional probabilities, we can compute *a posteriori* probability $P(h|x)$ that the signal is present, given the output of the detector, namely,

$$P(h|x) = \frac{P(h)P(x|h)}{P(x)}, \quad (2.5)$$

where $P(x|h)$ is the probability of obtaining the detector output assuming the signal is present in data and $P(x)$ is the *a priori* probability of obtaining detector output. $P(x|h)$ is also know as the likelihood function. $P(x)$ can be expressed in terms of two possibilities, with signal that present and that it is absent in the data

[39, 40],

$$P(h|x) = P(0)P(x|0) + P(h)P(x|h). \tag{2.6}$$

Equation (2.6) can be substituted in Eq. (2.5) to obtain

$$P(h|x) = \frac{P(h)P(x|h)}{P(0)P(x|0) + P(h)P(x|h)}. \tag{2.7}$$

We divide the right hand side (RHS) of Eq. (2.7) by $P(h)P(x|0)$ to get

$$P(h|x) = \frac{P(x|h)/P(x|0)}{[P(0)/P(h) + P(x|h)/P(x|0)]}. \tag{2.8}$$

We define the likelihood ratio as,

$$\Lambda = \frac{P(x|h)}{P(x|0)}. \tag{2.9}$$

Now we can combine likelihood ratio and Eq. (2.8) to get [39, 40, 41],

$$.P(h|x) = \frac{\Lambda}{[P(0)/P(h) + \Lambda]} \tag{2.10}$$

It is shown in Refs. [39, 40, 41] that the likelihood ratio can be expressed as

$$\Lambda = \exp[(x|h) - \frac{1}{2}(h|h)]. \tag{2.11}$$

By taking the logarithm of Eqn. (2.11) we can find log-likelihood ratio (LLR),

$$\ln \Lambda = (x|h) - \frac{1}{2}(h|h) \tag{2.12}$$

the above calculation demonstrates how to compute LLR for a single interferometric GW detector. In recent LIGO and Virgo runs we always analyzed data streams from at least two detectors at a time. For such cases we needed to calculate LLR for a detector network. Following the discussion in Ref. [23] the LLR ratio for a detector network can be written as

$$\ln \Lambda_{NW} = \sum_{I=1}^{M} \ln \Lambda_I = \sum_{I=1}^{M} (x_I|h_I) - \sum_{I=1}^{M} \frac{1}{2}(h_I|h_I), \qquad (2.13)$$

which can be simplified to [23]

$$\ln \Lambda_{NW} = (x|h)_{NW} - \frac{1}{2}(h|h)_{NW} \qquad (2.14)$$

where M is the number of detectors in the network. We will later use the network LLR to derive detection statistic of a multi-detector coherent search.

2.4 The "ihope" data analysis pipeline

The ihope data analysis pipeline was developed over many years by many LIGO-VIrgo collaborators for detecting GW signals from CBCs [20]. The pipeline runs in a hierarchical mode and contains many steps starting from collecting data to extracting search results. Although it is capable of estimating certain GW source parameters with limited accuracy, mainly it is this is considered as a GW signal detection pipeline for CBC sources.

The results presented in this thesis are mostly based on two different searches known as coincident and coherent searches. The coincident search is performed by running the standard ihope search pipeline on GW detector data. This is also the CBC default search method for LIGO and Virgo science data [25]. In the coincident analysis we are searching for known CBC signal patterns in all the detectors and, to claim a GW detection, signal has to be present in at least two detectors with consistent source parameters. Some of the results presented in this thesis were obtained by running coincident search on recent LIGO/Virgo science data. Despite

14

coincident searches perform very efficiently, only coherent searches can reach the maximum possible sensitivity for CBC searches. However, performing an all-sky, all-time fully coherent search demands a large amount of computational power. Therefore, we developed a hierarchical coherent search pipeline that runs on the output of the coincident or ihope pipeline. Since coherent search runs following the coincident analysis, these two analysis techniques can also be considered as two stages of a single data analysis pipeline. Section 2.6 gives details of the hierarchical coherent search pipeline.

This section provides an overview of the ihope pipeline to help understand the Science data searches presented in later chapters. More details about that pipeline and its features can be found in Refs. [20, 40, 37, 38, 41]. The first step of the data analysis pipeline is to collect data from multiple detectors of a detector network and prepare for the analysis. The LIGO and Virgo GW detector data are sampled at 16384 Hz and 20000 Hz respectively. However data of both LIGO and Virgo are down sampled to 4096 Hz for the analysis [20]. Although all the derivations in previous section for the optimal filter assume continuous-in-time data, in practice data is discretely sampled. Next step is to divide data in to 2048 second blocks for the analysis. This serves two purposes, namely analysing 2048 second blocks is computationally efficient and the noise power spectral density (PSD) of the detectors are nearly stationary on that time-scale. These 2048 second chunks are further divided into 256 seconds segments. The noise PSDs for the blocks are calculated by taking the median of separate segments. More details about how PSD is estimated for CBC searches can be found in Ref. [40, 20]. Data blocks that are smaller than 2048 seconds are not analyzed, since they can not provide

accurate estimate for the PSD.

For CBC data analysis, we are interested in searching in a large parameter space. The range of masses we search for varies depending on the search type. In the next step, which is to generate the template bank, one ensures that the bank is dense enough in the parameter space to ensure minimal loss of matched-filtering SNR for any CBC signal. Templates are placed in parameter space so that the match between any GW signal and the best-fitting template is better than a pre-determined minimum match (typically 97%)[20, 42]. The matched filtering of GW detector data with a bank of templates is considered as the most important step of the ihope pipeline. Equation (2.3) gives the mathematical form of matched filtering. The outcome of the matched filtering step is a set of GW triggers for each GW detector. In order to minimize the computational requirements for the next steps of the pipeline from this point onward we only consider triggers that crosses 5.5 in signal-to-noise ratio(SNR). This specific value was chosen based on simulation and past experience. After selecting triggers that cross that threshold, the search algorithm seeks for coincident events in time, binary mass, and GW amplitude across different GW detectors. If at least two detectors have triggers with consistent masses and amplitudes occurring at times separated only by the light travel time across the distance between the detectors, we call them coincident triggers.

The loudness of a GW signal (SNR) and coincident test alone are not sufficient to claim a GW detection. Most of the noise artifacts present in interferometric detectors can have same features as real GW signals. In order to avoid such false triggers, matched filtering step is repeated again, this time to perform signal-based

16

vetoes. Additionally, in this second matched filtering step, only the templates that matched with data in the previous step are selected for constituting the bank of templates a second time. The χ^2 signal-consistency test [43] is performed on selected triggers in the second matched filtering step.

In reality, one may find a similar significance for a GW signal and a glitch. In χ^2 signal-consistency test a template is divided into a number of sub-templates in frequency space to see what contribution each sub-template brings to total SNR. This test can separate glitches and GW signals of equal strength as contribution to total SNR for a GW signal comes equally from all sub-templates and glitches will not have this feature. Reference [43] presents the details of this signal-based discriminator and how to employ it efficiently to improve signal detection efficiency. Finally the triggers that pass the χ^2 test are considered as GW candidates. Remaining triggers are not considered for further analysis. If the individual detector SNR is ρ_I in the Ith detector, for a coincident GW candidate, then the combined SNR can be written as,

$$\rho^2{}_{combined} = \sum_{I=1}^{M} \left(\rho^I\right)^2 \tag{2.15}$$

where M is the number of detectors in the network.

2.5 Multi-detector Coherent Compact-Binary Coalescences searches

In this section we present the basic mathematical formalism and derive detection

statistic of the multi-detector coherent hierarchical search for non-spinning CBC signals based on Ref. [8]. Combining data from multiple GW detectors in a coherent manner gives the maximum sensitivity in Gaussian and stationary noise. Therefore, coherent analysis plays an important role in multi-detector searches. However, coherent searches for detector networks with two or less detectors reduces to coincident searches.

Consider a non-spinning coalescing compact binary with component masses $m_{1,2}$, such that its total mass is $M = m_1 + m_2$ and its reduced mass is $\mu = m_1 m_2 / M$. In the restricted post-Newtonian approximation, the two polarizations determining the GW strain are defined in equations (2.1) and (2.2) of reference [8]. The two polarizations h_+ and $h_\times$ depend on M, μ, the luminosity distance to the source r, the inclination angle of the source's orbital-momentum vector to the line of sight ι, the time of coalescence of the signal t_c, and the coalescence phase of the signal φ_c. Above, $\varphi(t; t_c, M, \mu)$ is the orbital phase of the binary [44, 45], $\mathcal{M} = \mu^{3/5} M^{2/5}$ is the chirp mass, G is the gravitational constant and c is the speed of light in vacuum. The GW strain in a detector can then be modeled as,

$$h(t) = F_+ h_+(t) + F_\times h_\times(t) , \tag{2.16}$$

where $F_{+,\times}$ are antenna-pattern functions that quantify the sensitivity of the detector to the sky-position and polarization of the source,

$$\begin{pmatrix} F_+ \\ F_\times \end{pmatrix} = \begin{pmatrix} \cos 2\psi & \sin 2\psi \\ -\sin 2\psi & \cos 2\psi \end{pmatrix} \begin{pmatrix} u \\ v \end{pmatrix} , \tag{2.17}$$

18

with ψ being the wave-polarization angle and $u(\alpha, \delta)$ and $v(\alpha, \delta)$ being detector-orientation dependent functions of the source sky-position angles (α, δ) [46, 23].

Following Ref. [47], let us map the CBC signal parameters $(r, \psi, \iota, \varphi_c)$, into new parameters, $a^{(k)}$, with $k =1,...,4$, such that the strain in any given detector has a *linear* dependence on them:

$$h(t) = \sum_{k=1}^{4} a^{(k)} \mathsf{h}_k(t) \,, \tag{2.18}$$

where the $\mathsf{h}_k(t)$'s are completely independent of those four parameters. By comparing the expression for the GW strain h_+ and $h_\times$, and (2.16), we find

$$
\begin{aligned}
\mathsf{h}_1(t) &\propto u(\alpha, \delta) \cos[\varphi(t; M, \mu, \alpha, \delta, t_c)] \,, \\
\mathsf{h}_2(t) &\propto v(\alpha, \delta) \cos[\varphi(t; M, \mu, \alpha, \delta, t_c)] \,, \\
\mathsf{h}_3(t) &\propto u(\alpha, \delta) \sin[\varphi(t; M, \mu, \alpha, \delta, t_c)] \,, \\
\mathsf{h}_4(t) &\propto v(\alpha, \delta) \sin[\varphi(t; M, \mu, \alpha, \delta, t_c)] \,,
\end{aligned} \tag{2.19}
$$

where the proportionality factor is $[G\mathcal{M}/c^2][(t_c - t)/(5G\mathcal{M}/c^3)]^{-1/4}$. This method of resolving the GW strain signal in a basis of four time-varying functions was first found in Ref. [48] for pulsar signals.

The new parameters, $a^{(k)}$, with the index k taking four values, are defined in terms of $(r, \psi, \iota, \varphi_c)$ as,

$$
\begin{aligned}
a^{(1)} &= \frac{1}{r}\left(\cos 2\psi \cos \varphi_c \frac{1+\cos^2 \iota}{2} - \sin 2\psi \sin \varphi_c \cos \iota\right), \\
a^{(2)} &= \frac{1}{r}\left(\sin 2\psi \cos \varphi_c \frac{1+\cos^2 \iota}{2} + \cos 2\psi \sin \varphi_c \cos \iota\right), \\
a^{(3)} &= -\frac{1}{r}\left(\cos 2\psi \sin \varphi_c \frac{1+\cos^2 \iota}{2} + \sin 2\psi \cos \varphi_c \cos \iota\right), \\
a^{(4)} &= -\frac{1}{r}\left(\sin 2\psi \sin \varphi_c \frac{1+\cos^2 \iota}{2} - \cos 2\psi \cos \varphi_c \cos \iota\right).
\end{aligned}
\tag{2.20}
$$

These constitute an alternative set of parameters that define the likelihood ratio. We used parenthetic indices above to avoid confusing them with numerical exponents.

To explore the properties of the LLR, it will be useful to define the (complex) unit-norm template $S^I(t)$ associated with the circular-polarization component of a GW, namely, $h_+(t) + ih_\times(t)$. It can be shown [23] that

$$
S^I(t) = g_{(I)}^{-1}\left[\xi^I(t_c - t)\right]^{-1/4} e^{i\varphi(t)},
\tag{2.21}
$$

where $g_{(I)}$ (with units of $\sqrt{\text{Hz}}$) is a normalization factor, such that $\langle S^I, S^I\rangle = 1$, and

$$
\xi^I = \frac{5}{256 f_s^I}\left[\frac{G\mathcal{M} f_s^I}{c^3}\right]^{-5/3}
\tag{2.22}
$$

is the time spent by the signal in the detector band, in the Newtonian approximation. Above, f_s^I is the seismic cut-off frequency of the Ith detector below which it has little sensitivity for GW signals. The single detector matched-filter output against $S^I(t)$ can then be defined as

$$
C^I = (S^I, x^I) \equiv \left(c_+^I + ic_-^I\right) = \rho^I e^{i\phi^I},
\tag{2.23}
$$

20

where $c_\pm^I$, ρ^I and ϕ^I are all real; $\rho^I = |C^I|$ is often termed as the signal-to-noise ratio (SNR) in the Ith detector. Since the detector strain due to a GW signal is expected to be tiny, one has $g_{(I)} \gg 1$. Therefore, for computational efficiency, we define a new factor that is closer to unity,

$$\sigma_{(I)} \equiv \left(\frac{GM/c^2}{1 \text{ Mpc}} \right) \left(\frac{5G\mathcal{M}\xi}{c^3} \right)^{1/4} g_{(I)} \,, \tag{2.24}$$

with ξ computed for a reference detector selected from one of those in the network. This is convenient since, as explained below, the detection statistics and the parameters $\{\psi, \iota, \varphi_c\}$ are all independent of the above parenthetic scale factors; only the source distance depends on them, and is computed after accounting for them.

Using the strain expression in Eq. (2.18), the LLR for a network of multiple detectors can be recast in terms of $a^{(k)}$, provided one knows how the strain from the same CBC signal varies from one detector to the other. This was explained in Refs. [22, 23]. Here, it suffices to note that this dependence arises owing to: (a) The spatial separation of the detectors, which can cause relative delays in the arrival of the signal. These delays are determined by the source's sky-position and can be accounted for in Eqs. for h_+ and $h_\times$ by adding those delays to t_c. (b) The different orientations of the detectors, which change u and v. Assuming that the noise in the different detectors are statistically independent, the joint LLR for a network of M detectors is

$$
\begin{aligned}
(ln\Lambda_{NW})_M &= \sum_{I=1}^{M} \log \Lambda_I \\
&= N_k a^{(k)} - \frac{1}{2} M_{ij} a^{(i)} a^{(j)} \,,
\end{aligned} \tag{2.25}
$$

21

where, in the last expression, the sum over detectors has been absorbed in N_k and M_{ij}, as defined below:

$$\begin{pmatrix} N_1 \\ N_2 \\ N_3 \\ N_4 \end{pmatrix} = \chi \begin{pmatrix} \sum_{I=1}^{M} \sigma_{(I)} u_I c_+^I \\ \sum_{I=1}^{M} \sigma_{(I)} v_I c_+^I \\ \sum_{I=1}^{M} \sigma_{(I)} u_I c_-^I \\ \sum_{I=1}^{M} \sigma_{(I)} v_I c_-^I \end{pmatrix} = \chi \begin{pmatrix} \mathbf{u}_\sigma \cdot \mathbf{c}_+ \\ \mathbf{v}_\sigma \cdot \mathbf{c}_+ \\ \mathbf{u}_\sigma \cdot \mathbf{c}_- \\ \mathbf{v}_\sigma \cdot \mathbf{c}_- \end{pmatrix}. \tag{2.26}$$

Above, $\mathbf{u}_\sigma$ and $\mathbf{v}_\sigma$ are network vectors with components $\sigma_{(I)} u_I$ and $\sigma_{(I)} v_I$, respectively, $\mathbf{c}_\pm$ are network vectors with components $c_\pm^I$, and

$$\chi \equiv \pi^{2/3} \left[\frac{GM_\odot/c^2}{1\text{Mpc}} \right]^{3/4} \text{Mpc} \tag{2.27}$$

is a normalization factor with dimensions of length. Also,

$$\mathbf{M} = \begin{pmatrix} A & B & 0 & 0 \\ B & C & 0 & 0 \\ 0 & 0 & A & B \\ 0 & 0 & B & C \end{pmatrix} \tag{2.28}$$

with

$$\begin{pmatrix} A \\ B \\ C \end{pmatrix} = \chi^2 \begin{pmatrix} \|\mathbf{u}_\sigma\|^2 \\ \mathbf{u}_\sigma \cdot \mathbf{v}_\sigma \\ \|\mathbf{v}_\sigma\|^2 \end{pmatrix}, \tag{2.29}$$

which define the network template-norm, namely, twice the second term on the right-hand side of Eq. (2.25); the first term there can be interpreted as the matched-filter output of the network data-vector, $\mathbf{x} \equiv \{x^1, x^2, ..., x^M\}$ [23].

Maximizing $2 \log {}^{(M)}\Lambda$ with respect to $\mathbf{a} = \{a^{(1)}, a^{(2)}, a^{(3)}, a^{(4)}\}$ yields

$$2 \log \left. {}^{(M)}\Lambda \right|_{\bar{\mathbf{a}}} = \mathbf{N}^T \cdot \mathbf{M}^{-1} \cdot \mathbf{N} \,, \tag{2.30}$$

which is still a function of $\{M, \mu, \alpha, \delta, t_c\}$. (Note that the above statistic is independent of χ.) The concomitant maximum likelihood *estimates* (MLEs) of the complementary set of four parameters are denoted with an overline:

$$\bar{\mathbf{a}} = \mathbf{M}^{-1} \cdot \mathbf{N} \,. \tag{2.31}$$

These estimates are also functions of $\{M, \mu, \alpha, \delta, t_c\}$, and are determined by the data through $c_{\pm}^I$ as follows:

$$
\begin{pmatrix} \bar{a}^{(1)} \\ \bar{a}^{(2)} \\ \bar{a}^{(3)} \\ \bar{a}^{(4)} \end{pmatrix} = \frac{\chi}{\Delta} \begin{pmatrix} \|\mathbf{v}_\sigma\|^2 \ (\mathbf{u}_\sigma \cdot \mathbf{c}_+) - (\mathbf{u}_\sigma \cdot \mathbf{v}_\sigma) \ (\mathbf{v}_\sigma \cdot \mathbf{c}_+) \\ -(\mathbf{u}_\sigma \cdot \mathbf{v}_\sigma) \ (\mathbf{u}_\sigma \cdot \mathbf{c}_+) + \|\mathbf{u}_\sigma\|^2 \ (\mathbf{v}_\sigma \cdot \mathbf{c}_+) \\ \|\mathbf{v}_\sigma\|^2 \ (\mathbf{u}_\sigma \cdot \mathbf{c}_-) - (\mathbf{u}_\sigma \cdot \mathbf{v}_\sigma) \ (\mathbf{v}_\sigma \cdot \mathbf{c}_-) \\ -(\mathbf{u}_\sigma \cdot \mathbf{v}_\sigma) \ (\mathbf{u}_\sigma \cdot \mathbf{c}_-) + \|\mathbf{u}_\sigma\|^2 \ (\mathbf{v}_\sigma \cdot \mathbf{c}_-) \end{pmatrix} \,, \tag{2.32}
$$

where $\Delta \equiv AC - B^2$. The MLE of a parameter will be denoted by placing an overline on its symbol.

It is important to note that the maximization in Eq. (2.30) assumes that the network matrix $\mathbf{M}$ is invertible. This is not true, in general. Indeed, $\mathbf{M}$ is singular when $\mathbf{u}_\sigma$ is aligned with $\mathbf{v}_\sigma$. These two vectors are determined by how the interferometers in the network are oriented with respect to the wave propagation vector, but are not affected by the polarization angle ψ. In addition to this singularity, $\mathbf{M}$ can be rank deficient, thus, making the problem of inverting it ill-posed [49]. Physically, this implies that the network does not have enough linearly independent basis detectors to be able to resolve the source parameters $\mathbf{a}$.

Note that these maladies of $\mathbf{M}$ are dependent on the sky-position angles. This means that a network that is able to resolve the signal parameters for certain source sky-positions may not be able to do so for others. These problems can be tackled by regularizing $\mathbf{M}$ in a variety of ways that have been explored in the context of searches of transient signals from unmodeled sources, also called "burst" searches [49, 50, 51]. These methods obviate the rank-deficiency problem at the cost of making the search statistic sub-optimal. Thus, any deficiencies arising from potential singularities in $\mathbf{M}$ or its regularization method adopted by a search pipeline will affect its performance. Since $\mathbf{M}$ is independent of the detector strain data, such effects will arise in searches in simulated Gaussian data sets as well, such as the ones studied here. Since our results below are devoid of these maladies, we are confident that they will not arise in real data searches as well.

The maximum-likelihood estimates for the four physical parameters $(r, \psi, \iota, \varphi_c)$ can now be expressed in terms of the above estimates by inverting Eq. (2.20) and replacing $\mathbf{a}$ with $\bar{\mathbf{a}}$. Specifically, for the luminosity distance we get:

$$\bar{r} = \frac{\sqrt{1 + 6\cos^2\bar{\iota} + \cos^4\bar{\iota}}}{2\|\bar{\mathbf{a}}\|}, \tag{2.33}$$

where $\|\bar{\mathbf{a}}\| \equiv \sqrt{\sum_{i=1}^{4}\left(\bar{a}^{(i)}\right)^2}$ is the norm of the four-parameter vector MLE, and $\bar{\iota}$ is defined below along with the other MLEs. Since those angular parameter estimates should not depend on an overall scaling of $\bar{\mathbf{a}}$, it helps to define the dimensionless unit-norm components $\hat{\bar{a}}^{(k)} \equiv \bar{a}^{(k)}/\|\bar{\mathbf{a}}\|$. In terms of the $\hat{\bar{a}}^{(k)}$, the

maximum-likelihood estimates for the three angular parameters are,

$$
\begin{aligned}
\bar{\psi} &= \frac{1}{4}\sin^{-1}\left(\frac{2\left(\hat{\bar{a}}^{(1)}\hat{\bar{a}}^{(2)} + \hat{\bar{a}}^{(3)}\hat{\bar{a}}^{(4)}\right)}{\sqrt{1-\zeta^2}}\right), \\
\bar{\phi}_c &= -\frac{1}{2}\sin^{-1}\left(\frac{2\left(\hat{\bar{a}}^{(1)}\hat{\bar{a}}^{(3)} + \hat{\bar{a}}^{(2)}\hat{\bar{a}}^{(4)}\right)}{\sqrt{1-\zeta^2}}\right), \\
\bar{\iota} &= \cos^{-1}\left(\frac{1-\sqrt{1-\kappa^2}}{\kappa}\right),
\end{aligned}
\tag{2.34}
$$

where $\zeta \equiv 2\left(\hat{\bar{a}}^{(1)}\hat{\bar{a}}^{(4)} - \hat{\bar{a}}^{(2)}\hat{\bar{a}}^{(3)}\right)$ and

$$
\kappa = \frac{\zeta}{1+\sqrt{1-\zeta^2}}.
\tag{2.35}
$$

Note that the expression for $\bar{\psi}$ goes over to that of $\bar{\phi}_c$ under the transformation $\bar{\psi} \longrightarrow (-\bar{\phi}_c)/2$ and $\hat{\bar{a}}^{(2)} \leftrightarrow \hat{\bar{a}}^{(3)}$. This relation arises from a similar symmetry exhibited by the $a^{(k)}$ defined in Eq. (2.20). Expressions for the CBC MLEs and the coherent statistic were first obtained in Refs. [22, 23]. Above, we reexpress them in terms of the four parameters $a^{(k)}$ since the search code in LAL uses them [35].

Substituting for $\mathbf{M}$ and $\mathbf{N}$, the MLR can be expanded as,

$$
2\log\Lambda\Big|_{\bar{\mathbf{a}}} = (\mathbf{w}_+ \cdot \mathbf{c}_+)^2 + (\mathbf{w}_- \cdot \mathbf{c}_+)^2 + (\mathbf{w}_+ \cdot \mathbf{c}_-)^2 + (\mathbf{w}_- \cdot \mathbf{c}_-)^2,
\tag{2.36}
$$

where $\mathbf{w}_\pm$ are network vectors with components $w_\pm^I$,

$$
\begin{pmatrix} w_{I+} \\ w_{I-} \end{pmatrix} = \begin{pmatrix} O_{11} & O_{12} \\ O_{21} & O_{22} \end{pmatrix} \begin{pmatrix} \sigma_{(I)}u_I \\ \sigma_{(I)}v_I \end{pmatrix},
\tag{2.37}
$$

and

$$
\begin{pmatrix} O_{11} & O_{12} \\ O_{21} & O_{22} \end{pmatrix} = \frac{1}{\sqrt{2\Delta}} \begin{pmatrix} \sqrt{C+A+D}/G_1 & \sqrt{C+A+D}(C-A-D)/(2BG_1) \\ \sqrt{C+A-D}/G_2 & \sqrt{C+A-D}(C-A+D)/(2BG_2) \end{pmatrix},
\tag{2.38}
$$

with $D \equiv \sqrt{(A-C)^2 + 4B^2}$ and $G_{1,2} \equiv \sqrt{(C - A \mp D)^2 + 4B^2}\,/(2B)$. The above matrix diagonalizes $\mathbf{M}$ and, in so doing, identifies the dominant polarization basis, first identified in [22] and named as such in [50].

The coherent search statistic is just $2 \log \Lambda \big|_{\bar{\mathbf{a}}}$ maximized over $\{M, \mu, \alpha, \delta, t_c\}$, namely,

$$\rho_{\text{coh}}^2 = 2 \log \Lambda \big|_{\bar{\boldsymbol{\vartheta}}}, \tag{2.39}$$

where $\boldsymbol{\vartheta} = \{a^{(1)}, a^{(2)}, a^{(3)}, a^{(4)}, M, \mu, \alpha, \delta, t_c\}$ is a set of nine parameters for the non-spinning CBC signal. The last five parameters are searched for numerically, by using a grid for the masses and the sky-position and by using the fast Fourier transform [52] to search for the coalescence time. $\bar{\boldsymbol{\vartheta}}$ denotes the MLE values of these parameters. Searching over (α, δ) requires the flexibility to delay $c_{\pm}^I$ relative to $c_{\pm}^J$ by an interval that can be anywhere between zero and the light-travel-time between the locations of the Ith and Jth detectors or the negative of it. This is why we construct small snippets of $C^I(t)$ called *C-data* around the end-time of every trigger that is found to be coincident in multiple detectors in a network. The statistic defined above will be termed as the coherent network SNR and is the detection statistic optimal in stationary, Gaussian noise [23].

Equation 2.39 of coherent network SNR can be compared to network SNR of coincident search given by 2.15.

2.6   The blind hierarchical coherent pipeline

Owing to requirement of large computational expenses, the coincident search was

selected as the default search method for recent LIGO-Virgo official CBC searches [25]. However, coherent search is expected to perform with better sensitivity. As a computationally feasible solution, we developed the hierarchical coherent search algorithm, which does not demand large computational resources required to a all-sky, all-time fully coherent search. The hierarchical coherent search runs as a part of the ihope pipeline and it takes GW candidates produced by the coincident search as input. In the coherent search, these candidates/triggers are coherently combined to derive coherent detection statistics. The fact that the hierarchical coherent search only analyzes triggers found by a different search reduces significant amount of computational expenses. However, at the same time this method is not capable of finding new GW triggers. Recent studies with the blind hierarchical coherent analysis showed very promising results with both Gaussian and real detector data. The next few chapters will demonstrate the capabilities and findings of the all-sky, att-time blind hierarchical search. This section will give an overview of the hierarchical coherent pipeline.

The first step of this algorithm generates a bank of templates, which is also known as the *coherent bank*, for coherent searches. These templates are created based on the known trigger times and mass pairs coming from the coincident analysis. In coincident search, owing to differences in noise PSD of individual detectors, template banks can be different from one another [33, 20]. Therefore for a coincident trigger coming from ihope pipeline it is possible for coincident triggers to have different templates in individual detectors for the same GW signal. However, in an ideal coherent analysis the template bank should be the same for all detectors in a network [28].

Additionally, template placement should be done according to a coherent template metric. Since hierarchical coherent search runs following the coincident search, for all the triggers instead of computing network templates afresh we choose one template from available detectors as the network template to save computational power. The template we choose is from the detector that found loudest GW trigger in coincident analysis. Reference [8] describes this process in detail. That common template is next used to compute the matched-filter output, which is in the form of an amplitude and phase time-series, for every detector in the coincidence. That step also computes the template normalization factors and implements signal-based vetoes.

Unlike in coincident search it is optional to have an individual detector threshold for matched filter outcome in coherent searches. In the early stages of development of hierarchical coherent analysis, thresholding was used similarly to coincident analysis. Subsequent investigation showed removing matched filtering threshold improves detection efficiency. [1] This means coincident triggers that receive contribution from two different detectors (double-coincident events) while all the detectors are in science mode can become triple-coincident (for three detector networks) events with the removal of the thresholding criteria. According to this set up, theoretically for the analysis of triple-coincident time, all double-coincident events should become triple-coincidences in the coherent analysis. However, there are rare cases this will not happen owing to some complications and those will be explained in the next chapters.

---

[1]The coincident pipeline uses pre-set threshold of SNR 5.5 to choose loud enough triggers for the further analysis.

2.7 Multi-detector signal based vetoes

In section 2.5 we derived network coherent SNR for a multi-detector search. Another statistic that is helpful in discriminating signals from noise glitches in multi-detector data is the null-stream [34]. If $\tilde{C}^I(f)$ is the Fourier transform of $C^I(t)$ obtained in 2.5, then one can show that for GW signals in the data, the mean of

$$Y \equiv \sum_{I=1}^{M} K_I \sigma_{\text{inv}}^{(I)} S_{h(I)}(f) \tilde{C}^I(f) \tag{2.40}$$

is zero. Above, $K_I = \epsilon_{IJK} F_+^J F_\times^K$, with ϵ_{IJK} being the Levi-Civita symbol, and $\sigma_{\text{inv}}^{(I)} \equiv (\sigma_{(I)})^{-1}$. For non-stationary artifacts, however, this need not be true, thereby, motivating the following discriminator:

$$\eta = \frac{\langle |Y| \rangle}{\sqrt{\text{Var}\,(|Y|)}}\,, \tag{2.41}$$

where $\langle x \rangle$ and $\text{Var}(x)$ denote the statistical average and variance of x, respectively. The above construct is called the null-stream statistic. Just like we combine all the data streams coherently to obtain the coherent SNR, we can combine all the data streams such way that combination cancels the GW signal present in data. We can use null-stream as a multi-detector signal based consistency test. For real GW signals signal will cancel out in the detector combination and outcome will be a very small value. However, for glitches, combination will not cancel out the feature in data since all the detectors are not capable of having same type of glitches at the same time.

Chapter 3

Preparations for detecting and characterizing gravitational-wave signals from binary black hole coalescences

3.1 Introduction

Inspiraling BBHs are one of the most promising gravitational-wave sources that the second generation ground-based detectors, such as the Advanced Laser Interferometer Gravitational-wave Observatory (aLIGO) [53] and Advanced Virgo (AdV) [54] detectors, are likely to detect. Currently these laser interferometric detectors are being upgraded and will start collecting data in a few years' time with a sensitivity improvement of about an order of magnitude. The new detector

KAGRA [55] is also expected to take data with a similar design sensitivity later this decade. These detectors will define what is being termed as the Advanced Detector Era (ADE). Second generation instruments will have sensitivity in a broader frequency band compared to the initial detectors and will observe gravitational waves (GWs) from compact binary coalescence (CBC) signals starting at a lower frequency. Observations of X-ray binaries IC10 X-1 [56] and NGC 300 X-1 [57] indicate that the masses of the stellar-mass components of a BBH can be as high as $20-30M_\odot$. The discovery of HLX-1 in ESO 243-49 that has a lower mass limit of approximately 500 $M_\odot$ presents strong evidence for the existence of intermediate-mass black holes [58]. As described in Refs. [59] and [7], binary black holes with component masses that high or higher will be detectable in the ADE detectors only through the merger and ringdown signals. This chapter presents a search for BBH systems with total mass $25M_\odot \leq M \leq 100M_\odot$ and component masses $3M_\odot \leq m_1, m_2 \leq 97M_\odot$. Searches in real LIGO-Virgo data for BBHs in the same mass range were conducted with Inspiral-Merger-Ringdown (IMR) templates in Refs. [59, 7].

The ability to detect GW signals arising from BBH coalescences crucially depends on the accuracy of the waveform models used in designing search templates for detection pipelines. Estimation of parameters of BBH signals also demands accurate knowledge of the inspiral, merger and ringdown phases of the waveforms [60]. In 2008, the Numerical Injection Analysis (NINJA) collaboration was formed to facilitate the interaction of the Numerical Relativity and the GW Data Analysis communities with the objective of modelling CBC signals and using them
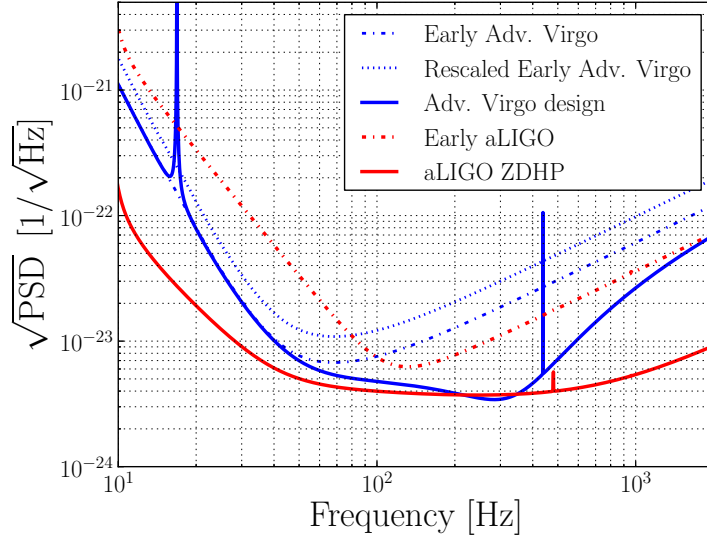
Figure 3.1: Comparison of early and final Advanced LIGO (aLIGO) and Advanced Virgo (Adv. Virgo) design amplitude spectral densities (ASDs) [1]. The ASD is the square-root of the power spectral density (PSD) [2]. The red dotted and solid lines represent early and zero-detuned high-power (ZDHP) aLIGO design ASDs, respectively [3]. The solid blue curve shows the Adv. Virgo design ASD [4]. The blue dotted curve is obtained by rescaling it so that its horizon distance [5] is similar to that corresponding to the early aLIGO ASD.

to perfect GW search pipelines and parameter estimation algorithms. The main purpose of the first NINJA project (NINJA-1) [61] was to foster the exchange of numerical-relativity waveforms to evaluate the performance of a variety of data analysis pipelines in detecting them in simulated initial LIGO and Virgo detector noise. The NINJA-2 exercise, on the other hand, creates the opportunity to test and compare detection pipelines more meaningfully than in NINJA-1 owing
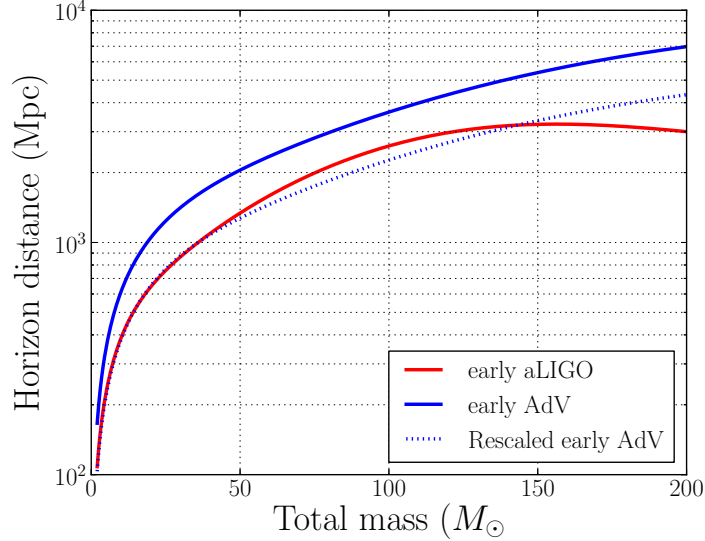
Figure 3.2: Comparison of horizon distances in Mpc for different early advanced detector noise curves as a function of total mass of the binary system in $M_\odot$. This figure is taken from Ref. [6].

to the strict requirements imposed on the accuracy and length of the NR-based waveforms employed by it. The NINJA-2 project required each BBH waveform to include at least five orbits of usable data before merger, i.e. neglecting the initial burst of junk radiation. Additionally, NR waveform amplitude had to be accurate to within 5%, and the phase (as a function of gravitational-wave frequency) should have an accumulated uncertainty over the entire inspiral, merger and ringdown (of the numerical simulation) of no more than 0.5 rad. Following these restrictions eight NR groups have contributed 56 waveforms to NINJA-2 project [62]. Since the typical signal will have more cycles in band than what NR alone can produce at the desired accuracy with the computational resources at hand, post-Newtonian

theory is used to model the remaining cycles to produce long *hybrid* signals, which we will refer to here as pN-NR hybrid signals or simply NR or NR-based signals. The NINJA-2 waveform-catalog paper [62] describes in detail the waveform requirements and method used to construct the pN-NR hybrid waveforms.

In this chapter, we quantify how well "EOBNR" waveforms, obtained from the effective one-body formalism [63] by calibrating against a specific family of NR waveforms, namely, the ones obtained by the NASA-Goddard group [63], perform in detecting pN-NR BBH signals modelled for NINJA-2. In NINJA-2, a variety of NR-based signals were injected in simulated Gaussian, stationary data from three LIGO-Virgo detectors with early ADE sensitivities (see Fig. 3.1). These signals were constructed with contributions from various numerical relativity groups (see Table 1 in Ref. [62]), and are available in the public domain [64]. For the study reported here we focus on non-spinning BBH signals. A total of 2000 such signals from 20 pN-NR signal families were injected in a two-month long data set [64]. The coincident all-sky, all-time compact binary coalescence (CBC) search pipeline [20] was run along with an added coherent stage [8] to search for those signals. We also compare these observations with the results of a study where EOBNR templates were used to find EOBNR signal injections to account for any biases that might arise from the data analysis pipeline itself. We find that the EOBNR templates are slightly less efficient, by about a percent, in detecting non-spinning NR-based signals than in detecting EOBNR injections. Also, the magnitude and nature of the systematic error in the measurement of signal parameters show some interesting but limited variations. In particular, a very small fraction of signals are systematically detected with more massive templates and, therefore, have a mea-

sured end-time that is earlier than the true one. The same signals have a worse match than other signals with EOBNR templates of the same parameters [62]. We show how a coherent all-sky, all-time search can improve CBC detection efficiencies over a coincident analysis by improving the detection probability for any given false-alarm probability. The coherent method requires coincidence of the signal arrival times and other signal parameters, just like a coincident search method [20] does. But the former also checks for the consistency of the signal phases and amplitudes in the various detectors in a network with a physical value for the signal time-delays across the detector baselines. It also provides multi-baseline signal-based tests like the null-stream test that are effective in discriminating real signals from noise artifacts, especially, when the sensitivities of the detectors are comparable [34, 8, 24, 65].

Owing to the high computational cost of employing a fully coherent all-sky, all-time CBC search [23], here we use the *hierarchical* coherent algorithm [8] to search for BBH signals. This algorithm and the detection statistic are described in Sec. 3.2. Coherent data analysis methods have been formulated for searching GW signals from a variety of modelled and unmodelled sources [23, 66, 25, 67, 8, 24]. It is the optimal method in stationary, Gaussian noise under the Neyman-Pearson criterion [2]. In CBC searches, it has been used recently in targeted searches [24] where the time of occurrence of the signal and the sky-position of the source are known, e.g., from the observation of an electromagnetic (EM) counterpart, such as a gamma-ray burst (GRB). It was demonstrated to perform better than the targeted all-sky, all-time coincident search.

In Sec. 3.3, we compare the performances of the coincident and the hierarchi-

cal coherent searches. We find the latter to be somewhat better than the former and explain what factors contribute to this improvement. We argue that the level of improvement is as per expectations for a hierarchical method and that a fully coherent method should be able to yield a much better detection efficiency. We present results from multiple sanity tests that check if the signal injection recovery is consistent with our expectations of a BBH search. Moreover, the effect of signal-based discriminatory tests, such as the chi-square and the null-stream tests, on the performance of that search is also analyzed.

In Sec. 3.4, the accuracy with which various signal parameters are recovered is described. Those results are found to be mostly devoid of systematic errors when compared with measurements of EOBNR injection parameters by using EOBNR templates. The very few cases where a bias was found, the explanation lies in the mismatch of the pN-NR hybrid signal in those cases with the EOBNR templates, as was seen in Ref. [62].

3.2 Coincident and coherent searches for binary black hole systems

3.2.1 Search algorithm

The all-sky, all-time coincident search pipeline that was used to detect injected pN-NR hybrid signals is described in detail in Ref. [20]. On the other hand, the hierarchical coherent search pipeline used here was introduced in Ref. [8]. The latter pipeline consists of the former with an additional stage that computes the

coherent SNR of all coincident triggers found by the former.[1] We will variously refer to these two stages as the coincident (or the first) and the coherent (or the second) stage, respectively. Both these stages comprise multiple steps. The coincident stage first splits the strain data time-series from every detector in the network into 2048 sec chunks. The noise power spectral density (PSD) [2] is estimated for each chunk and is used to construct a template bank for matched filtering. Whenever the signal-to-noise (SNR) of the filtered output crosses a preset threshold, which was chosen to be 5.5 in Refs. [59, 7] and in this work, the template parameters and the time of the trigger are saved for each detector. Next the triggers from individual detectors are compared for coincidences in mass and end-time in two or more detectors to identify multi-detector coincident GW candidate events. Triggers in a detector that do not find any coincidence with a trigger in another detector are dropped from further analysis since currently we do not have a method for assessing the noise background for single detector events. A candidate event is termed as double-coincident (triple-coincident) if the masses and end-times of the triggers in two (three) detectors are found to be very similar [21], as stipulated in advance of the searches. Since the maximum number of detectors available to this search is three, these are the only two types of coincident candidate events possible here. In a real search, a candidate event is subjected to further checks before it is announced as a GW event to ensure that it was not caused by an environmental or instrumental artifact.

The coherent stage requires coincident trigger times in order to begin the coherent analysis. This analysis includes multiple steps, which are similar to the

---

[1]That stage also computes the null stream [34, 24], which will be described in Sec. 3.3.2.

coincident counterpart but include some important modifications. First, a template bank, termed as the coherent bank, is constructed for the coherent analysis using the parameters of the coincident triggers. The triggers identified by the coincident stage can have different mass parameters in different individual detectors due to the different noise in each detector. By definition, however, the same template must be used in every detector for computing the coherent SNR. Here, we choose the mass-template in the loudest detector for that computation. Reference [8] explains this process in detail. That common template is next used to compute the matched-filter output, which is in the form of an amplitude and phase time-series, for every detector in the coincidence. That step also computes the template normalization factors and implements signal-based vetoes.

Similar to the matched-filtering step in the coincident stage, the coherent matched-filtering step used a thresholding criterion in previous studies [8] to reduce the computational cost. This threshold value is set for the individual detectors as in the coincident stage but the value is lowered to allow more triple coincident triggers compared to the coincident counterpart. Typically, the values of previous studies used to be 5.5 for the coincident matched filtering step and 5.0 for the coherent one. One of the main goals of the coherent analysis is to convert all double-coincident triggers in the coincident stage to triples, whenever data are available from all three detectors, to improve the significance of real signals. Although a lower threshold in the coherent stage on individual detector SNRs helps to convert more double coincident events into triples many more remain as doubles when that threshold is non-zero. To improve upon earlier studies, we devised a method to handle these additional background triggers more efficiently,

essentially, by reducing the maximum coincidence duration analyzed at a time. Lowering that threshold to zero allows converting all triggers that were double-coincident in the first stage to triple-coincident ones [2]. This provides additional information about every single trigger due to the phase consistency check we can impose on the signal in every participating detector. The matched-filtering step in the coherent stage is followed by the computation of the coherent SNR and the null stream for every trigger. Since we use large number of templates in our template bank, same feature in detector data can be picked by different template waveforms. This leads to have multiple GW triggers at same end-time. Additionally, for coherent searches multiple sky positions can give triggers for same feature in data. These set of triggers is also know as clusters. The last step of this pipeline clusters the gravitational-wave triggers in time and sky position so that only the most significant of them is retained per cluster.

3.2.2 Detection Statistics

The BBH search algorithms exploit the knowledge of their GW signals to define the templates used for matched filtering. Nine parameters describe the GW signal from nonspinning BBH sources studied here. These are the two component masses m_1 and m_2, the luminosity distance to the source d, the right ascension and declination angles (α, δ) specifying its sky position, its orbital inclination angle ι to the line-

---

[2]Results from the new pipeline show that a few signals that show up as doubles in the coincident stage are still not converted into triples in the coherent stage. This is because those (simulated) signals are very weak in the third detector, thereby, resulting in unphysical time-delays between that and the other two detectors.
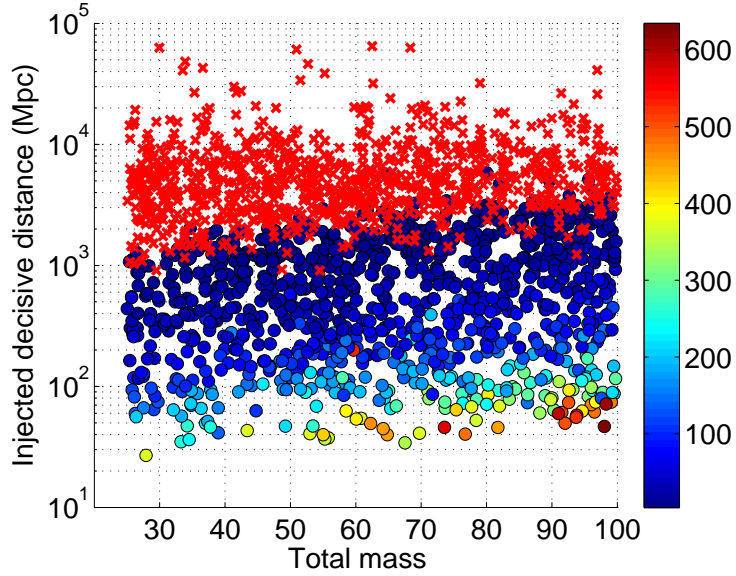
Figure 3.3: The injected decisive distance of found and missed pN-NR simulated signals plotted as a function of total mass of the binary black hole system. The colorbar shows the coherent SNR. A total of 1033 injections were found out of 2000 injections by the search pipeline. Red crosses represent missed simulated signals.

of-sight, the angle ψ describing the orientation of its signal polarization ellipse, the signal coalescence time t_c, and the signal coalescence phase ϕ_c. Alternative mass parameters, in the form of the total mass M, the symmetrized mass-ratio $\eta \equiv m_1 m_2 / M^2$, and the chirp mass $M_{\mathrm{chirp}} \equiv \eta^{3/5} M$ are also often used to describe BBH signal parameters.

For the coincident analysis, the detection statistic used here is the one that was introduced in Ref. [7] for the *high-mass* search in LIGO-Virgo data from the sixth LIGO Science Run (S6) and the second and third Virgo Science Runs (VSR2/3).

That search targeted GW signals from BBH sources with each component mass between $3 - 97 M_\odot$ and total binary mass between $25 - 100 M_\odot$. If the matched-filter output of a unit-norm mass template from a stretch of single-detector data is denoted by ρ, then the detection statistic used for long-duration templates, with a duration $t_{\mathrm{dur}} \geq 0.2$ sec, is the *new* SNR defined as follows:

$$\rho_{\mathrm{new}} = \begin{cases} \dfrac{\rho}{[(1+(\chi_r^2)^3)/2]^{1/6}} & \text{for } \chi_r^2 > 1, \\ \rho & \text{for } \chi_r^2 \leq 1, \end{cases} \tag{3.1}$$

where $\chi_r^2 \equiv \chi^2/(2p - 2)$, and χ^2 is the signal-based time-frequency discriminator studied in Ref. [43] with a chi-squared distribution of p degrees of freedom. On the other hand, for short-duration templates, with a duration smaller than 0.2 sec, the detection statistic used is

$$\rho_{\mathrm{eff}} = \frac{\rho}{[\chi_r^2(1 + \rho^2/50)]^{1/4}} , \tag{3.2}$$

which is termed as the *effective* SNR. These choices were arrived at after comparing their detection efficiencies with those of ρ and other alternative statistics. In a network with M detectors, the coincident detection statistic employed here is

$$\rho_{\mathrm{coinc}} = \begin{cases} \left[\displaystyle\sum_{I=1}^{M} \left(\rho_{\mathrm{eff}}^I \right)^2 \right]^{1/2} & \text{if } t_{\mathrm{dur}}^I < 0.2 \text{sec, for any } I\,, \\ \left[\displaystyle\sum_{I=1}^{M} \left(\rho_{\mathrm{new}}^I \right)^2 \right]^{1/2} & \text{for all other cases}\,, \end{cases} \tag{3.3}$$

where x^I denotes the value of x for the Ith detector. Employing χ^2 in the detection statistic was found to improve the performance of a search, especially, in real data, which is neither Gaussian nor stationary.

41

Contrastingly, a network detection statistic formed from only the ρ^I is the *combined* SNR, which is just $\left[\sum_{I=1}^{M}\left(\rho^I\right)^2\right]^{1/2}$.

The coherent statistic used here is the same as the one defined in Eq. (2.30) in Ref. [8].

When describing how effective a search is in finding signals, one of the parameters used is how distant their sources are. However, from the measured strength of a signal, it is not always possible to deduce the source luminosity distance. This is because the strength of a signal in a detector is determined not only by the proximity of a source but also its location, its orbital inclination angle to the line-of-sight, and the angle ψ describing the orientation of its polarization ellipse. In fact, a source at a luminosity distance d appears to be at an *effective* distance of

$$d_{\text{eff}} = \frac{d}{\sqrt{F_+^2(\alpha, \delta, \psi)\left(1 + \cos^2 \iota\right)^2/4 + F_\times^2(\alpha, \delta, \psi)\cos^2 \iota}}, \qquad (3.4)$$

where $F_{+,\times}$ are the detector antenna-pattern functions. Due to the different orientations and, therefore, $F_{+,\times}$, the effective distance of a source can vary from one detector to another. Since for a detection we require coincidence in at least two detectors, it is essential that the larger of the two corresponding effective distances not be too large for the signal to fall below the detection threshold of the weaker detector. This is why it is useful to define the *injected decisive* distance as the injected effective distance in the second loudest detector in a coincidence. Indeed, in Fig. 3.3 we show how this quantity and the coherent SNR vary as a function of the total-mass of the injected sources. It is manifest that the closer sources are found with a higher coherent SNR whereas many of the very distant sources are missed.
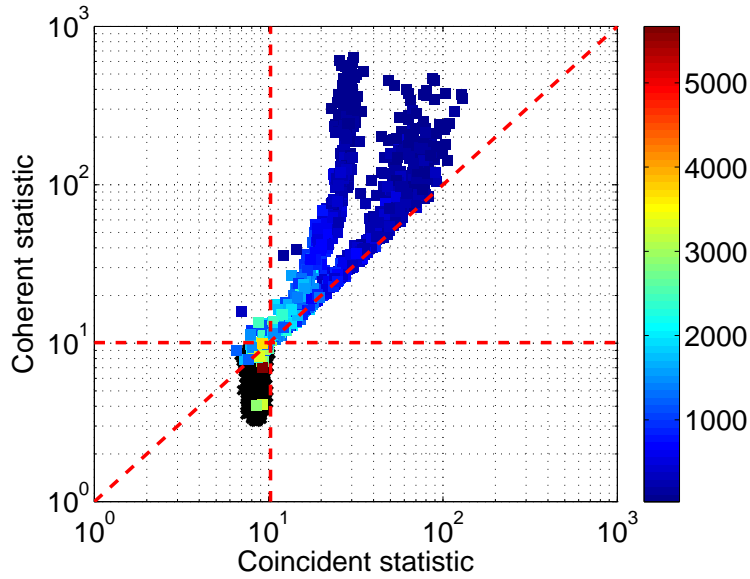
Figure 3.4: The coherent and coincident detection statistic values of found simulated signals (colored squares) and background events (black crosses). The colorbars show the injected decisive distance in Mpc. The coherent SNR is used as the coherent detection statistic. The coincident detection statistic is ρ_{coinc}, as defined in Eq. (3.3), which is the one that was used in the high-mass search of LIGO's S6 and Virgo's VSR 2/3 data [7].

3.3 Detecting pN-NR hybrid signals with EOBNR templates

In this study we analyzed the performance of the hierarchical coherent pipeline in simulated Gaussian noise. Strain noise time-series were produced for two LIGO detectors, H1 and L1, and the Virgo detector, V1, using the design noise curves of early advanced LIGO and advanced Virgo detectors [19], respectively. Each time-
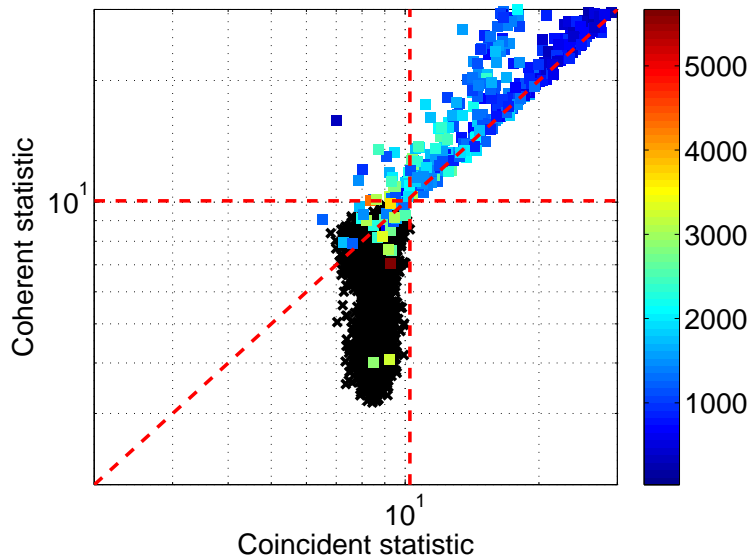
Figure 3.5: Zoomed version Fig. 3.4 shows better the distribution of the weak injections in the two statistics.

series is continuous and is of two months' duration. Performance of the search pipelines was evaluated by injecting pN-NR waveforms in the simulated data and recovering them with EOBNR templates [68]. As with the LIGO-Virgo highmass search in S6-VSR2/3 data, here too the template bank used for matched-filtering spans $3-97M_\odot$ for each of the two component masses and $25-100M_\odot$ for the total mass. The noise curves used to simulate noise in this study is the same as the one used for NINJA-2 blind injection challenge [69]. Unlike in blind injection studies, it is Gaussian and stationary and has early aLIGO noise amplitude spectral density (ASD) for H1 and L1 and rescaled early advanced Virgo ASD for V1, as depicted in Fig. 3.1. As the name suggests, the latter is obtained by rescaling early AdV ASD to match the noise expected in V1 when H1 and L1 will be taking early aLIGO data in the future.
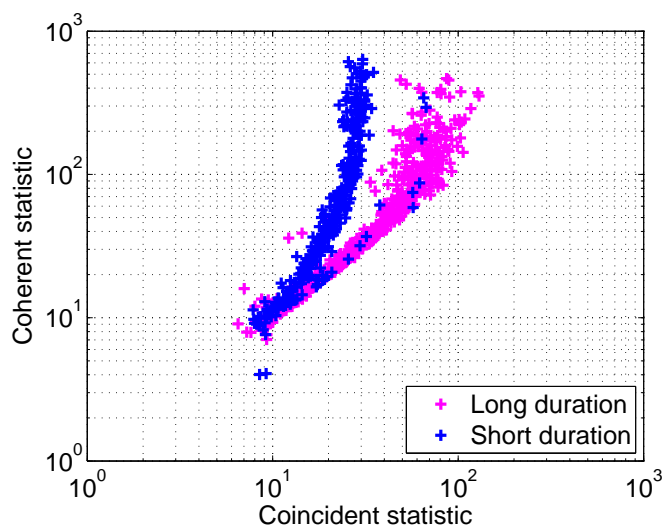
Figure 3.6: Distribution of pN-NR simulated injections can be mostly separated into two groups characterized by the duration, long or short, of the template they triggered in the coherent search. This plot shows that a small subset of the triggers with a long-duration template fall in the same cluster as the ones with a short-duration template, and *vice versa*. This is because a signal can trigger multiple templates; the loudest trigger in coherent statistic can correspond to a different template than that of the loudest trigger in a coincident statistic, which penalizes short-duration ones more than the long-duration ones.

Rescaling Virgo noise curve creates the opportunity to have three equally sensitive detectors and it benefits parameter estimation studies and multi-detector signal based vetoes in coherent analysis. It is important to note that these curves are not the 2015-predicted curves, but a best guess at them from over a year ago when NINJA-2 data sets were created. In the past, real data from the LIGO and Virgo detectors had more dissimilar ASDs than the one used in NINJA-2. This

45

aspect of our search assumes special significance since we later study the performance of the null stream, which is more powerful for detectors in a network with similar rather than disparate sensitivities.

Since the hierarchical coherent pipeline is not a fully coherent all-sky search, it depends on some other search method to identify the GW event times. In our study we analyze GW events identified by the coincident CBC pipeline. The coherent pipeline takes GW event times found by the latter as its input and does a coherent analysis of the individual detector data from around those trigger times. Compared to a fully coherent all-sky search, which combines complete time series coherently to identify GW events, the hierarchical coherent search requires less computational power. One of the main goals of this paper is to draw lessons from the hierarchical coherent search that can benefit the development of a fully coherent search for the ADE.

One major difference between the hierarchical coherent analysis used in this paper and those employed in the past [8] is that after the coincidence stage identifies a part of the data that offers an interesting trigger, its coherent SNR is computed by involving every detector that was active at the time, even if it did not contribute to the coincidence in that stage (e.g., because the SNR in the third detector was below threshold around that event time). Previous searches used thresholds for individual matched-filter outputs to reduce the computational cost. Typical value for this SNR threshold was 5.0, which was chosen to be somewhat below the threshold in the first stage, of 5.5, chosen for the matched filtering step. By placing an SNR threshold of 5.0 the coherent pipeline allowed the conversion of some double coincident triggers (namely, H1L1, L1V1 and H1V1) to triple-coincident

H1L1V1 triggers at times when all three detectors had science data, often termed as *triple time*. In this study we lower the individual detector thresholds in the coherent stage to zero. This allows all double and triple coincident triggers, in tripe time, in the coincident stage to be analyzed as triple-coincident triggers in the coherent stage. By doing so for double coincident triggers, the coherent stage uses new information available from the third detector data for constructing the coherent statistic that was not used in constructing the coincident statistic in the first stage (apart from the fact that the third detector is weaker than the other two). This is an important change vis-a-vis the previous hierarchical coherent searches.

We analyzed the performance of the hierarchical coherent pipeline by injecting and recovering the different NR wave-forms submitted to the NINJA-2 project by various NR groups. For this study we considered only non-spinning waveforms with different mass ratios. Two sets of simulated GW signals were injected with distances between 20 Mpc to 2900 Mpc, distributed uniformly in linear or logarithmic distance. Just as for the template bank, for the injections as well the total mass was chosen to be in the range $25 - 100 M_\odot$ and the component masses between $3 - 97 M_\odot$, All the injections recovered by the coincident algorithm were found by the hierarchical coherent pipeline as well, which is expected. On the other hand, although one might expect to find only triple-coincident events after the coherent stage, owing to the removal of the individual detector thresholds there, some events were found to be double-coincident. This is because these injections have very large effective distance in one of the detectors compared to the other two; the event time registered in the detector with the large effective distance (and, therefore, low SNR) typically had a large error and often did not fall within the light
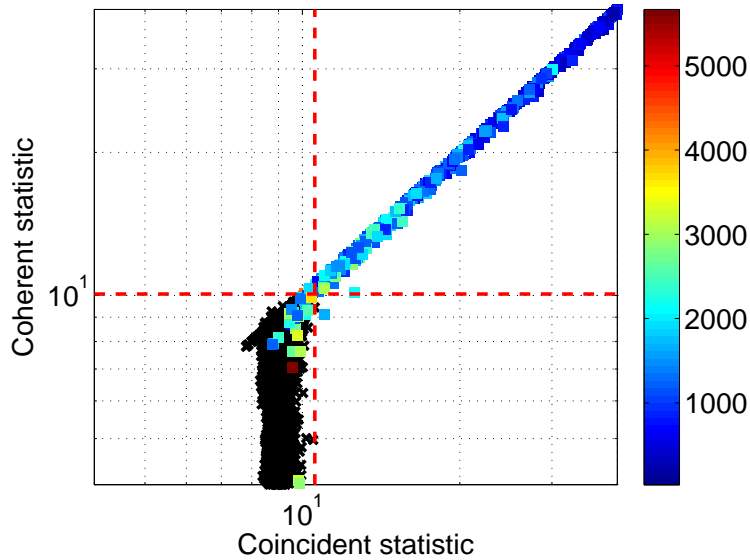
Figure 3.7: The coherent and coincident detection statistic values of found simulated signals (colored squares) and background events (black crosses). The colorbar shows injected decisive distance in Mpc. The coincident detection statistic used here is the combined SNR. This plot confirms that the maximum value the coherent SNR of a trigger can assume is the combined SNR.

travel-time window corresponding to the two baselines formed with the other two detectors. This is why the hierarchical coherent pipeline did not promote them to be triple coincidences but retained them as double coincidences.

Figure 3.3 presents the injected decisive distance of found and missed injected BBH signals as a function of their total mass. As introduced earlier, the injected decisive distance is defined as the effective distance of a source in the detector where it was the second loudest, and is termed so because at least two detectors are required to hear the signal louder than the threshold to produce a coincident event.

The closest missed injection had an injected decisive distance of 907.34 Mpc. Figure 3.6 compares the distribution of injected signals and background triggers using both coincident and coherent detection statistics. The coherent analysis used the coherent network SNR as the detection statistic whereas the coincident analysis employed the same detection statistic as the one used for LIGO-Virgo BBH search of the S6-VSR2/3 data [7], namely, the one defined in Eq. (3.3). Due to the relatively poor performance of the χ^2 test for short-duration templates compared to long-duration ones, this statistic utilizes that information differently for GW triggers associated with those two categories of templates. This is reflected in its definition in Eq. (3.3), and the phenomenological case for it is explained in Ref. [7].

Figure 3.7 plots the coherent SNR of every found injection trigger and background trigger versus the coincident statistic, which in this case is the combined SNR. The color-filled squares denote found simulated signals and the black crosses represent background triggers. While the loudest background trigger in the coincident analysis has a coincident detection statistic value of 10.3, its counterpart in the coherent analysis has a coherent SNR of 10.0. The right plot in Fig. 3.7 is the zoomed version of the left plot, focusing on the most interesting region of the plot where the simulated signals and background events start mixing. The two plots show two red dashed lines, intersecting at right angles, that divide each plot into four quadrants. These lines cut across the loudest background triggers for each analysis, respectively. For instance, colored squares in the region $\rho_{\mathrm{coinc}} > 10.25$ are simulated signals found louder than the loudest background event, or simulated signals found with zero False Alarm Rate (FAR), in the coincident analysis. Sim-

ilarly, the colored squares in the region $\rho_{\text{coh}} > 10.0$ are simulated signals found with zero FAR in the coherent analysis. All the background triggers are confined to the bottom-left quadrant. The top-right quadrant has only injection triggers; these signals are found with a zero FAR in both coincident and coherent searches. The bottom-right quadrant has only injection triggers that have a zero FAR in the coincident search; note that these injection triggers have a non-zero FAR in the coherent search because the loudest background in the coherent search has an SNR (shown by the horizontal red line that is) greater than that of any of these inection triggers. On the other hand, the top-left quadrant has only injection triggers that have a zero FAR in the coherent search. When one counts the injection triggers in these quadrants, one finds that there are more of them in the top-left quadrant than in the bottom-right quadrant. This leads to the inference that in this study the coherent statistic performed better than the coincident one, at zero FAR.

It is also interesting to find that in Fig. 3.6 most of the simulated signals lie above the diagonal; this is due to the re-weighting of coincident SNR based on their χ^2 values. One also finds that the injection triggers in these plots are distributed in two branches. To investigate the reason behind this feature, we plotted the same set of simulated signals after binning them into two different sets based on the duration of the templates that detected them. Events are termed to be of a short duration if at least one of the detectors finding it has a template duration less than 0.2 sec. To be categorized as a long duration event all the participating detectors should have their template durations greater than or equal to 0.2 sec for that event. The bottom plot in that figure indeed shows that these two branches of simulated signals were formed mostly from long and short duration events.
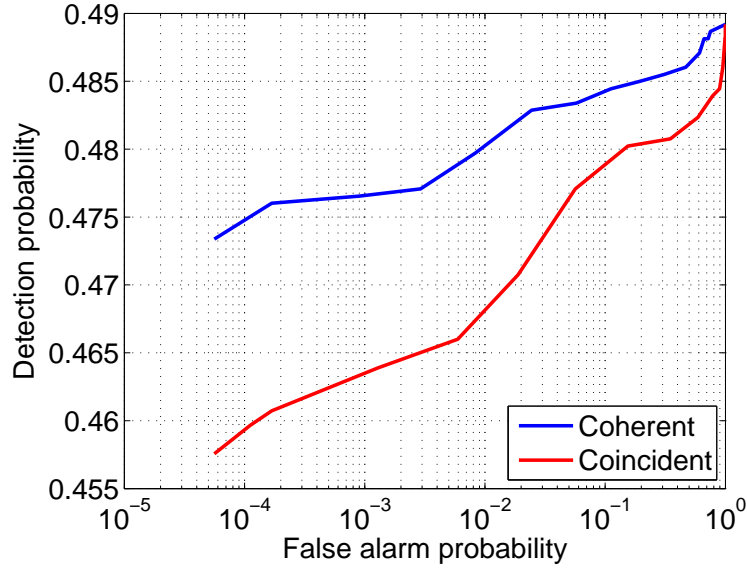
Figure 3.8: Receiver Operating Characteristic (ROC) curves from the injection and (partial) recovery of 2000 numerical relativity simulated signals. The two curves here compare the performances of the coherent and coincident searches.

That plot also shows that a few triggers of each kind are picked by templates of the opposite kind. This is because a signal can trigger multiple templates; the loudest coherent SNR trigger in the second stage can correspond to a different template than the loudest coincident SNR trigger in the first stage. Note that the coincident statistic penalizes short-duration templates more than the long-duration ones.

The maximum value that the coherent SNR can take for any trigger, from background or injection, is the combined SNR. The combined SNR is the square root of the quadrature sum of the individual detector SNRs. Figure 3.7 confirms this statement for both simulated signals and background events. It is clear that most
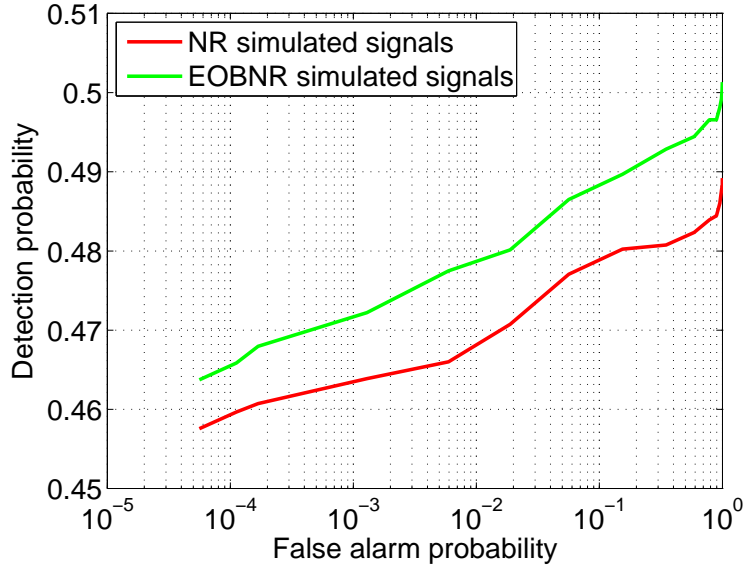
Figure 3.9: The ROC curves for two different simulated signal families, namely, EOBNR and pN-NR, recovered with the same EOBNR template bank.

of the simulated signals fall on diagonal. A relative few, especially of the weak kind, fall below the diagonal. This is because the contribution from their cross detector terms to the coherent SNR is less than maximal. As expected most of background events can be found below the diagonal due to the incoherence of their individual detector triggers. However, these is a small fraction of background triggers that lie on the diagonal. A majority of these are triggers were associated with sky positions that created issues for polarisation matrix inversion. Due to ill-posed polarisation matrix, detection statistic of these triggers had un-physical values larger than the combined SNR. Therefore we assigned combined SNR for detection statistic of such triggers allowing them to be on diagonal.

3.3.1 Comparing ROC curves

In this section we address the following two issues. First, we enquire if the coherent stage improves the detectability of a CBC signal, which in NINJA-2 is limited to the pN-NR hybrid kind. If an improvement is found then it will make the case for developing computationally viable fully coherent CBC searches. Second, we ask how much worse does an EOBNR template-bank perform in detecting pN-NR signals than those modelled by the EOBNR formalism itself. This exercise probes, in a limited way, if the differences in the deduction of the pN-NR waveforms, on the one hand, and the EOBNR waveforms, on the other hand, are consequential enough to affect the ability of our search pipelines to make a detection. The limitation of this exercise is that it does not address how different EOBNR and pN-NR hybrid waveforms are from a fully accurate waveform solution from General Relativity. For readers interested in that subject, we refer them to Refs. [70, 71, 72, 73, 74], and the references therein. We make both types of comparisons by computing the Receiver Operating Characteristic (ROC) curves [2] for each case.

The ROC curves in the Fig. 3.8 compare the performances of the hierarchical coherent and coincident searches for the same set of simulated pN-NR hybrid signals. The detection probability of the former is higher than the latter for all values of the false alarm probability (FAP) that could be computed in this exercise. But the region in this figure where this observation matters the most is the low FAP region around $10^{-5} - 10^{-4}$, where the first GW detections are expected to be made. Note, however, that the improvement obtained by running the additional coherent
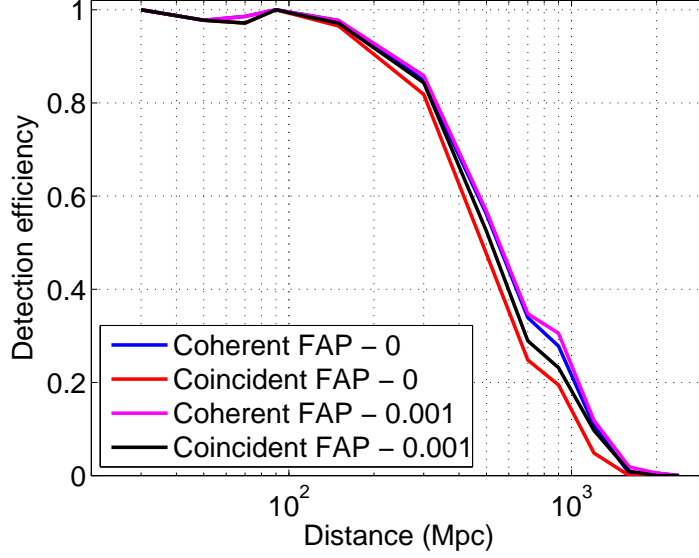
Figure 3.10: The detection efficiency is plotted as a function of the injected decisive distance (Mpc), for the hierarchical coherent and coincident searches, at false-alarm rates (FAPs) of 0.000 and 0.001.

step in this coincident pipeline is limited by its hierarchical nature and, therefore, the utility of this study is that it suggests that a fully-coherent, all-sky, all-time pipeline should perform even better.

The FAP at a given value of the detection statistic, $\rho_{\text{threshold}}$, is obtained as follows

$$\text{FAP}(\rho_{\text{threshold}}) = \frac{N_{\text{background}}(\rho > \rho_{\text{threshold}})}{N_{\text{total background}}}, \tag{3.5}$$

where $N_{\text{background}}(\rho > \rho_{\text{threshold}})$ is the number of background triggers that have the value of their chosen detection statistic ρ greater than $\rho_{\text{threshold}}$, and $N_{\text{total background}}$ is the total number of background triggers, with any value of ρ, found by the
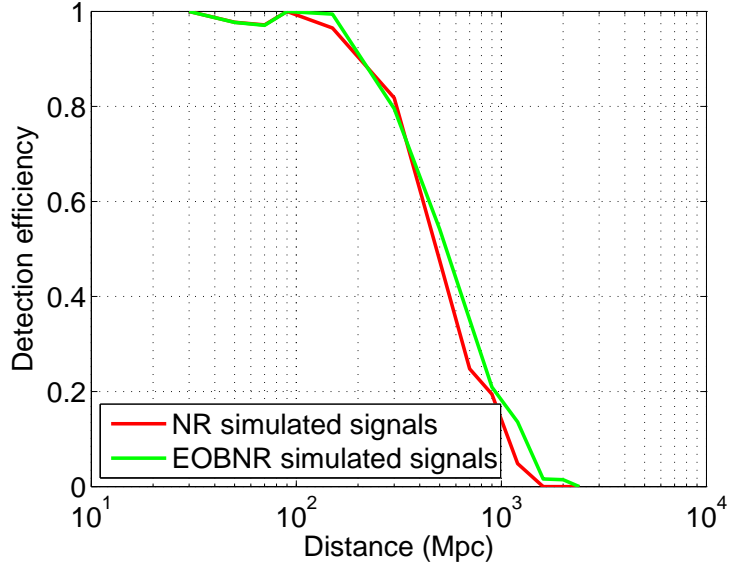
Figure 3.11: Detection efficiency comparison of two different sets of simulated signals, namely, EOBNR and pN-NR.

search. On the other hand, the detection probability is given by

$$P_{\text{detection}}(\rho > \rho_{\text{threshold}}) = \frac{N_{\text{recovered}}(\rho > \rho_{\text{threshold}})}{N_{\text{recovered}}(\rho > \rho_{\text{threshold}}) + N_{\text{missed}}}, \quad (3.6)$$

where $N_{\text{recovered}}(\rho > \rho_{\text{threshold}})$ is the number of recovered simulated signals with the detection statistic value greater than the value corresponding to a given false alarm probability, and N_{missed} denotes the number of simulated signals either with $\rho < \rho_{\text{threshold}}$ or totally missed by the detection pipeline.

To get some insight into the relative behavior of the ROC curves in Fig. 3.8 note that the rate of change of FAP with respect to the detection statistic is faster in the case of the coincident statistic than in the case of the coherent statistic. However, the value of the detection statistic for an injection trigger scales inversely with its distance.

Also, the detection probability decreases with increasing source distance. Thus, it follows that the rate of change of FAP with respect to the detection *probability* is faster in the case of the coincident statistic than the coherent statistic. This is exactly what is found in the left plot in Fig. 3.8. The fact that the two ROC curves there should meet at a high enough FAP, where the detection threshold is very small, then implies that the ROC curve of the coherent search should be above that of the coincident search. The detection probability does not go to unity in that figure because a hard cut-off of $\rho = 5.5$ was placed in each detector in the first stage, thereby, causing a fraction of the triggers to be missed. In this experiment that fraction happened to be about 51%. Figure 3.14 and 3.15 shows how the loudness of the background triggers is distributed for the two searches.

Figure 3.8 shows that at a FAP of 6×10^{-5} the difference between the detection probabilities of the coherent and coincident searches is approximately $(47.4 - 45.8)\% = 1.6\%$. This implies that for a total of 2000 injections the former search found 32 more than the latter, at that FAP.[3] One must bear care, however, in drawing conclusions for astrophysical searches from this simulation study because the source rate for aLIGO is estimated to be in the several tens and not thousands [75], and the aforementioned improvement will affect the detection of very few sources. Instead, the main conclusion is that while hierarchical coherent searches may not be worth investing resources into, they demonstrate the (small) improvement we expect of them and, in turn, suggest that it may be worthwhile to explore how much more gain in detection rate one can achieve with fully coherent all-sky,

---

[3]Note that these two searches are correlated in the sense that a strong (weak) signal in one is highly likely to produce a strong (weak) signal in the other.

all-time algorithms in realistic search pipelines.

We next enquire how much the detectability of a signal suffers owing to the fact the pN-NR hybrid waveforms that are used to model the signals are not quite the same as the EOBNR waveforms used to model the templates [62]. Fig. 3.9 compares the performance of two sets, with the same number of simulated signals injected at the same sky locations, but with two different signal families: The green curve corresponds to signals modelled with the EOBNR family and the red curve represents simulated signals made using the NINJA-2 pN-NR hybrid waveforms. Both sets of simulated signals were searched with EOBNR templates. As expected, simulated signals from the same family as the templates, namely EOBNR, register a better performance, at all FAP values. That figure also shows that the mismatch between the template and the signal families result in a small effect on the detection probability, which is of the order of a few percent at the most.

The variation of detection efficiency with distance also shows the expected behavior. We define it to have the same expression as $P_{\text{detection}}$ in Eq. (3.6), but now $P_{\text{detection}}$, $N_{\text{recovered}}(\rho > \rho_{\text{threshold}})$, and N_{missed} are all computed in multiple distance bins. Figure 3.10 shows the detection efficiencies of the hierarchical coherent and coincident searches at $\rho_{\text{threshold}}$ corresponding to FAP=0 and 10^{-3}. The detection efficiencies for all of the searches are very similar; they begin at 100% for nearby sources and fall off to zero near 2 Gpc, which is the greatest horizon distance [25] of the set of BBH sources simulated here.

3.3.2 The null-stream

Real data is neither Gaussian nor stationary and a statistic that is optimal in Gaussian and stationary noise may not remain so in real data. This makes the case for seeking a more effective detection statistic and signal-based vetoes for LIGO/Virgo science data. An advantage of multi-detector coherent searches is that a detector network with three or more baselines can (over-)determine the two waveform polarizations, in addition to identifying the source location with time-delay triangulation [25]. In such cases, one can form a linear combination of detector time-series outputs that contains no GW signal [34]. Such a combination is called the "null stream". The null stream is consistent with the noise in a detector network, and a noise artifact or a glitch in a detector that is uncorrelated with noise in the other detectors is expected to leave a residue in the null stream. Therefore, its presence can be used to veto a candidate event. The simplest example of the null-stream is the one for a network consisting two co-located, co-aligned detectors. In the simple case where both detectors in such a pair have the same sensitivity, the null stream corresponding to any search template is proportional to the difference of its matched-filter outputs from the data of the two individual detectors. When the two detectors in the pair have different sensitivities, the matched-filter outputs are inversely weighted with their respective template-norms before calculating the difference [8]. The value of the null-stream time-series at the trigger time is called the null statistic.

Figure 3.12 presents the null-statistic distribution for simulations and background events as a function of their coherent SNR.

For very strong signals the null statistic is large since even a slightly imperfect subtraction of two large SNR values can leave a moderately large residue. This is not a major concern since the distribution of loud injections on this plot is well separated from that of the background triggers. However, the null statistic can play a critical role in the detection of weak signals. Those occur in the region where their distribution on this plot mixes with that of the background triggers. Figure 3.12 shows that nearly all the background triggers fall on a relatively tight band and only a couple lie outside it. Those two outliers are also the loudest background triggers in coherent SNR. Interestingly, these are triggers for which the sky positions were such that the LIGO-Virgo network could not resolve the putative signal polarizations. Just as for the injections, for these two triggers too the search pipeline used the coincident statistic as the detection statistic, the values of which were found to be well below 10.0. Therefore, Fig. 3.12 demonstrates that the null statistic is helpful in mitigating the impact of loud background triggers on a search pipeline's detection efficiency.

Although we will not be employing hierarchical search pipelines in ADE it is important to understand its issues in order to improve the efforts on developing fully coherent searches. As shown above, the thresholding criteria used in current coincident and hierarchical coherent pipelines can limit the detection efficiency of the search. In the current pipeline we only analyze triggers that cross the first matched-filtering stage with an SNR greater than 5.5. Additionally, we also require at least two such triggers in two different detectors within the window of light travel time between two sites to claim a gravitational-wave detection. It is possible to have gravitational-wave signals that only have threshold crossing trigger

59

in one detector with significant coherent SNR. To investigate this in the same NR simulations, we searched for such events. Numerical relativity simulations plotted in Fig. 3.16 have only one threshold-crossing detector, yet their coherent SNRs are relatively strong: Out of a total of 2000 simulated pN-NR signal injections, we found that 52 had coherent SNR above 9.5. For each of these found injections only one of the three detectors in coincidence produced a single-detector SNR of above 5.5.[4] Furthermore, 35 of them had a coherent SNR higher than the loudest background trigger. Figure 3.16 reveals that some of these simulations had larger single-detector SNRs in Virgo compared to those in the two LIGO detectors. Due to their similar orientation and sky coverage, both LIGO detectors had very similar sensitivities in a large fraction of the sky. Additionally, their similar noise PSDs means that signals from the same source will have very similar SNRs in those detectors most of the time. But Virgo's orientation is quite different from that of the LIGO detectors. Therefore, in Fig. 3.16 some of the events have larger SNR contributions from Virgo than from any of the LIGO detectors.

3.4 Parameter recovery

Parameter estimation will play an important role in making astrophysical statements about the origin of the GW signals we detect (see, e.g., Ref. [47]). For instance, by measuring the masses of BBH components through GW observations we will be able to constrain stellar population synthesis models. This section presents

---

[4]For a three-detector network with single-detector thresholds of 5.5 each, the minimum combined SNR for an event is $\sqrt{3} \times 5.5 = 9.52$.

results from our EOBNR template searches of pN-NR simulated injections to educate us on how accurately one might be able to measure the parameters of real BBH signals. In this study, parameters of those signals were estimated using the maximum likelihood method [2]. Figure 3.17 shows that the measured coherent SNR is within a few percent of the expected value when for signals the latter exceeds 20. Moreover, this observation holds across the whole range of total-mass values of the injected non-spinning BBH systems.

A useful construct for describing the error in the measurement of the value of a dimensional parameter is:

$$\text{fractional error} = \frac{\text{measured value - injected value}}{\text{injected value}}, \tag{3.7}$$

which we will use especially for studying the error in the measured or *recovered* chirp-mass values. Comparing the injected and recovered parameter values helps us in determining if any systematics can develop in searching for pN-NR signals with a specific waveform family. Consider, e.g., the chirp-mass recovered by EOBNR templates in Fig. 3.18. There, in most cases, the injected chirp mass is greater than the recovered one. This can happen owing to the following possibilities: (a) For some cases of pN-NR waveforms EOBNR templates with a smaller mass have the same or similar number of cycles. If this is true, then this is information that the hybridization schemes of those pN-NR waveforms can use to correct for this bias. (b) Templates that are longer in time and have more cycles than these pN-NR injections perform better at finding them. Longer templates would accrue noise from the cycles that do not overlap with any part of the signal and would, therefore, lose SNR. However a mismatch between an injection and

the template, in amplitude or phase, can cause the projection of the signal on the template manifold to select a longer template as the best fit. Indeed, the chirp-mass recovery and end-time recovery plots reveal that pN-NR injections tend to be found often with relatively higher chirp-mass EOBNR templates. Since higher chirp-mass templates will have a smaller duration than lower chirp-mass ones, all else being the same, one would expect that this bias should be accompanied by a systematic error whereby the template (or recovered) end-time occurs earlier than the injected (pN-NR) end-time. This expectation is confirmed in Fig. 3.21. The end-time difference of recovered simulated signals in Fig. 3.21 is computed by subtracting the injected end time from the measured end time. A negative end-time difference implies that the pN-NR signal is found at a later time than its injected value. A majority of the signals were recovered within 10 msec of the injected end time. A few outliers with a greater positive (smaller negative) end-time difference arise from systems with a large (small) total mass and relatively low coherent SNR.

The results for the measurement of the symmetrized mass-ratio η are presented in Fig. 3.23. The end-time difference is computed by subtracting the injected value from the measured one. As shown in Ref. [62], only six mass-ratio values were used to model and inject non-spinning pN-NR signals. For EOBNR signals, we produced a greater variety of mass ratios and, therefore, η, as can be seen in the top-right plot in that figure. The measured values of η are always between 0.00 and 0.25 because those are the boundaries of the template bank that was employed, and correspond to mass ratios of infinity and 1, respectively. It is interesting to note that in a large fraction of cases small (large) η, or low (high)

mass ratio, templates detect large (small) η signals. This bias is, in fact, correlated with low (high) chirp-mass templates detecting high (low) chirp-mass signals, as confirmed by Fig. 3.26 for injections of pN-NR as well as EOBNR signals. This covariance of errors occurs because templates with low (high) η and low (high) $M_{\rm chirp}$ can have similar number of wave cycles and bandwidths as signals with high (low) η and high (low) $M_{\rm chirp}$.[5] In the same figure, also note how the degree of covariance changes somewhat as one goes from low total-mass systems (shown in blue) to high total-mass systems (shown in red). A similar behavior was observed in the Monte Carlo studies in Ref. [47] of statistical errors in measuring BBH mass parameters with phenomenological waveforms [76].

3.5   Gaussian vs real detector noise

Although we test performance of data analysis pipelines on Gaussian and stationary data, our ultimate goal is to improve the performance of real data searches. In past searches we employed different techniques such as data quality and signal-based vetoes to avoid of non-Gaussian features of real detector data. However, even with the most efficient vetoes we have today, in most searches non-Gaussianity and non-stationary of real detector data hurt the performance of GW searches. To study this situation in ADE searches, we compared performance of the CBC ihope search pipeline in Gaussian and real detector data. The simulated Gaussian data set was created using early aLIGO and Advanced Virgo predicted curves for 2015.

[5]A similar correlation of errors in η and the total-mass M was found in Ref. [60] where the effect of using inspiral-only templates for searching inspiral-merger-ringdown signals on detection and parameter estimation was studied.

As we did in the studies presented in earlier sections of this chapter, we rescaled Virgo noise curve get similar horizon distance in both LIGO and Virgo detectors. The real data set was created by recoloring LIGO S6 and Virgo VSR2/3 data to match above motioned noise curves. Data selected from S6 and VSR2/3 were collected from different times so that no real GW coincident will not appear in recolored data. This was the same method use for NINJA-2 mock data challenge presented in Ref. [6].

Figure 3.27 presents the comparison of Gaussian and real data search. In this study we used publicly available NINJA-2 GW waveforms [62] as simulations. Same set of simulations were used in both Gaussian and real data sets. This set consist approximately 1500 pN-NR hybrid simulations to make the comparison fair. While Gaussian search recovered approximately 860 simulations real data search only found approximately 580 injections. For both searches we used EOBNR waveforms as templates. Ultimately these numbers reveal the detection efficiency at highest FAP. The gap between detection efficiency of Gaussian and real search is consistent for all FAP values. This comparison is very important as it analysis performance of two cases under exact same conditions such as number of simulations and sensitivity of detectors. Only difference in two searches is the real data features appear in one data set compared to Gaussian and stationary features in the other. Most probably detection efficiency deficit was created by this difference. Our goal is to reduce this gaps as much as possible for future searches. More effective data quality vetoes and signal-based vetoes can paly an important role in ADE searches. Since this was a highmass search it is also possible signal-based vetoes do not operate with best efficiency. Therefore, one important data point will be to

do the same comparison for lowmass simulations. Two curves in Fig. 3.27 suggest real data curve reach low FAP values than Gaussian counterpart. This is due to the number of background events in two different searches. Compared to approximately $18,000$ background events real data search had $54,000$ events due to its nature. This allows to go for less FAP values similar to a extended background estimation explained in blind injection recovery and NINJA-2 mock data challenge of next two chapters. Also it is important to note this study used approximately 1500 non-spinning BBH simulations and in future efforts it will be useful to have much larger set of simulations of all kinds such as spinning and high mass ratio simulations.

3.6   Comparison of different mass ratio waveforms

Among the public waveforms submitted to NINJA-2 project, there were number of waveforms with different mass ratios. We studied the detection efficiency of different mass ratio waveforms using EOBNR templates. In this study we injected approximately 1500 non-spinning waveforms in simulated Gaussian noise. We did four different analyses with simulated GW signals, with the values of mass ratios $1, 2, 3$ and 4. Figure 3.28 presents the results. Interestingly, with the increase of mass ratio of the simulations, detection efficiency decreased. Although the drop of detection efficiency was relatively small this feature was consistent for all the FAP values. Overall this shows the equal mass ratio simulations had the best match to the templates we used. However, it is important to note among same mass ratio signals, it is possible to have differences in waveforms submitted based on the

group that produced the waveforms. Reference [62] shows some plots for overlap of different waveforms submitted by different groups. Therefore, a complete study will have detailed analysis about all these different waveforms. In our study we only used waveforms up to mass ratio 4 due to limited number of waveforms available for higher mass ratios than 4.

3.7 Discussion

Testing the preparedness of search pipelines to detect real signals in the ADE is one of the primary goals of NINJA. This study helped to quantify the sensitivity of one of the existing CBC search pipelines to numerical-relativity based BBH waveforms in early advanced detectors *albeit* in simulated Gaussian, stationary data. As we found here, the EOBNR waveforms, which employed only NASA-Goddard NR waveforms for calibration, were able to detect pN-NR signals produced by a number of NR collaborations. This is borne out by the fact that the ROC curve of EOBNR injections tracks that of the NR injections very closely. Additionally, we studied some aspects of a coherent CBC search. Since a coherent search explores a larger dimensional parameter space than a coincident search it is more expensive, which makes the estimation of the background for the former type of search especially difficult. Therefore, we used the hierarchical coherent CBC search pipeline described in Ref. [8] on the same NR based injections. Such an exercise is also useful to teach us about a subset of the potential issues we may face in a fully coherent search in the future. Here we demonstrated that the performance of that search conforms to expectations. Specifically, the characteristics of its background

are consistent with theoretical predictions. Moreover, the coherent stage provides the null-stream statistic, which is a powerful multi-baseline signal consistency test, and can be employed to improve the performance of the search. This test is especially useful for high-mass CBC searches where the chi-square test is less effective than low-mass ones, owing to fewer waveform cycles of high-mass signals in the detector band.

Finally, NINJA provided an important opportunity to test how well we might be able to measure the signal parameters. To address this question, we compared the maximum-likelihood estimates obtained by using the EOBNR family of templates. We focused our attention on only non-spinning injections. Here again the parameter accuracies of EOBNR injections are very similar to those of the pN-NR ones. The only small disagreement occurs for a few injections, mainly in the small total-mass region. For most of them, its cause was traced to the fact that compared to other injected waveforms these ones were *a priori* known to have a somewhat poorer match (by a few percent) [62] with the waveforms produced by the Spectral Einstein Code (SpEC). (See Ref. [77] for details about SpEC.) To study systematic errors stemming from signal-template mismatch in more detail, studies are ongoing with NR waveforms with spin and a variety of different mass ratios. Additionally, to study the impact of real data, which can be non-Gaussian and non-stationary, we plan to study the NINJA-2 waveforms injected in a recolored data set, where real data from past science runs will be scaled to have early aLIGO or aLIGO ASDs [69].
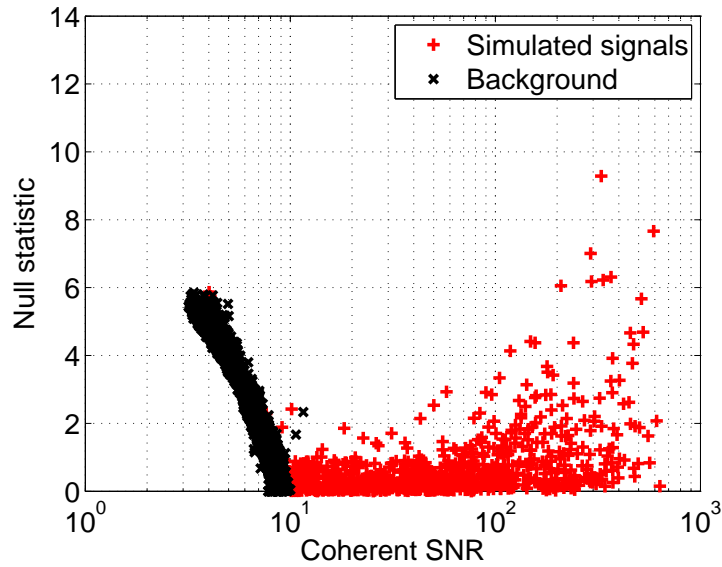
Figure 3.12: We plot the null-statistic for background and pN-NR simulated signals as a function of their coherent SNR. Most of the background triggers form a "band", which helps to separate signals from them. Notice that two of the loud background triggers prominently fall outside the band. These correspond to sky positions where the network does not resolve the GW polarizations very well [8]. In such a case, the trigger is vetoed. A better way to handle such triggers would be to not veto them but construct a more effective detection statistic by using a network's polarization resolving power at the trigger's sky position. This aspect will be explored elsewhere.
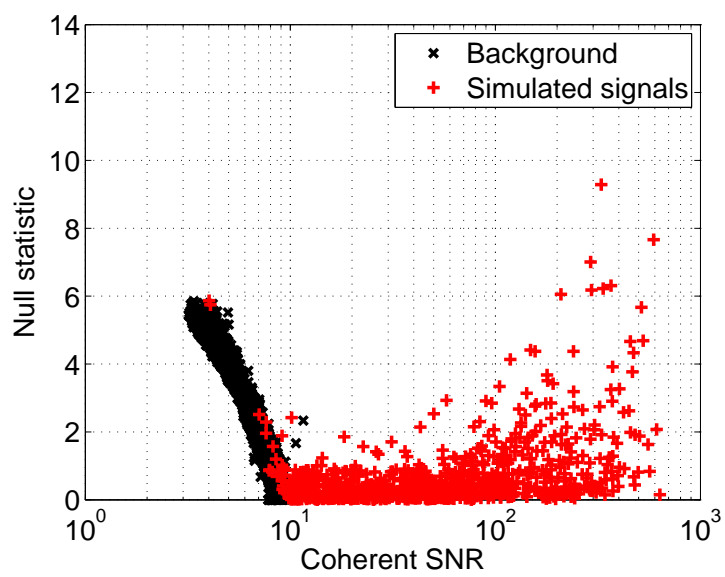
Figure 3.13: Here we show the injection triggers above the background triggers to highlight that for very weak injections, the null-statistic worsens and loses its discriminatory power.
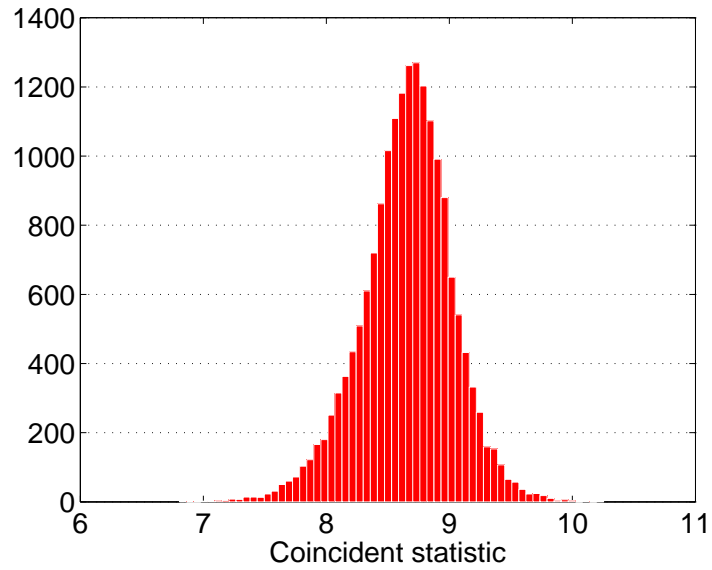
Figure 3.14: Distribution of background events in the coincident detection statistic used for the LIGO S6 - Virgo VSR2/3 high-mass search.
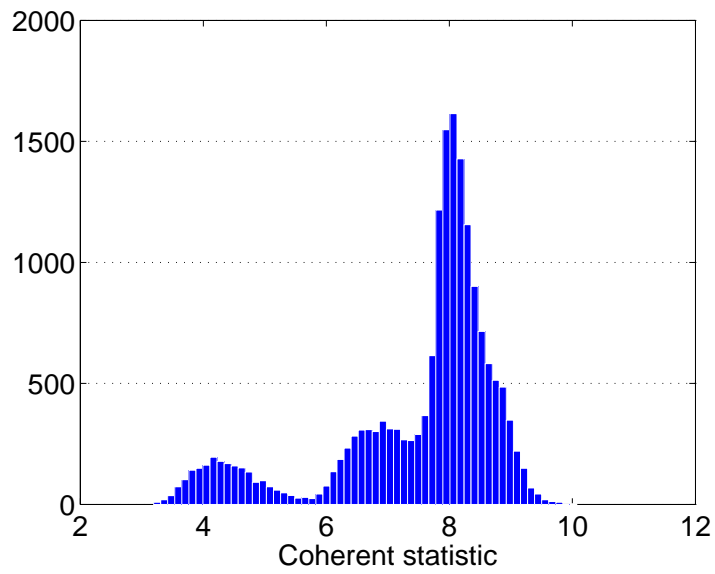
Figure 3.15: Distribution of background events in the coherent detection statistic.
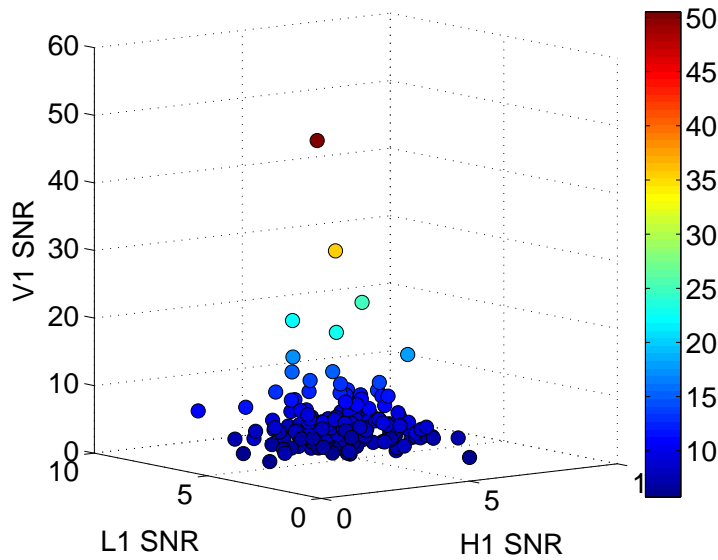
Figure 3.16: The coincident pipeline uses thresholds on matched-filter outputs from all detectors in a network to keep the number of background trigger coincidences at a manageable level so that the search remains computationally viable. An event has to be coincident in at least two detectors before it can be treated as a detection candidate. While this requirement improves confidence in a detection, it also hurts detection efficiency by rejecting signals with marginally sub-threshold triggers in two of three detectors that would otherwise produce a candidate event with comparable detection confidence. This plot shows the distribution of such events, with the colorbar displaying their coherent SNR. Out of 2000 simulated pN-NR signals, 48 were found with a zero false-alarm rate that have the SNR crossing the standard 5.5 threshold in only one of the three detectors. Also 54 events were found that had SNR crossing the standard 5.5 threshold in all three detectors.
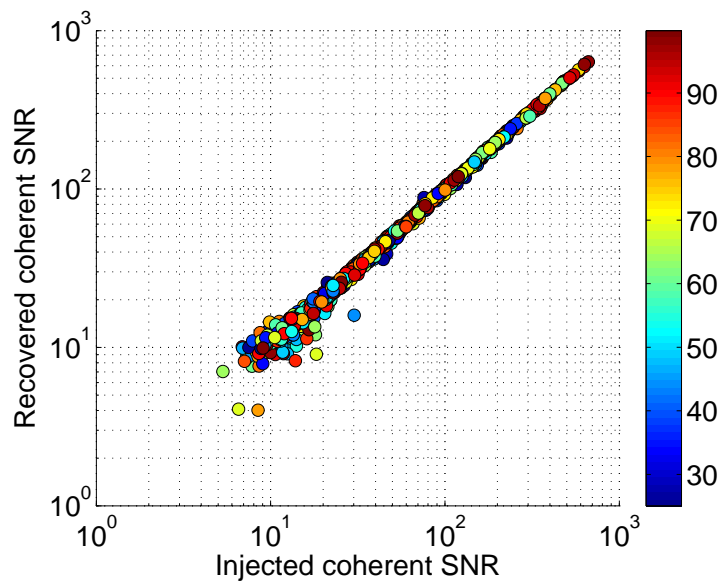
Figure 3.17: Recovered coherent SNR versus its injected value for NR simulated signals. The colorbar shows the total mass of the BBH systems whose pN-NR hybrid waveforms were injected.
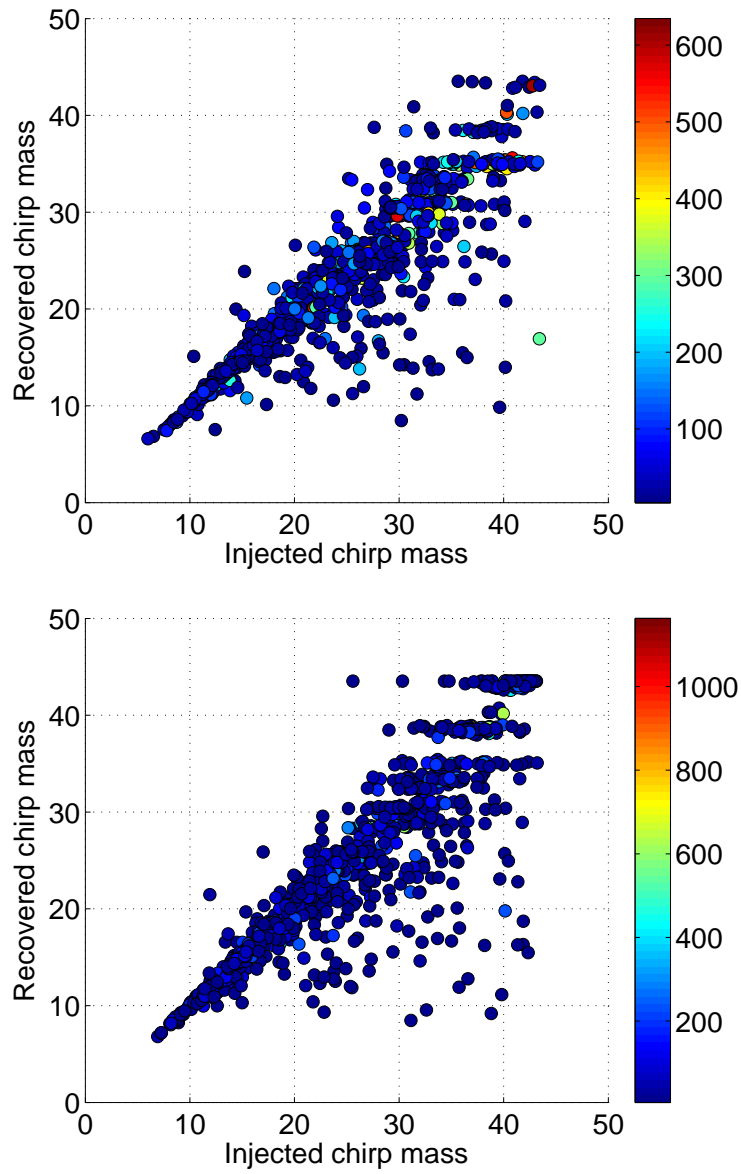
Figure 3.18: Recovered chirp mass as a function of injected chirp mass for pN-NR simulations (top) and EOBNR simulations (bottom), with the colorbar showing the coherent SNR.
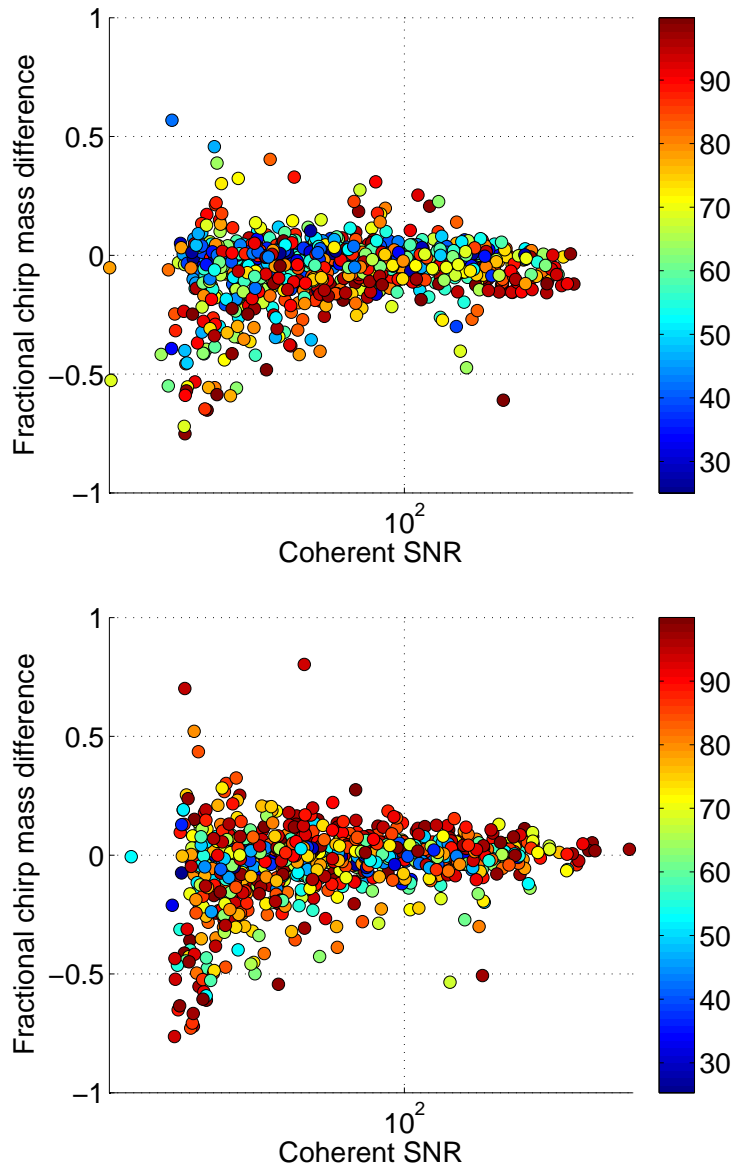
Figure 3.19: Fractional chirp-mass difference as a function of coherent SNR with the colorbar displaying the total mass of the BBH system. Top and bottom figures are for pN-NR and EOBNR respectively.
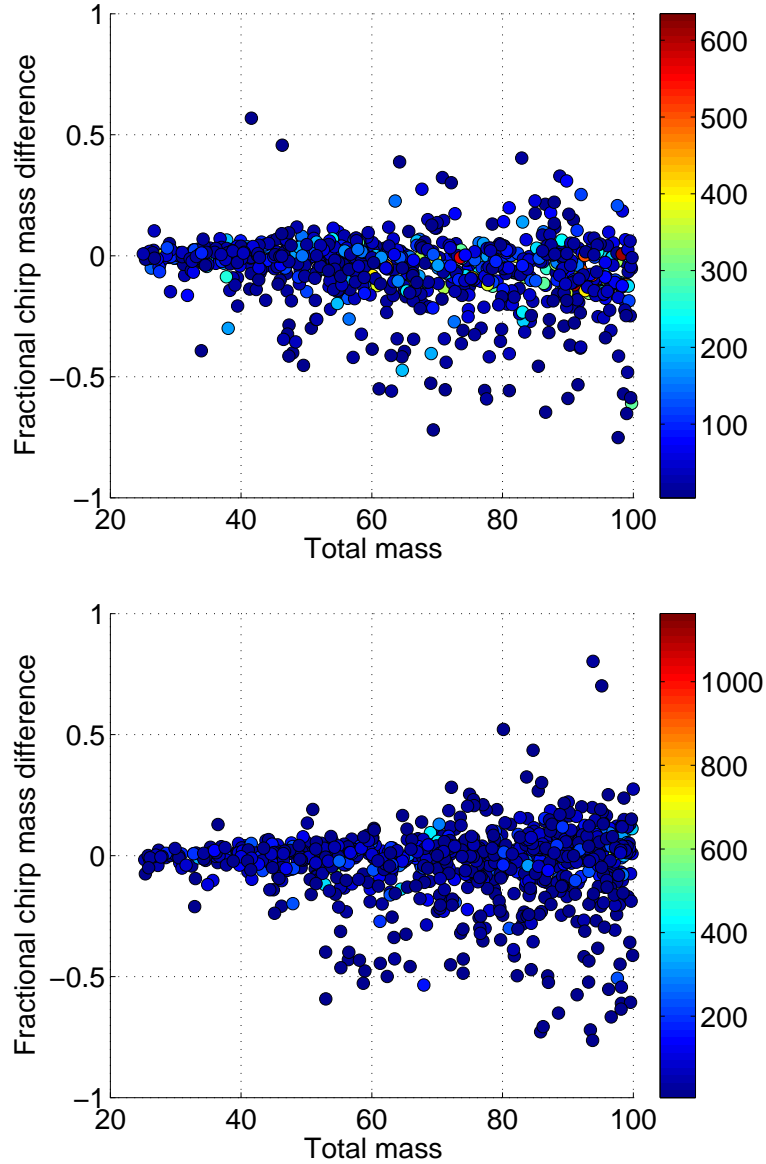
Figure 3.20: Fractional chirp-mass difference as a function of the total mass of the BBH system, with the colorbar showing the coherent SNR. According to the bottom panel the overall chirp mass recovery is slightly better for EOBNR simulations than the pN-NR ones, due to better match with the templates in the former case.
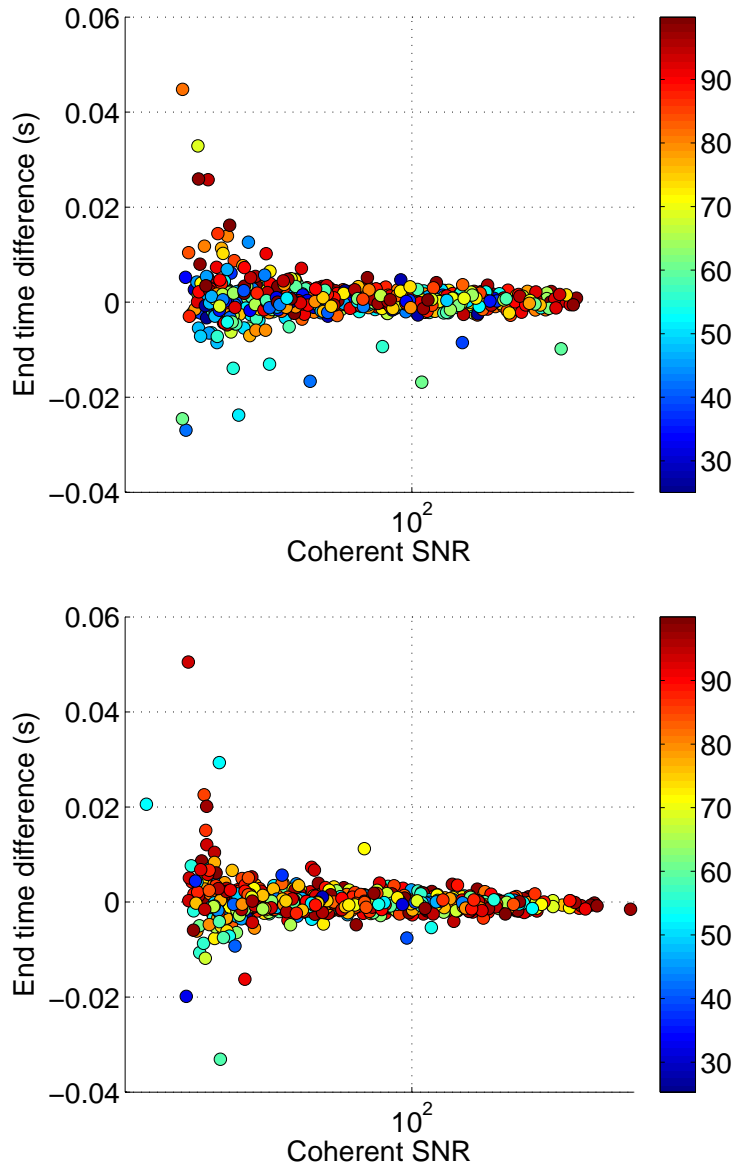
Figure 3.21: Difference between the measured and injected end time of detected simulated signals (in seconds). The Left figure is the end-time difference is plotted as a function of the coherent SNR for pN-NR simulations. The colorbar represents the total mass of the binary system (in $M_\odot$). The bottom plot shows same quantity is plotted for EOBNR simulations.
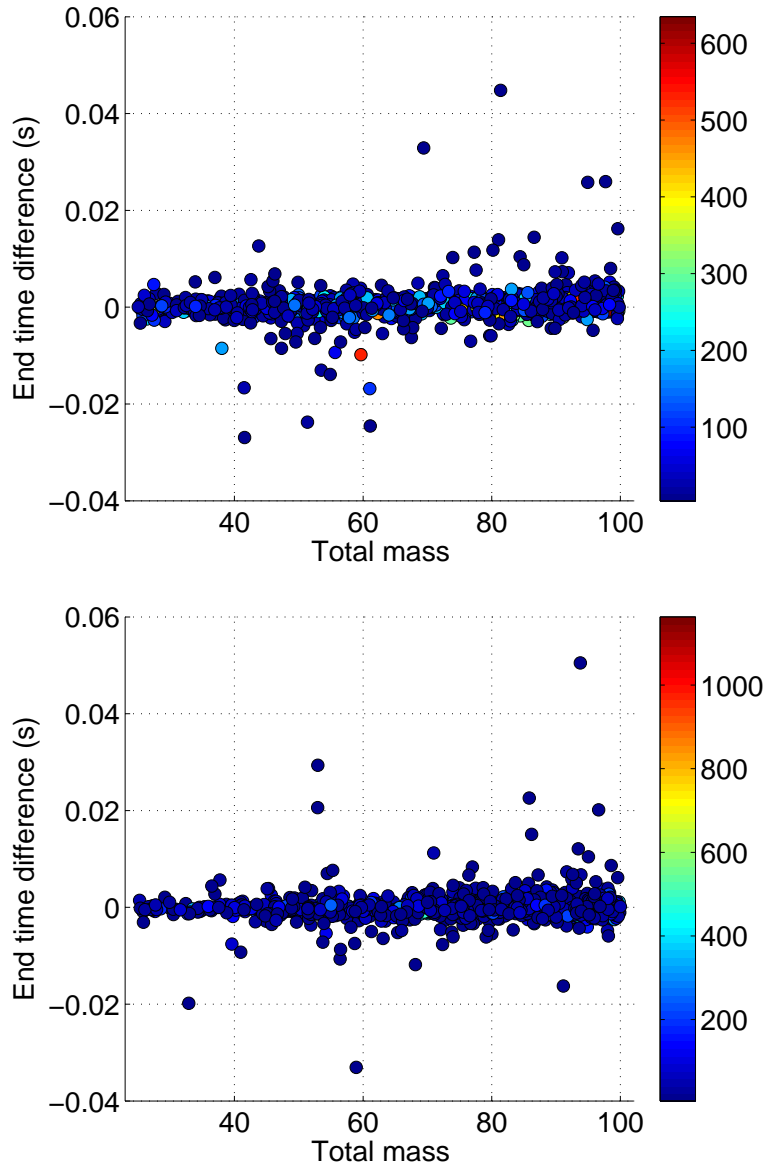
Figure 3.22: Difference between the measured and injected end time of detected simulated signals (in seconds). The end-time difference is plotted as a function of the total mass of the system. For pN-NR simulated signals (top) a few were recovered with relatively high negative end-time difference, i.e., ≥ 0.01 sec, in the total-mass range $40M_\odot$ to $62M_\odot$, at both high and low coherent SNRs.
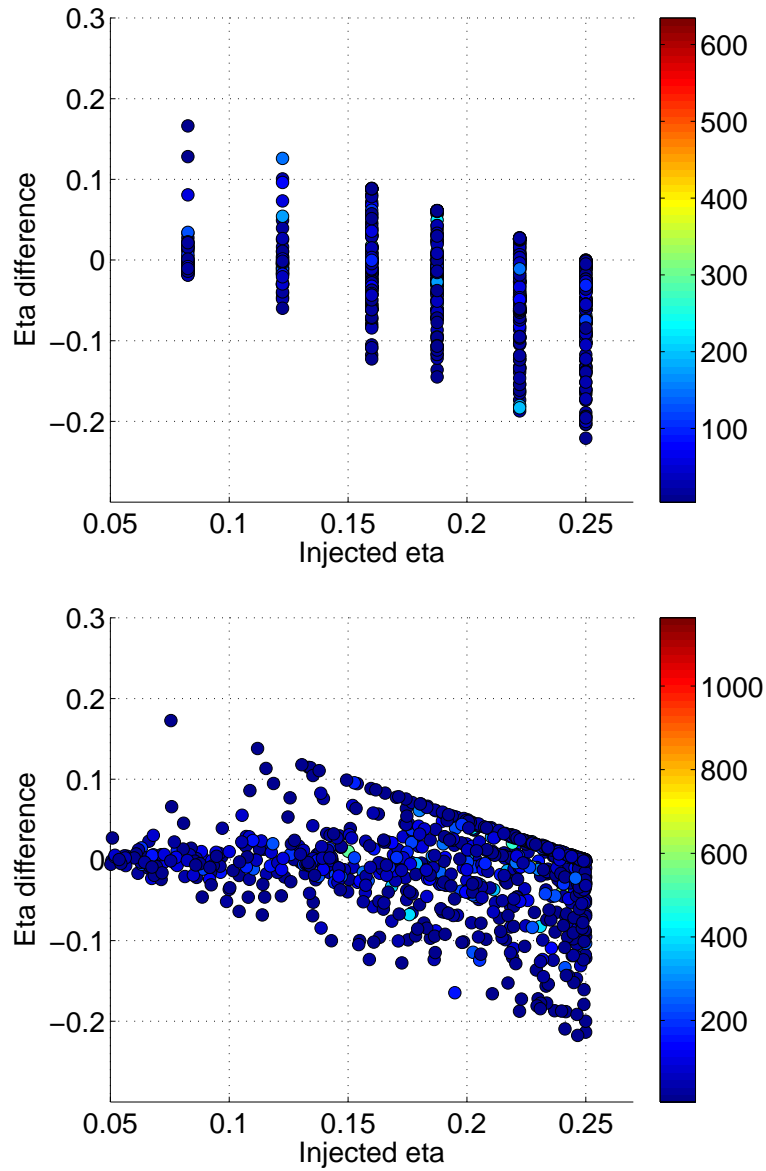
Figure 3.23: This figure shows the η difference as a function of injected η values. Since pN-NR simulations are only available for a discrete set of η values the top plot only has a few different values of injected η compared to EOBNR counterpart, which is plotted in the bottom. Since $\eta \in (0, 0.25]$, the maximum (minimum) η difference is 0.25 (-0.25).
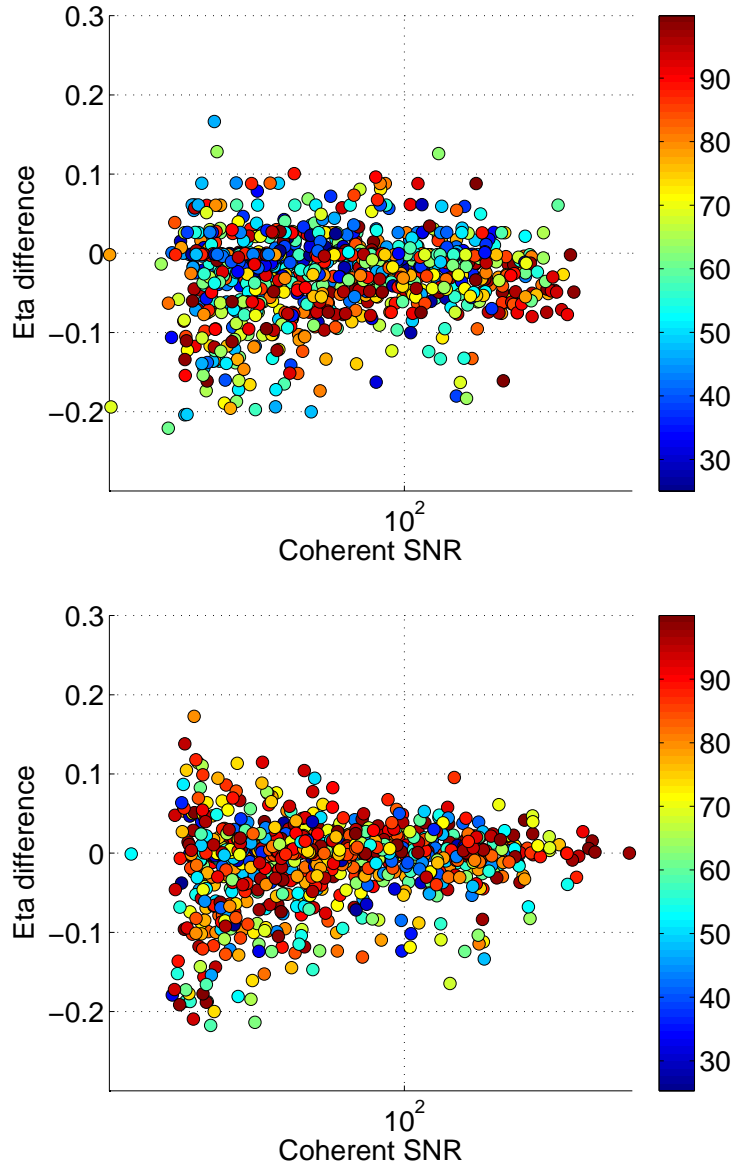
Figure 3.24: This panel shows that the η difference of pN-NR hybrids is slightly worse compared to that of EOBNR simulations due to template mismatch. This is most apparent above at large coherent SNR values. The colorbar denotes the total mass of the binary system.
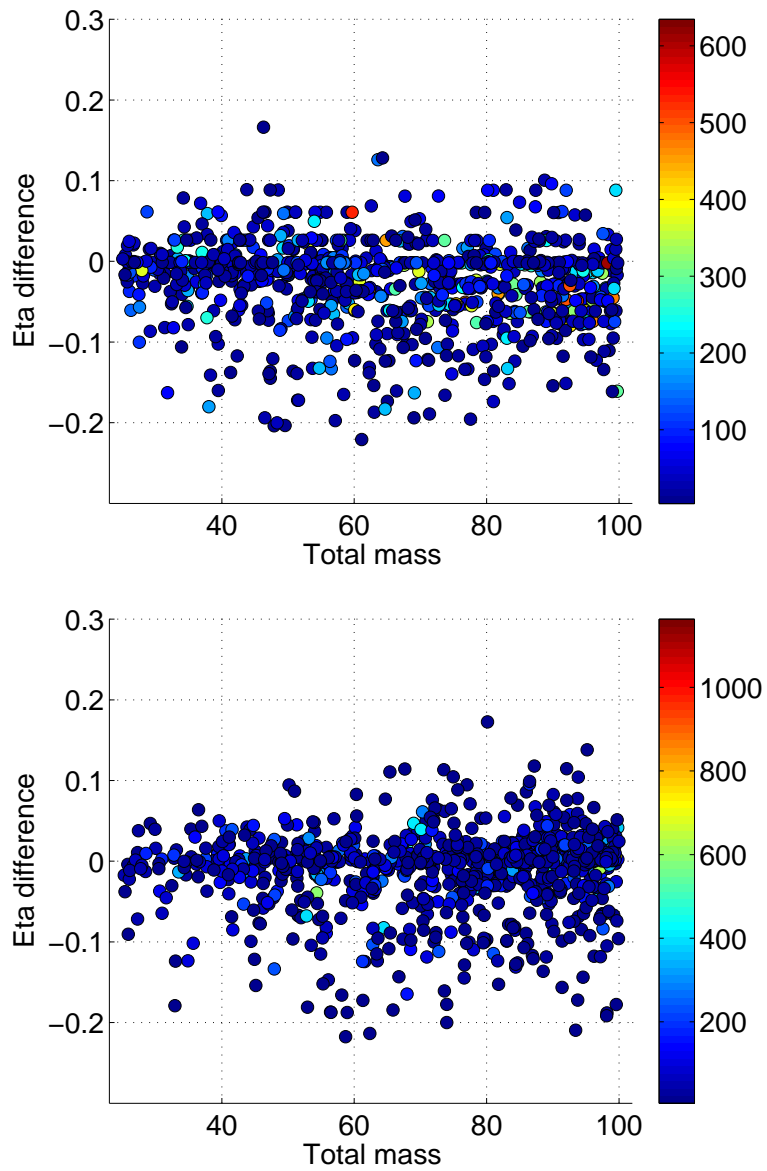
Figure 3.25: Eta difference of two simulation categories is shown as a function of the total mass of the system.
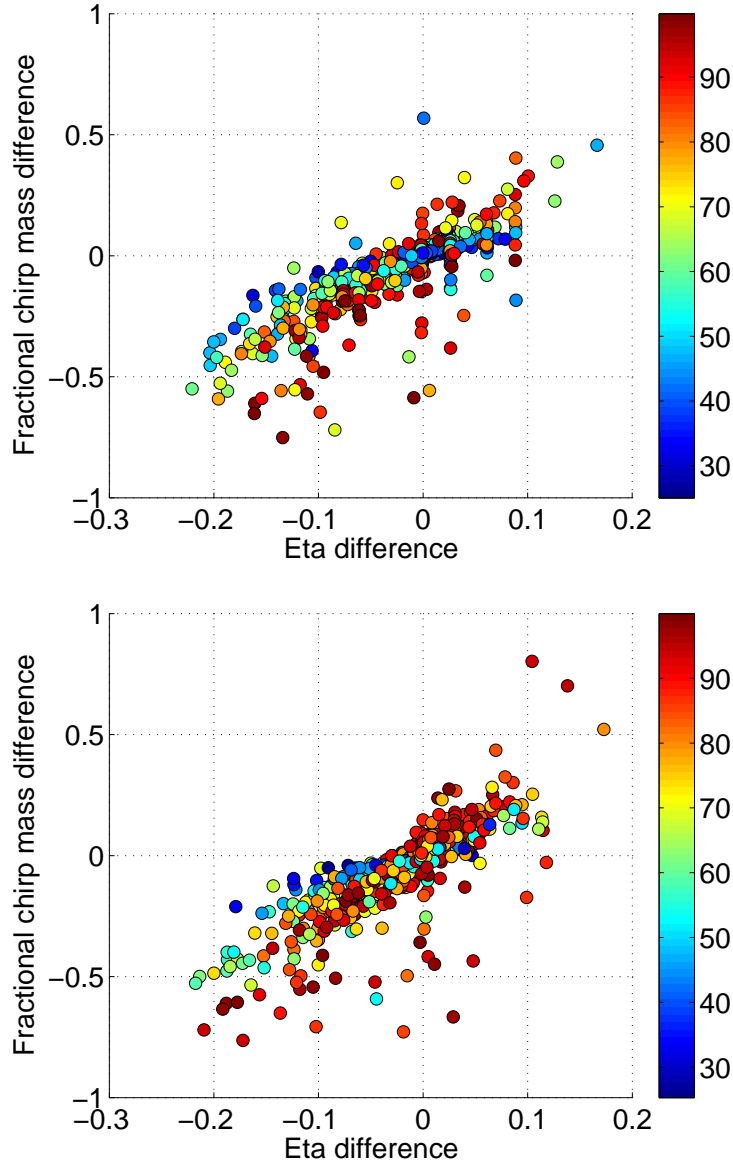
Figure 3.26: Covariance of chirp-mass error with η error. The top figure shows this covariance for pN-NR injections and the bottom figure shows it for EOBNR injections. In both cases EOBNR templates were used to conduct the search. The colorbar shows the total mass of the BBH systems (in $M_\odot$).

81
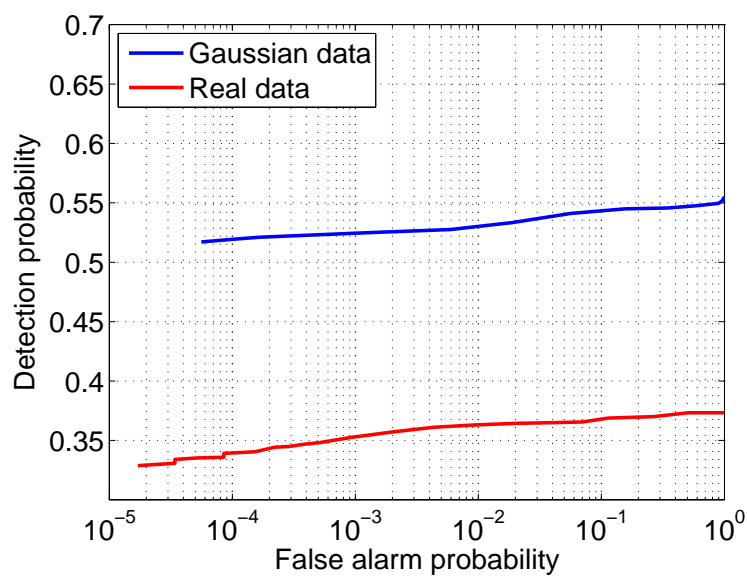
Figure 3.27: This ROC curve compares the performance of CBC coincidence pipeline in Gaussian and real detector data. We injected same set of injections in Gaussian and real detector data and recovered the injections running the CBC ihope pipeline.
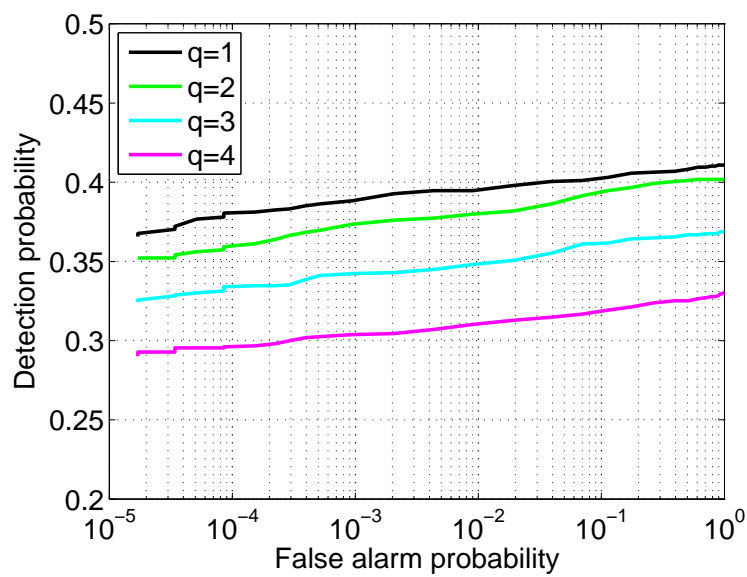
Figure 3.28: This ROC curve compares the performance of CBC coincidence pipeline in recovering different mass ratio NINJA-2 waveforms in real detector data. We injected same set of injections and recovery shows better performance for low mass ration waveforms.

Chapter 4

The Ninja-2 project: Mock data challenge

4.1 Introduction

As described in chapter 3 the NINJA project is a collaboration between members of the numerical relativity and GW data analysis communities. The main purpose of NINJA is to study the sensitivity of existing gravitational-wave search and parameter-estimation algorithms in detecting numerically simulated waveforms, and to foster closer collaboration between the numerical relativity and gravitational-wave astrophysics communities. Chapter 3 and Ref. [62, 64] give more details about differences between the first version of NINJA (i.e. NINJA-1) and the NINJA-2 projects. They also present studies conducted using NINJA-2 waveforms in Gaussian data. This chapter focuses on studies that used recolored real detector noise [6]. The NINJA-2 mock data challenge is a NINJA collaboration

wide exercise that allowed us to compare performances of different GW search and parameter estimation pipelines to pN-NR waveforms in early ADE. In this study we inject selected NINJA-2 waveforms in to recolored simulated early advanced detector data and try to recover them with different search pipelines. Additionally we also discuss about NINJA-2 waveforms in this chapter and the results of the mock data challenge using CBC search pipelines. In a mock data challenge we compare the performances of different data analysis pipelines by recovering same injected signals in a common data set.

4.2 NINJA-2 binary black hole waveforms

The first edition of NINJA project considered 23 waveforms submitted by various NR groups [62]. These waveforms were injected into simulated Gaussian noise colored with the frequency sensitivity of initial LIGO and Virgo. These data sets, with added numerically-modelled, physically-realistic GW signals, were analyzed by nine data-analysis groups using both detection and parameter-estimation algorithms. Although NINJA-1 was a successful effort, there were two major limitations that demanded next edition of more sophisticated projects. First, to attract more NR groups, no length or accuracy requirements were placed on the contributed numerical waveforms. Consequently, many of the waveforms were too short to inject over an astrophysically interesting mass range without introducing artifacts into the data. Second the data set used for injection of NR waveforms was Gaussian and stationary. Lack of non-Gaussian and non-stationary features did not allow full exploration of the performances of detection and parameter estimation

pipeline in a realistic setting.

The main purpose of the NINJA-2 project is to overcome these limitations. As a result 60 pN-NR hybrid waveforms submitted by eight numerical relativity groups to build the waveform catalog. The catalog of the waveforms and procedures used to validate these waveforms are presented in Ref. [62]. This section presents a brief summary of the NINJA-2 waveform catalog.

All the waveforms in the NINJA-2 catalog include all three inspiral-merger-ringdown phases of binary coalescence. Each waveform consists of a post-Newtonian portion modelling the early inspiral phase stitched to a numerical portion modelling the late inspiral, merger and ringdown phases. For every waveform it was required that for its NR portion, the amplitude be accurate to within 5% and the phase (as a function of gravitational-wave frequency) have an accumulated uncertainty of no more than 0.5 radian. NINJA-2 also required that the NR portion have at least five orbits in order to ensure robust blending with the post-Newtonian portion. Additionally, It was decided to limit NINJA-2 to systems without eccentricity, and with the black-hole component angular momenta (spins) parallel or anti-parallel to the orbital angular momentum. This last condition avoids precession and was imposed for two reasons. First, precession greatly complicates waveform phenomenology and, the collaboration preferred to first tackle a simpler subset that still retains the main features of binary evolution and merger. Second, at the start of NINJA-2 the precessing-binary parameter space had been sampled by only a handful of numerical simulations [62].

Tables 4.1 and 4.2 present the details of the waveforms submitted to the NINJA-2 project. To refer to these waveforms in later sections, we follow the notation

used in Ref. [6]. As discussed there, a sample waveform "`G2+20+20_T4`" is constructed as follows: The first letter represents the group submitting the numerical simulation, namely:

F: The numerical relativity group at Florida Atlantic University [78, 79, 80, 81].

G: The Georgia-Tech group [82, 83, 84, 85, 86, 87, 88].

J: The BAM (Jena) code, as used by the Cardiff-Jena-Palma-Vienna collaboration [89, 90, 91, 92, 93, 94].

L: The Lean Code, developed by Ulrich Sperhake [95, 96].

Ll: The Llama code, used by the AEI group and the Palma-Caltech groups [97, 98, 99].

R: The group from Rochester Institute of Technology [100, 101, 102, 103].

S: The SXS collaboration using the SpEC code [104, 105, 106, 107, 108, 109, 110, 77, 111, 112].

U: The group from The University of Illinois [113].

Right next to first letter of the label, follows the value of the mass-ratio $q = m_1/m_2$, where the masses are assigned such that $q \geq 1$. The next two numbers are the components of the initial dimensionless spins along the orbital angular momentum, multiplied by 100 (e.g. '+20' corresponds to $\hat{L} \cdot \vec{S}_1/m_1^2 = 0.2$), of the more massive and the less massive black hole respectively. The last two characters of the above label denote the Taylor-approximant being used for the PN portion
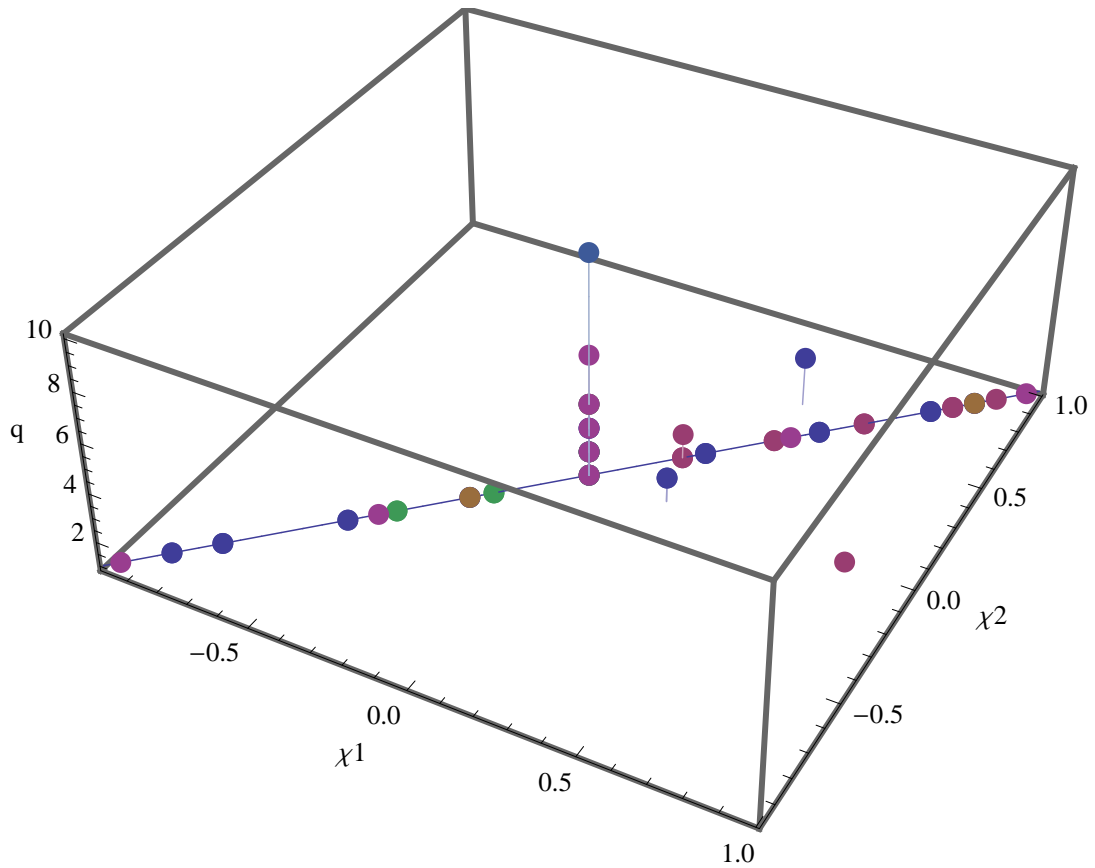
Figure 4.1: Mass ratio q and dimensionless binary component spins χ_i of the NINJA-2 hybrid waveforms.

of the waveform, with "T1" and "T4" representing TaylorT1 and TaylorT4, respectively. However, the Georgia-Tech group submitted four pairs of simulations where within each pair the same system was simulated with identical physical parameters, stitched to the same post-Newtonian approximant. The two waveforms in a pair, however, are not identical since each one has a different number of NR cycles and was generated at a different resolution. Such waveforms are distinguished by appending "_1" and "_2" to the label.

Label	q	χ_1	χ_2	$1000e$	$100\,M\omega$ hyb.range	# NR cycles	pN Approx
S1-95-95_T1	1.0	-0.95	-0.95	1.00	3.3 – 4.1	18.42	T1
J1-85-85_T1	1.0	-0.85	-0.85	2.50	4.1 – 4.7	12.09	T1
J1-85-85_T4							T4
J1-75-75_T1	1.0	-0.75	-0.75	1.60	4.1 – 4.7	13.42	T1
J1-75-75_T4							T4
J1-50-50_T1	1.0	-0.50	-0.50	2.90	4.3 – 4.7	15.12	T1
J1-50-50_T4							T4
S1-44-44_T4	1.0	-0.44	-0.44	0.04	4.3 – 5.3	13.47	T4
Ll1-40-40_T1	1.0	-0.40	-0.40		6.1 – 8.0	6.42	T1
Ll1-40-40_T4							T4
J1-25-25_T1	1.0	-0.25	-0.25	2.50	4.5 – 5.0	15.15	T1
J1-25-25_T4							T4
Ll1-20-20_T1	1.0	-0.20	-0.20		5.7 – 7.8	8.16	T1
Ll1-20-20_T4							T4
J1+00+00_T1	1.0	0.00	0.00	1.80	4.6 – 5.1	15.72	T1
J1+00+00_T4							T4

Label	q	χ_1	χ_2	$1000e$	$100\,M\omega$ hyb.range	# NR cycles	pN Approx
G1+00+00_T4				3.00	5.5 – 7.5	9.77	T4
Ll1+00+00_F2					5.7 – 9.4	8.30	F2
S1+00+00_T4				0.05	3.6 – 4.5	22.98	T4
G1+20+20_T4_1	1.0	0.20	0.20	10.00	6.0 – 7.5	6.77	T4
G1+20+20_T4_2				6.00	5.5 – 7.5	10.96	T4
J1+25+25_T1	1.0	0.25	0.25	6.10	4.6 – 5.0	18.00	T1
J1+25+25_T4							T4
G1+40+40_T4_1	1.0	0.40	0.40	10.00	5.9 – 7.5	7.70	T4
G1+40+40_T4_2				6.00	5.5 – 7.5	12.02	T4
Ll1+40+40_T1					7.8 – 8.6	6.54	T1
Ll1+40+40_T4							T4
S1+44+44_T4	1.0	0.44	0.44	0.02	4.1 – 5.0	22.39	T4
J1+50+50_T1	1.0	0.50	0.50	6.10	5.2 – 5.9	15.71	T1
J1+50+50_T4							T4
G1+60+60_T4_1	1.0	0.60	0.60	12.00	6.0 – 7.5	8.56	T4
G1+60+60_T4_2				5.00	5.5 – 7.5	13.21	T4

Label	q	χ_1	χ_2	$1000e$	$100\,M\omega$ hyb.range	# NR cycles	pN Approx
J1+75+75_T1	1.0	0.75	0.75	6.00	6.0 – 7.0	14.03	T1
J1+75+75_T4							T4
G1+80+00_T4	1.0	0.80	0.00	13.00	5.5 – 7.5	12.26	T4
G1+80+80_T4_1	1.0	0.80	0.80	14.00	5.9 – 7.5	9.57	T4
G1+80+80_T4_2				6.70	5.5 – 7.5	14.25	T4
J1+85+85_T1	1.0	0.85	0.85	5.00	5.9 – 6.9	15.36	T1
J1+85+85_T4							T4
U1+85+85_T1				20.00	5.9 – 7.0	15.02	T1
G1+90+90_T4	1.0	0.90	0.90	3.00	5.8 – 7.5	15.05	T4
S1+97+97_T4	1.0	0.97	0.97	0.60	3.2 – 4.3	38.40	T4

Table 4.1: Summary of the contributions to the NINJA-2 waveform catalog with $m_1 = m_2$. Given are an identifying label, mass-ratio $q = m_1/m_2$ which is always 1 for these simulations, magnitude of the dimensionless spins $\chi_i = S_i/m_i^2$, orbital eccentricity e, frequency range of hybridization in $M\omega$, the number of numerical cycles from the middle of the hybridization region through the peak amplitude, and the post-Newtonian Taylor-approximant(s) used for hybridization.

Label	q	χ_1	χ_2	$1000e$	$100\,M\omega$ hyb.range	# NR cycles	pN Approx
J2+00+00_T1	2.0	0.00	0.00	2.30	6.3 – 7.8	8.31	T1
J2+00+00_T4							T4
G2+00+00_T4				2.50	5.5 – 7.5	10.42	T4
Ll2+00+00_F2					6.3 – 9.4	7.47	F2
S2+00+00_T2				0.03	3.8 – 4.7	22.34	T2
G2+20+20_T4	2.0	0.20	0.20	10.00	5.6 – 7.5	11.50	T4
J2+25+00_T1	2.0	0.25	0.00	2.00	5.0 – 5.6	15.93	T1
J2+25+00_T4							T4
J3+00+00_T1	3.0	0.00	0.00	1.60	6.0 – 7.1	10.61	T1
J3+00+00_T4							T4
S3+00+00_T2				0.02	4.1 – 5.2	21.80	T2
F3+60+40_T4	3.0	0.60	0.40	1.00	5.0 – 5.6	18.89	T4

Label	q	χ_1	χ_2	$1000e$	$100\,M\omega$ hyb.range	# NR cycles	pN Approx
J4+00+00_T1	4.0	0.00	0.00	2.60	5.9 – 6.8	12.38	T1
J4+00+00_T4							T4
L4+00+00_T1				5.00	5.1 – 5.5	17.33	T1
S4+00+00_T2				0.03	4.4 – 5.5	21.67	T2
S6+00+00_T1	6.0	0.00	0.00	0.04	4.1 – 4.6	33.77	T1
R10+00+00_T4	10.0	0.00	0.00	0.40	7.3 – 7.4	14.44	T4

Table 4.2: Summary of the contributions to the NINJA-2 waveform catalog, with $m_1 > m_2$. Given are a waveform identifying label, mass-ratio $q = m_1/m_2$ magnitude of the dimensionless spins $\chi_i = S_i/m_i^2$, orbital eccentricity e, frequency range of hybridization in $M\omega$, the number of numerical cycles from the middle of the hybridization region through the peak amplitude, and the post-Newtonian Taylor-approximant(s) used for hybridization.
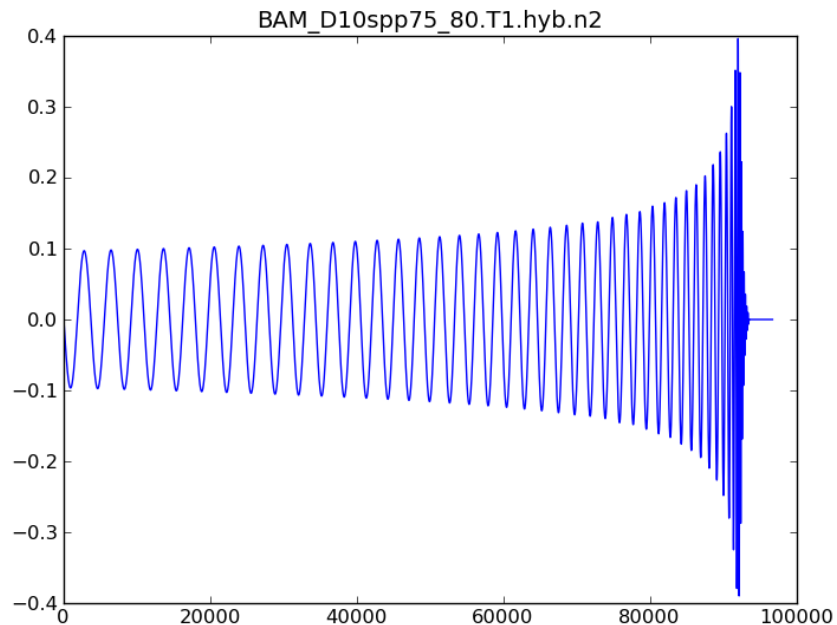
Figure 4.2: A waveform submitted to NINJA-2 waveform catalog. This plot shows the waveform in time domain. The same waveform in frequency domain is shown in Fig. 4.3.

4.3 The blind injection challenge

One major goal of NINJA-2 is to evaluate the performance of search pipelines and parameter estimation methods for LIGO, Virgo GW searches using noise curves predicted for 2015-2016. In order to create data sets with predicted 2015-2016 sensitivities, two-month long stretches of initial detector data were recolored. However, it was clear that projected sensitivity of the early advanced Virgo detector is significantly greater than that of the early Advanced LIGO detectors. To simplify the analysis we rescaled down the early advanced Virgo noise curve by a
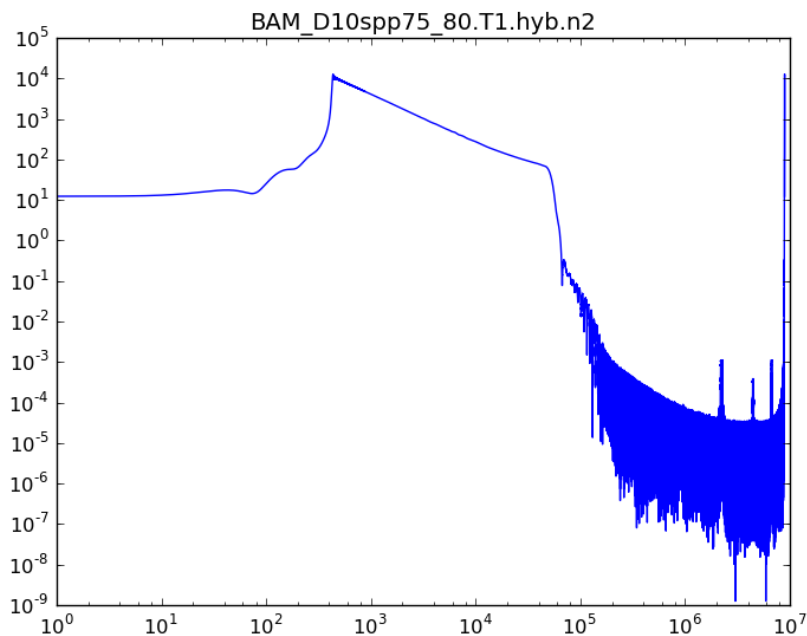
Figure 4.3: The frequency domain representation of the waveform shown in Fig. 4.2.

factor of 1.61. With this rescaling the sensitivities of the two different simulated detector data sets match. A detailed description of the recoloring process can be found in Ref. [6].

To measure the recovering accuracy of NINJA-2 BBH signals, 7 waveforms were added to the recolored data sets. The analysts were aware that "blind injections" had been added; however, the number and parameters of these simulated signals were not disclosed until the analyses were completed. This was similar to blind injection tests conducted by the LIGO and Virgo collaborations in their latest science runs [9]. These injections (simulated signals) are self-blinded to ensure that no bias from knowing the parameters of the signal, or indeed whether a candidate

Waveform label	q	M ($M_\odot$)	χ	RA (rad)	Dec. (rad)	Dist. (Mpc)	Detectors Online	Hybrid Range (Hz)
J4+00+00_T4	4	124	0.00	1.26	-0.76	569	H1L1V1	15 – 18
Ll1-20-20_T4	1	35.5	-0.20	1.70	-0.03	244	H1L1V1	52 – 71
Ll1+40+40_T4	1	14.4	0.40	4.18	0.07	170	H1L1V1	175 – 193
G2+20+20_T4	2	26.8	0.20	2.19	-0.36	247	L1V1	68 – 90
L4+00+00_T1	4	19.1	0.00	1.68	0.14	83	H1V1	86 – 93
J1+25+25_T4	1	75.7	0.25	4.68	0.49	854	H1V1	20 – 21
J1-75-75_T1	1	19.3	-0.75	0.81	-0.07	292	H1L1V1	69 – 79

Table 4.3: The details of the blind injections that were added to the NINJA-2 datasets prior to analysis. M denotes the total mass and q the mass ratio. χ denotes the spin on *each* black hole: in all 7 cases both black holes in a binary had the same spin. The RA and dec give the right ascension and declination of the signals, respectively. Dist. denotes the distance to the source. Detectors online lists the detectors for which data is present at the time of signal. Hybridization range gives the range of frequencies in which the signal is hybridized between the post-Newtonian and numerical components. Waveform label indicates which numerical waveform was used, as shown in Tables 4.1 and 4.2.

event is a signal or a noise artifact, affects the analysis process.

The 7 waveforms that were added to data sets were taken from NINJA-2 pN-NR submissions. The parameters of the blind injections were selected to cover a wide section of the parameter space. However, the physical parameter values of these injections was not meant to represent any physical distribution. Table 4.3 presents the values of the parameters used to construct each blind injection.

4.4 Binary Black hole search

The main goal of the NINJA-2 blind injection challenge was to assess the sensitivities of data analysis search pipelines to modelled signals from BBH systems using latest NR developments. This analysis used two search pipelines. Namely, the CBC ihope search pipeline [20] and the unmodelled burst pipeline *Coherent WaveBurst* (cWB). Similar to latest the LIGO Virgo science runs the ihope search was divided into two separate searches based on the total mass of the system. The lowmass ihope pipeline is designed to search for BBH systems with total mass from $1M_\odot$ to $25M_\odot$ while its highmass counterpart searches for systems with total mass from $25M_\odot$ to $100M_\odot$. The author was the lead analyst for highmass BBH search and some of the results shown in this chapter are taken from NINJA-2 blind injection analysis.

The ihope pipeline begins by matched-filtering the detector data with a dense bank of templates. These templates are effective-one-body inspiral-merger-ringdown model calibrated to numerical relativity waveforms described in Ref. [63]. It is important to note that these templates used are modeled GW signals from non-spinning compact binaries. The filtering stage of the pipeline produces a sequence of triggers, which are plausible events with a high signal-to-noise ratio (SNR). The coincidence algorithm of Ref. [21] is used to keep only those triggers that are coincident across the network of detectors, in order to reduce the false alarm rate. Knowledge of the instruments and its environment is used to further exclude events that are likely due to non-Gaussian noise transients, or glitches, as they are referred to in Ref. [6]. The time periods where the rate of glitches is elevated are

divided into three *Veto* categories. Veto-categories $1, 2$ and 3 contain time segments when the instrument is known, with respectively decreasing certainty, to cause glitches in the data. These vetoes are applied to exclude especially noisy chunks of time from the analysis, in a cumulative manner; e.g., Category-3 periods are vetoed only after vetoing Category-$1, 2$ times. Signal-based consistency measures further help distinguish real signals from background noise triggers for those that are not vetoed and pass the coincidence test. The χ^2 statistic proposed in Ref. [43] quantifies the disagreement in the frequency evolution of the GW trigger and the waveform template that accumulated the highest SNR for it, c.f. Eq. (4.14) of Ref. [43]. We weight the SNR with this statistic to obtain the *re-weighted* SNRs of all coincident triggers. The exact weighting depends on the mass range the search is focused on, c.f. Eqs.(17) and (18) of Ref. [20]. Higher values of re-weighted SNR indicate a higher likelihood of the trigger being a real signal, and it is used as the ranking statistic to evaluate the significance, or the false alarm rate (FAR), of all triggers.

4.5 Results

The data set used for the blind injection challenge was selected from LIGO S6 and Virgo VSR 2/3 data and recolored to match early advanced detector sensitivities as discussed in this chapter. Therefore, we applied the same vetoes that were used in Ref. [9, 7]. After category 1-3 vetoes were applied, the total analyzed time consisted of 0.6 days of coincident H1L1 data, 5.4 days of coincident L1V1 data, 6.5 days of coincident H1V1 data and 8.9 days of coincident H1L1V1 data.
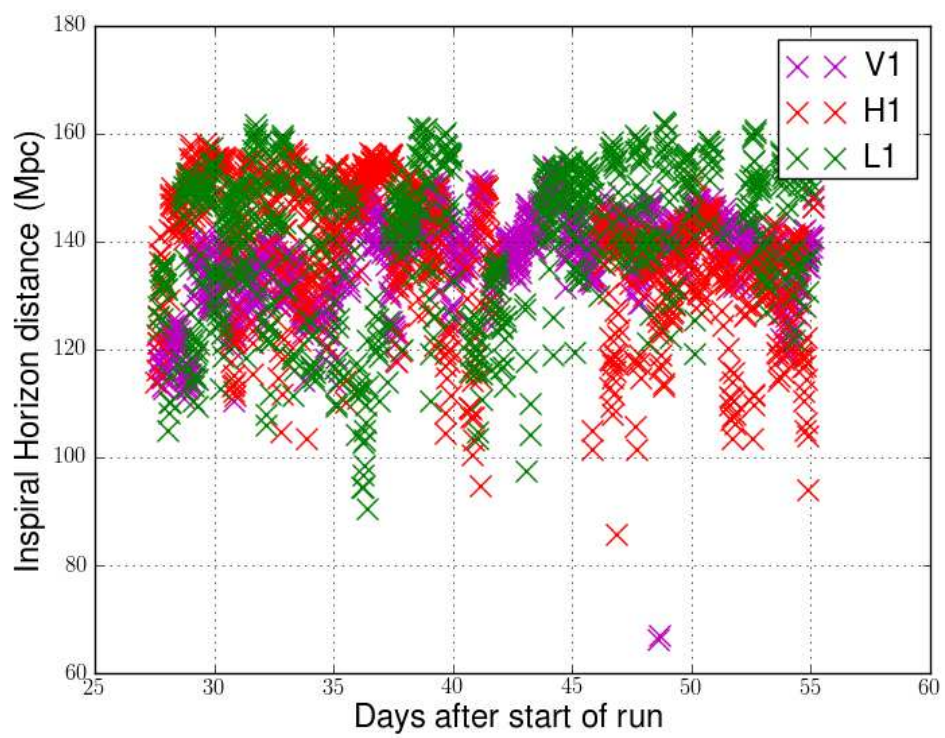
Figure 4.4: Inspiral horizon distance in Mpc for two LIGO detectors and the Virgo detector in NINJA-2 highmass search.

False alarm rates (FARs) were calculated in each bin using the time-shift method described in Ref. [20].

Initially we used 100 time shifts to identify candidate events. This means in addition to original analysis we conduct 100 more analyses by time shifting detector data by different time intervals. For each time shifted analysis we ensure the shifted time larger than the time travel time between different detectors. In this results all of the coincident events later associated with the blind injections were louder than all background in the 100 time shifts. These were also the only events to be louder than all background triggers. Using 100 time shifts we could only bound the FAR of the events to $\lesssim 10\,yr^{-1}$, which is not small enough to claim a detection. To improve our estimate, we performed as many $5\,$s time shifts as possible in the two calendar weeks surrounding each event. This is the same method that was used for the blind injection described in Ref. [9]. Using the FAR estimate from the extended background we estimated the false alarm probability as $1-\exp[-FT]$, where F is the FAR and T is the foreground analysis time. The false alarm probability is given in Table 4.4 for each candidate.

Four blind injections were recovered by the ihope highmass search. Two of them were found when all three detectors were taking data. Among them one event was a triple coincident event and the other one was a double coincident event. The remaining two event were also recovered as double coincident events in double coincident time.

Event one was found as an H1L1 event in triple coincident time. The individual detector SNRs for this event were 18.64 and 14.0 for H1 and L1, respectively. The most recent highmass search for LIGO and Virgo science data runs divided events

100

Event ID	$(FAR)^{-1}$ (yr)	ΔM (%)	Δq (%)	Analyzed Detectors	Found Detectors	Network SNR
1	≥ 6174	-20	380	H1L1V1	H1L1	16.34
2	≥ 10204	32	440	H1L1V1	H1L1V1	14.12
3	≥ 30612	-7	-30	L1V1	L1V1	14.94
4	≥ 36963	-9	220	H1V1	H1V1	15.32

Table 4.4: This table reports the results of ihope highmass search for NINJA-2 mock data challenge. ΔM and Δq are the percent difference in total mass and mass ratio, respectively, between the blind injections and the candidates reported by ihope. These values are calculated by finding *(Rec - Inj)/Inj*, where *Rec* is the recovered parameter and *Inj* is the injected parameter. The recovered parameters are calculated from the average value of the parameters recovered in each detector.

into two different bins based on their template durations. For this specific event template durations in H1 and L1 are 0.284 and 0.236 seconds. As described in Ref. [7] and earlier chapters, events with template duration larger than 0.2 s in all detectors are considered to be long duration events. Following the same criteria we consider this event to be a long duration event. The re-weighted SNRs for this events are 12.33 and 10.72. This event was found louder than all the background events in the long duration bin.

The second event was found as an H1L1V1 event in triple coincident time. Although there were three different events corresponding to the same event time (i.e., H1L1, H1L1V1 and L1V1), the triple coincident event was found as the most significant of them. The re-weighted network SNR of this event is 14.12. Despite
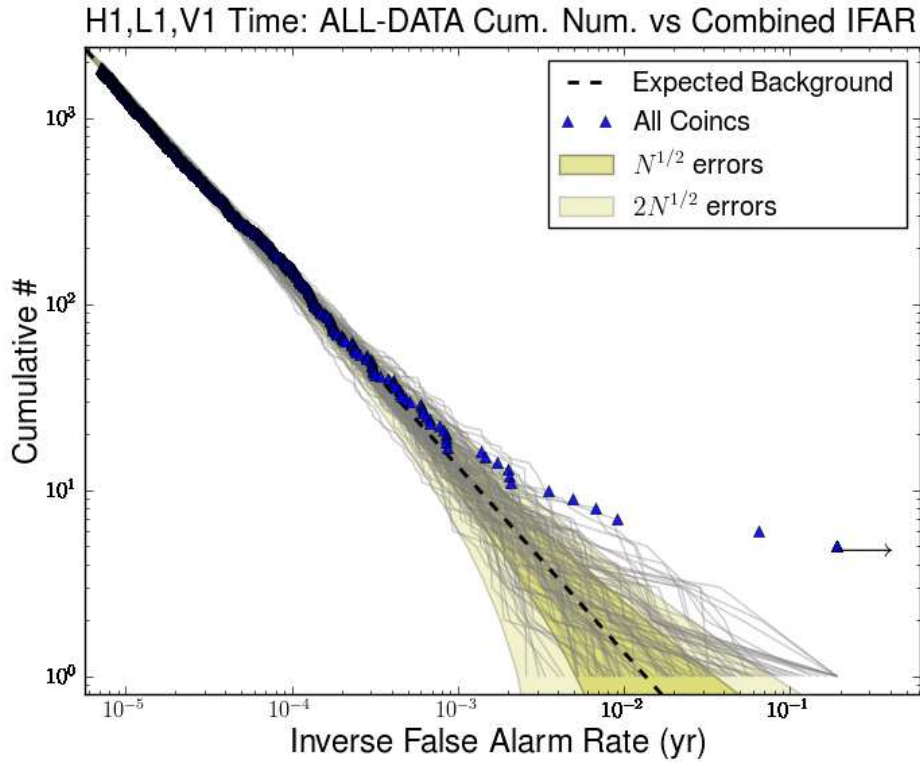
Figure 4.5: Combined Inverse False Alarm Rate(IFAR) plot for H1L1V1 coincident time after category 3 vetoes were applied. Events one and two in table 4.4 are the triggers above all the background events.

being a triple coincident event most contribution to its SNR arises from L1 and V1 detectors. Individual detector SNRs of H1, L1 and V1 are 6.57, 9.57 and 9.17, respectively. The extended background estimation computed in previous studies was only limited to double coincident events. Therefore, we considered this event as an L1V1 event for 5 s time-slide calculations. The same procedure was used for studying the NINJA-2 lowmass candidates [6].

The candidates of highmass search can belong to either long or short duration
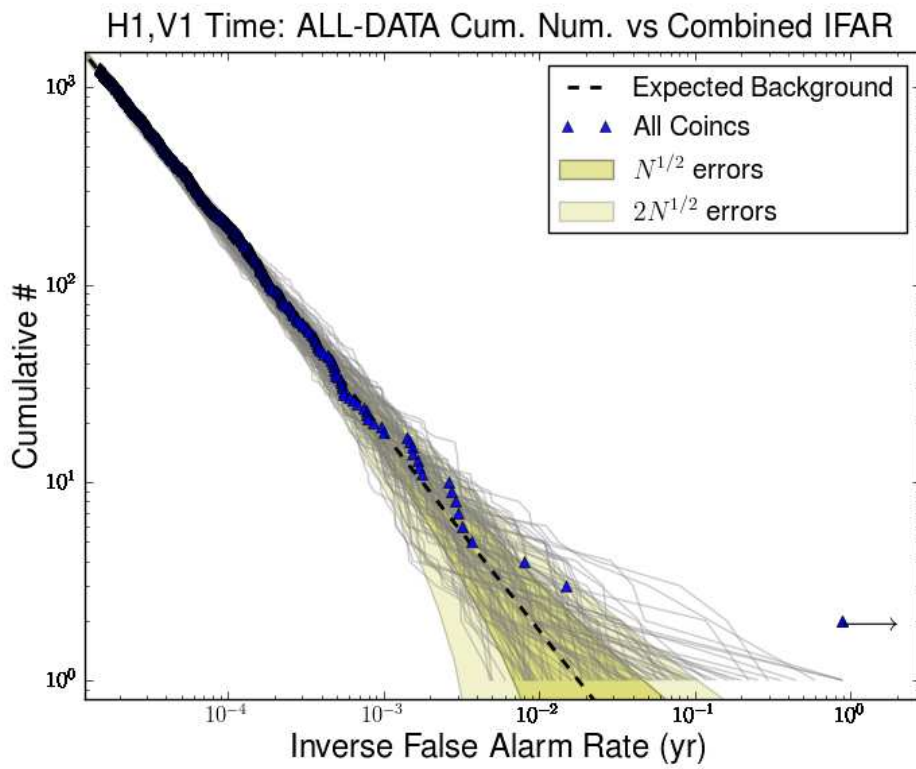
Figure 4.6: Combined IFAR plot for H1V1 coincident time before category 3 vetoes were applied. Event four in table 4.4 is the trigger above all the background events.
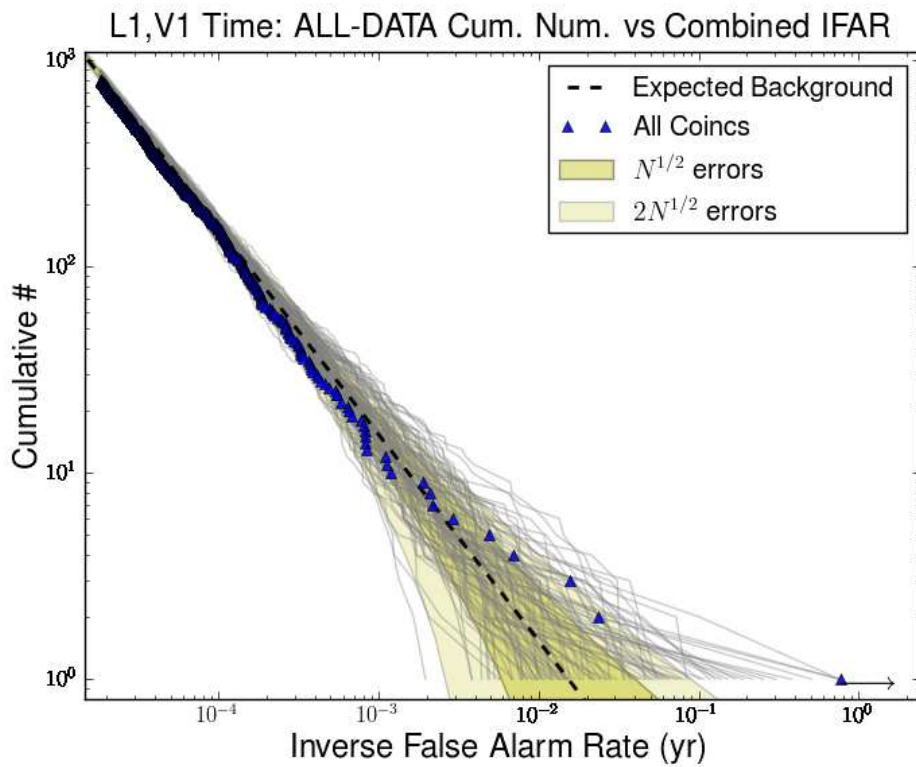
Figure 4.7: Combined IFAR plot for L1V1 coincident time after category 3 vetoes were applied. Event three in table 4.4 is the trigger above all the background events.

template bins depending on their template lengths. Therefore, there is no clear way to understand which candidate is the strongest if loudest candidates fall into two different bins. The third event is an L1V1 double coincident event in double coincident time. Similar to earlier events this is also found louder than all the background events. The re-weighted network SNR for this event is 15.94. The individual detector SNRs are 8.97 and 12.18 in L1 and V1 detectors, respectively. The total mass of the system found in L1 and V1 are $24.8 M_\odot$ and $25.7 M_\odot$, respectively. This suggests the possibility that this binary system has an actual mass that is lower than what is recovered in the highmass search owing to its template bank range.

The fourth event is the only event that did not survive category 3 veto level. Therefore significance of this event was calculated using triggers survived after category 2 vetoes. The re-weighted network SNR of this event is 16.03. According to template duration reported by ihope search, this event is also considered as a long duration event. Although the total mass of the system found in two different detectors are similar namely, ($72.5 M_\odot$ and $65.9 M_\odot$), the recovered values of individual component masses were very different in them.

4.6 Discussion

Table 4.4 also gives the percent differences in the total mass and mass ratio between the values reported by ihope and the values used to construct the blind injections. We see that the values reported by the ihope pipeline can vary substantially from the injected ones. This is not surprising since it is primarily a detection
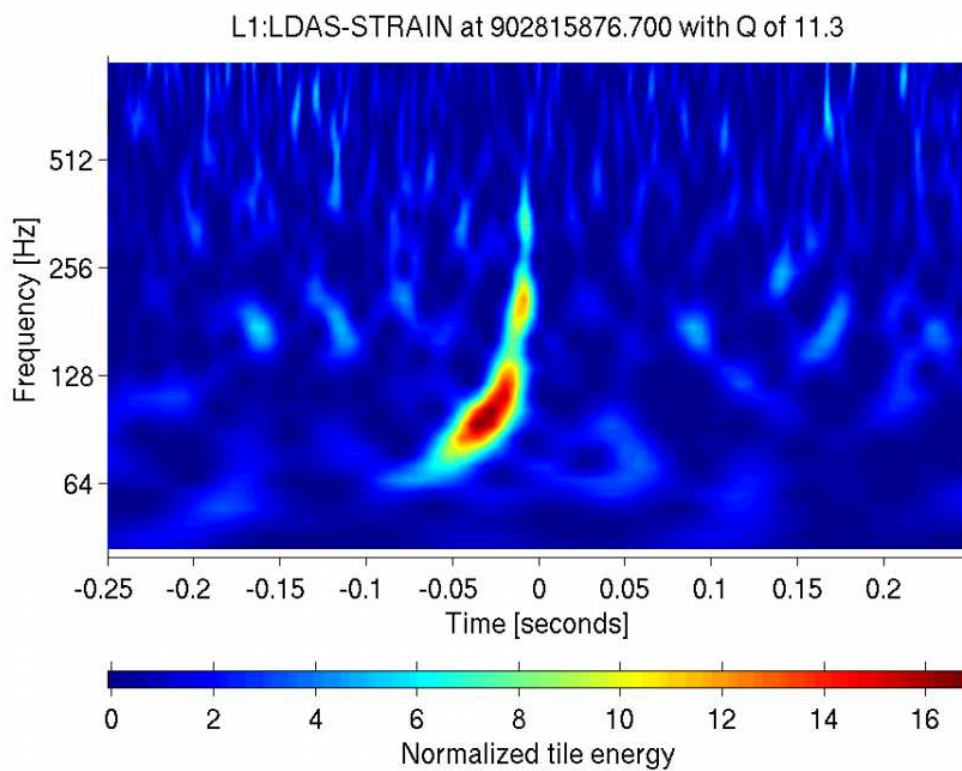
Figure 4.8: Omega scan for LIGO Livingston detector for the triple coincident event 2 in table 4.4. For this event L and V were the dominant detectors compared to LIGO Hanford.
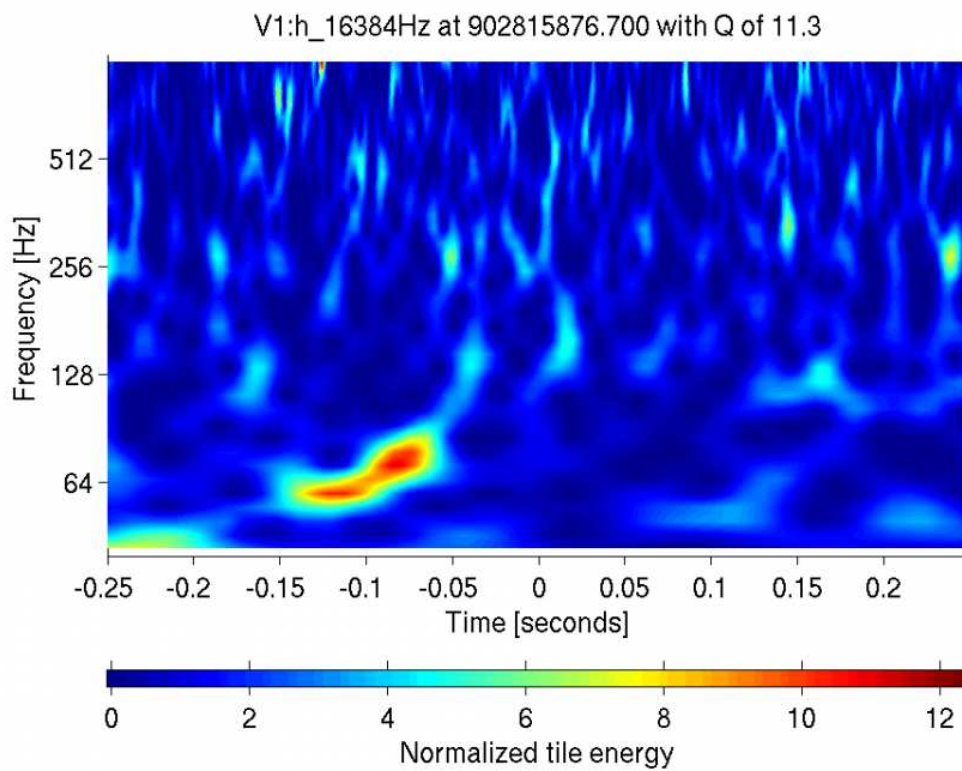
Figure 4.9: Omega scan for Virgo detector for the triple coincident event 2 in table 4.4. This event was louder in L1 and V1 detectors than in H1 detector. Therefore, for the extended time-shifted analyses we only used L1 and V1 triggers.

pipeline: many of the injections had spin, and one injection (Event 1) was outside of the mass range searched. We also see that the high-mass search deviates from the actual mass parameters more than the low-mass search. This, too, is expected since the template bank in the high-mass search is more sparsely populated. In general, templates are placed in the ihope so as to maximize detection probability across the parameter space while minimizing computational cost. The ihope therefore only provides a rough estimate of candidate parameters. For more precise estimates we use the parameter estimation techniques and results described in Ref. [6]. That reference also reports the results thus obtained.

The greatest concern for a detection pipeline like ihope is whether mismatch between templates and signals is small enough so as not to lose a substantial amount of re-weighted SNR. Remarkably, the templates used in this search were able to recover enough SNR of the blind injections to make them stand significantly above background.

Chapter 5

Results of recent LIGO, Virgo science data searches for Compact Binary Coalescences

5.1 Introduction

Chapters 2 and 3 of this thesis present studies of what we did with simulated GW signals in simulated Gaussian data to test our search pipelines and improve their detection probabilities. The main impetus behind these studies however is to ultimately prepare for searches in real detector data with non-stationary and non-Gaussian noise. This chapter presents a few such applications with real detector noise. The most recent science run of LIGO, namely, the sixth Science run (S6), started on 7 July 2009 and ended on 20 October 2010. During this time period Virgo also finished two Science runs, the first one from from 7 July 2009 to 11

January 2010 (VSR2), and the second one from 11 August 2010 to 20 October 2010 (VSR3). There were two all-sky, all-time searches conducted in the CBC sub group during these Science runs, namely, the CBC low mass search and the CBC high mass search. Both these searches employed the ihope data analysis pipeline to search for GW signals in LIGO/Virgo data with different features specific to each search. There was significant improvement of the data analysis software in between two LIGO Science runs S5 and S6. This chapter presents details of such improvements of the search pipeline, search techniques and results of the LIGO S6 and Virgo VSR2/3 low and highmass searches.

5.2 LIGO S6, Virgo VSR 2/3 search for lowmass Compact Binary Coalescences

5.2.1 Overview

The lowmass search is developed to detect GW signals emitted by compact binaries with total mass in the range from $2M_\odot$ to $25M_\odot$. Binary Neutron Stars (BNSs), Binary Black Holes (BBHs) and, Neutron Star-Black Hole (NS-BH) binaries are among the promising sources for this search. For such binary coalescences, the inspiral and merger phases of the system occur in the most sensitive band of LIGO and Virgo detectors (between 40 and 1000 Hz). Similar to earlier search for S5 data, *ihope* data analysis pipeline was employed to search for GW signals. However, compared to their S5 versions, the data analysis pipeline and techniques were modified to make the search more efficient in detectability and latency.

The main component of the ihope data analysis search pipeline is to matched-filter individual detector data against the bank of templates. For this search template wave-forms were generated at 3.5 post-Newtonian order in the frequency domain and placed across the mass range such that no more than 3% SNR was lost due to the discreteness of the bank. The analysis was carried only for non-spinning GW signals. The upper limit used for the total mass in the initial stages of the search was chosen to be $35 M_\odot$. However, subsequant studies indicated that waveforms of systems with total mass between $25 M_\odot$ and $35 M_\odot$ are more susceptible to non-stationary noise in the data. Therefore, the upper mass limit used in the later stages of the analysis was reduced to $25 M_\odot$.

Similar to the earlier version of lowmass ihope analysis, we required GW triggers to have greater than 5.5 matched-filter SNR in at least two detectors and consistent values for masses and arrival times across different detectors to claim that the triggers correspond to a GW candidate. However, changing the ranking statistic for the lowmass search in S6-VSR2/3 can be identified as the most significant change from its last edition. During LIGO S5 and Virgo VSR1/2 lowmass search, effective SNR was considered as the ranking statistic. To improve the detectability of GW signals, the new event ranking statistic re-weighted the SNR with the reduced chi-squared statistic χ_r^2 [41]. To avoid effective SNR becoming larger than SNR for $\chi_r^2 < 1$, the new ranking statistic, known as *new SNR*, was introduced.

$$\hat{\rho} = \begin{cases} \dfrac{\rho}{[(1 + (\chi_r^2)^3)/2]^{1/6}} & \text{for } \chi_r^2 > 1, \\[2ex] \rho & \text{for } \chi_r^2 \leq 1, \end{cases} \tag{5.1}$$

where, as before, ρ is the SNR of individual detectors.

The background rates of coincident GW events were estimated by performing time-shifted analysis to create non-physical events. For this specific search there were 100 time-shifted analyses performed. All the background and foreground events were sorted in to three different bins depending on their chirp mass $\mathcal{M} \equiv (m_1 m_2)^{3/5}(m_1 + m_2)^{-1/5}$ values. In the following step, the search algorithm compares the value of the ranking statistic of every GW candidate with that of every background event to assign FAR values to every candidate. This was computed separately for each chirp mass bin. Eventually all the FAR values for the different bins are combined to obtain the combined FAR of each event [41]. This value is considered as the detection statistic.

5.2.2   Search Results

Based on Science run durations and hardware upgrades LIGO S6 and Virgo VSR 2/3 low mass and high mass analyses were broken in to 4 epochs. These are S6A from 7 July 2009 to 1 September 2009, S6B from 24 September 2009 to 11 January 2010, S6C from 6 February 2010to 25 June 2010, and S6D from 26 June 2010 to 20 October 2010 [41]. Coincident times of network of detectors with LIGO and Virgo are categorized as H1L1, H1L1V1, H1V1 and L1V1. Here H1, L1 and V1 represent LIGO Hanford, LIGO Livingston and Virgo detectors, respectively
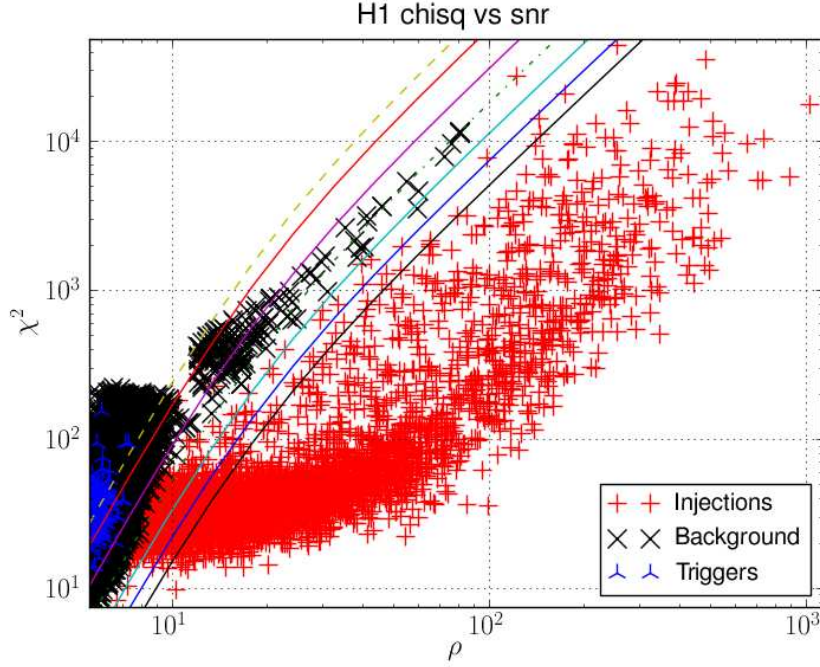
Figure 5.1: Distribution of χ^2 values of simulated signal injection and background events as a function of SNR. Data was taken from a sample of S6 lowmass search.

and H1L1 denotes times when H1 ans L1 have Science run data in coincidence. Total live times by coincident type are given in Ref. [41]. It is 70.2 days for H1L1, 37.4 days for H1L1V1, 39.1 days for H1V1 and 27.7 days for L1V1. Owing to the fact that Virgo was not operating during the S6C epoch, the live times of coincident types involving Virgo are less compared to those involving LIGO detectors.

Search results reveal no GW candidates observed in data. Indeed, the strength of the loudest events was consistent with that of the background events, obtained from time-shifted analysis [20]. The most significant event was an L1V1 coincidence in L1V1 time with combined FAR $1.2yr^{-1}$. The second and third loudest
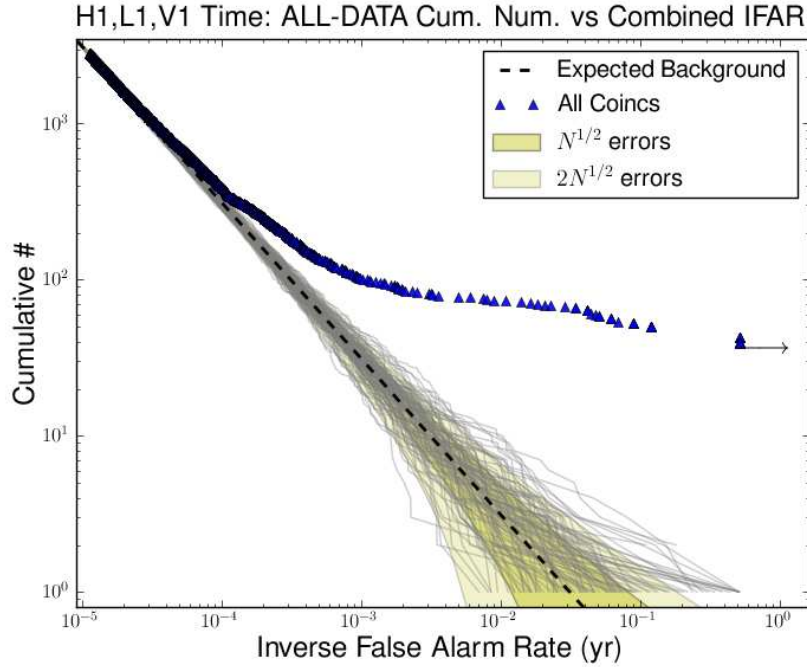
Figure 5.2: This plot was taken from the S6D epoch of the low-mass analysis. FAR was calculated for every candidate to understand their significance. Most significant events are the ones with the lowest FARs for a given search. This figure shows the inverse of FAR or IFAR of candidates before applying the CAT 3 veto, which removes the hardware injections from the list of candidates.

events had combined FAR of $2.2yr^{-1}$ and $5.6yr^{-1}$ respectively. Although no GW candidates were detected, observations from the search were used to set upper limits on coalescence rates of BNS, BBH, and NSBH systems.

The author performed the initial analysis and detector characterization of data from multiple fortnights of the chunk 2 period of the S6D epoch. Some of the figures here show results from those analyses (Fig. 5.2 and Fig. 5.4). No GW candidates were observed in the data.

114
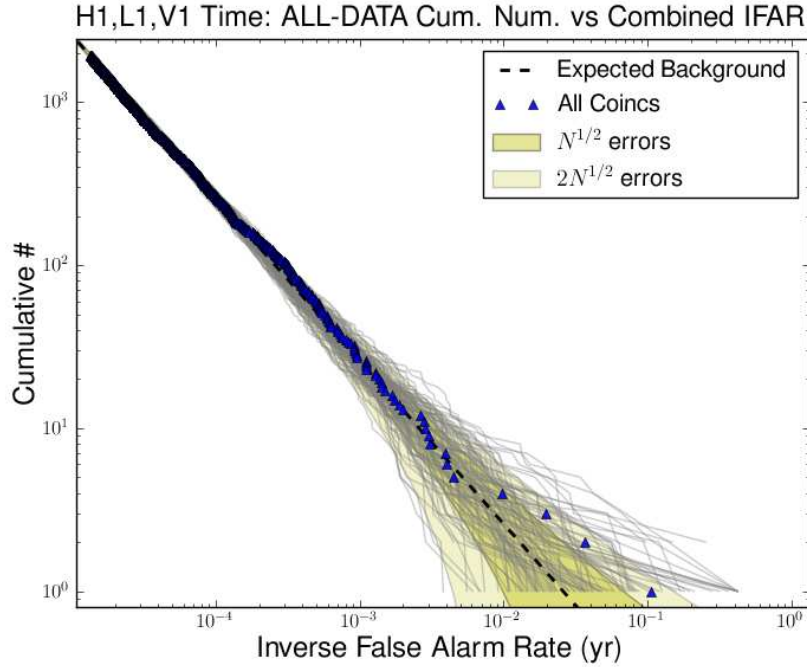
Figure 5.3: The same triggers as 5.2 with CAT 3 veto applied. Once CAT 3 is applied all triggers due to hardware injections will be removed from the figure. All Coincs denotes all the coincident events for a given coincident time (in this case H1L1V1).

Moreover, the search result was consistent with background estimation performed with time-shifted data.

5.2.3 Blind Injection Recovery

A simulated CBC signal injection was injected into the data of the LIGO and Virgo detectors by hardware actuation of their end test masses during S6D/VSR3 without the search groups' knowledge.

System	BNS	NSBH	BBH
Component masses ($M_\odot$)	1.35 / 1.35	1.35 / 5.0	5.0 / 5.0
D_{horizon} (Mpc)	40	80	90
Non-spinning upper limit ($\mathrm{Mpc}^{-3}\mathrm{yr}^{-1}$)	1.3×10^{-4}	3.1×10^{-5}	6.4×10^{-6}
Spinning upper limit ($\mathrm{Mpc}^{-3}\mathrm{yr}^{-1}$)	$\cdots$	3.6×10^{-5}	7.4×10^{-6}

Table 5.1: Summary of the upper limits calculation published as a part of S6, VSR 2/3 lowmass search results Ref. [9]. Table shows rate upper limits of BNS, BBH and NSBH coalescences, assuming canonical mass distributions. D_{horizon} is the horizon distance averaged over the time of the search [9]. The sensitive distance averaged over all sky locations and binary orientations is $D_{\mathrm{avg}} \simeq D_{\mathrm{horizon}}/2.26$ [10, 11]. The first set of upper limits are those obtained for binaries with non-spinning components. The second set of upper limits are produced using black holes with a spin uniformly distributed between zero and the maximal value of Gm^2/c. A spinning BNS search was not done.
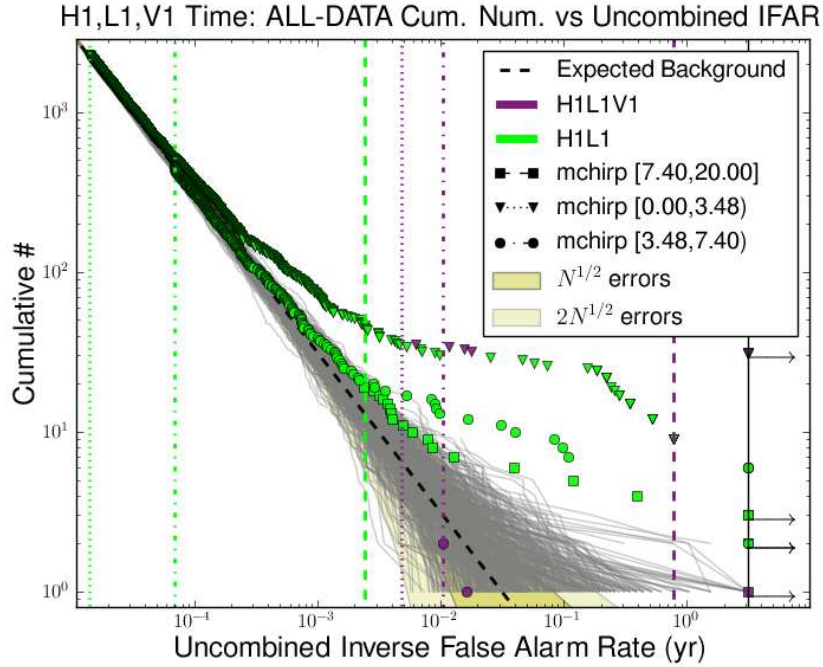
Figure 5.4: Uncombined FAR values for the same data shown in Fig. 5.2. As explained in the search overview lowmass search divides events in three bins based on their chirp mass (mchirp in legend) values. Note that this figure shows uncombined FAR values with hardware injections.

The idea behind this blind-injection challenge was to test the data analysis groups' abilities to detect signals and to exercise the LIGO and Virgo Collaborations' candidate vetting procedures in the event that a real GW candidate is detected. In this case, the signal was detected, without the knowledge of this blind injection. We treated this event as a real GW signal and completed the required analysis before the collaboration reveal the list of such injected signals.
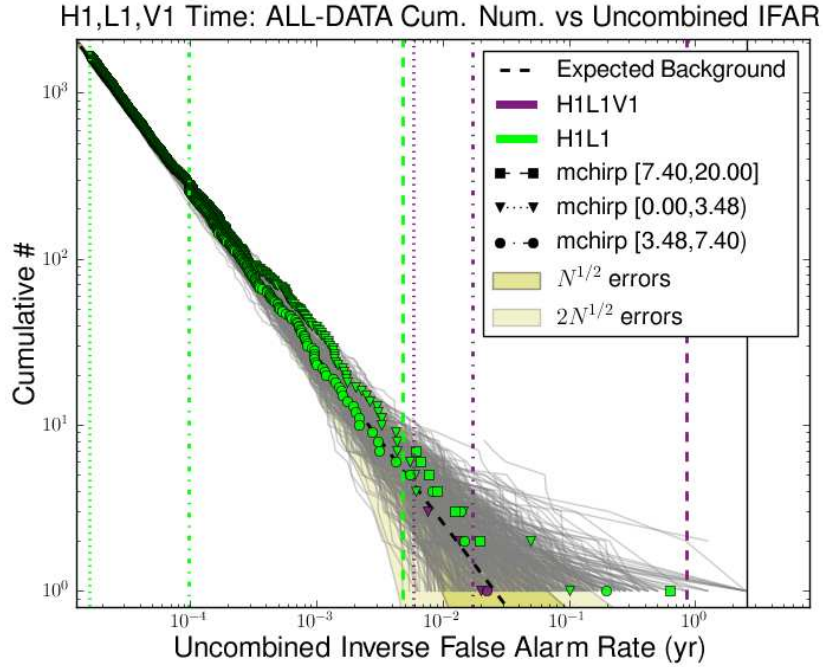
Figure 5.5: Uncombined FAR values for the same data shown in 5.3. As explained in the search overview lowmass search divides events in three bins based on their chirp mass values. Note that this figure shows uncombined FAR values without hardware injections.

The search pipeline described above (lowmass ihope) identified a GW candidate corresponding to the blind injection occurring on September 16, 2010, at 06:42:23 UTC, (GPS time 968654558.0 seconds) with combined new-SNR 12.5 in coincidence between the two LIGO detectors. The individual matched-filter SNR obtained for this event was 15 in H1 with total mass $4.7 M_\odot$ and 10 in L1 with total mass $4.4 M_\odot$. This difference in SNRs was consistent with typical differences in antenna response factors for these differently oriented detectors [9]. Although

Virgo was also operating at the time of the event, its smaller sensitivity, by a factor of approximately 4, compared to the LIGO detectors, caused the Virgo trigger to be below the SNR threshold and not pass the matched filtering step. As a double-coincident event, it was louder than all the background events obtained by the standard time-shifted analysis. However, with only standard 100 time shifts, we could only bound the FAR to less than 1 in 23 years, even after folding in all data from the entire analysis [9]. To seek a higher significance we performed all possible multiples of 5 sec time-shifts on four calender months of data around the event. With the extended background estimation we found five events that had a value of detection statistic that was equal or larger than that of the original candidate. However, these five events were coincidences of signal candidates in H1 and noise events in L1. Background estimation with candidate removed found no events louder than the original candidate. After considering all possible mass bins and possible coincidences, and taking trials factors into account [41], FAR for the event was found to be 1 in 7000 yr [41, 9]. See Fig. 3 of Ref. [9] for more information about background estimation of the blind injection recovery.

Estimating background of a GW search in the presence of one or multiple signals is a very challenging problem. In this exercise it was relatively easy since the event was a double-coincident event. For a triple coincident event this procedure can be computationally very expensive. In chapter 4 we presented results from NINJA-2 blind injection analysis. Similar to the blind injection recovery explained in the above paragraph, in NINJA-2 we recovered multiple blind injections in our analysis [6]. As expected, the estimated background for these candidates was not significant enough to claim a detection. Therefore, we employed the same

techniques described above to estimate their background. However, there were some differences: Namely, instead of event we had to deal with multiple events and one of them was triple-coincident event. Not having an algorithm to estimate background for a triple-coincident event led us to treat the event as double coincident, by choosing two dominant detectors out of the three that participated in contributing the event.

Results presented in Refs. [41, 9] were taken from the standard ihope pipeline. We also employed the blind hierarchical coherent pipeline to learn more about the blind injection. The main motivation for running the coherent pipeline was to confirm the findings of the standard ihope pipeline and add Virgo's trigger to make the event a triple-coincident event. Chapter 3 describes how the blind hierarchical coherent search pipeline combines all available detector data streams to extract as much information as possible. The coherent pipeline recovered blind injection with a weighted coherent SNR [8] of 17.54. Individual component masses found by the coherent search were $5.64 M_\odot$ and $4.96 M_\odot$. Although the coherent search was able to convert ihope's double-coincident event to a triple-coincident one in H1L1V1 time, Virgo's contribution was relatively weak. Therefore, the significance of the GW event assessed by the coherent search was only slightly better compared to the ihope results.

Figures 5.6 and 5.7 show the individual detector SNR time series and coherent SNR time series around the event time. Figure 5.7 reveals Virgo's signal is very weak compared to other detectors'. Additionally, it is clear that the two peaks of H1 and L1 time series are occurring at different times due to the time the GW takes to travel across the distance between the detectors. However, peak of the coherent
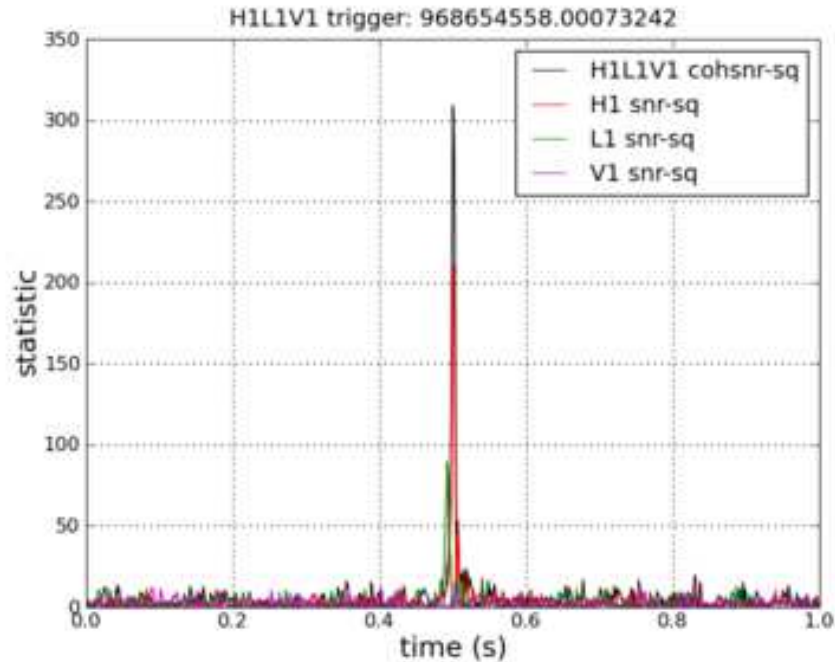
Figure 5.6: The SNR-squared time series computed on data from H1,L1 and V1 detectors around the time of the blind injection. This figure also shows the coherently combined data stream.

SNR time series is consistent with the peak of the H1 SNR time series as the latter had the strongest signal among all the detectors. As explained in chapter 2 the coherent pipeline is capable of computing the null-stream for a GW event. In this case we calculated it and compared it to the weakest detector SNR time series. The null-stream combines individual detector data in such a way that this combination will cancel a GW signal present in the data. Therefore, for real signals we will see a very small null-stream but for noise artifacts may find a relatively large null-stream. Figure 5.8 confirms that the null-stream of this event is very small and, therefore, it is a GW event. Comparison with the weakest detector SNR time series
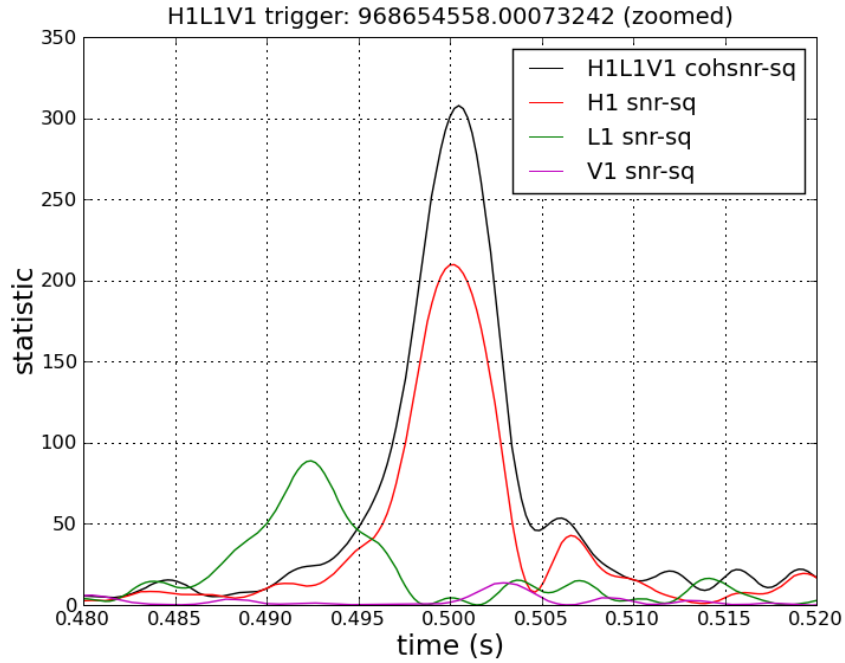
Figure 5.7: Zoomed version of Fig. 5.6 for all the individual detectors and coherent SNR-squared time series.

shows that at the time of the event the null-stream has a minimum while the SNR time series has a maximum.

Figures 5.9 and 5.10 present some scatter plots from two weeks of data that had the blind injection. Figure 5.10 is the zoomed version of Fig. 5.9. In these plots the y-axis represent χ^2 weighted coherent SNR (see Eqn. 2.39) and x-axis represents a detection statistic used for earlier searches, namely, the effective SNR. The red pluses in the figure denote foreground triggers and the black crosses represent background events. Since coherent searches do not give any extra information for searches with two detector with different orientations, double-coincident triggers have same the detection statistic for both coherent and coincident analyses.
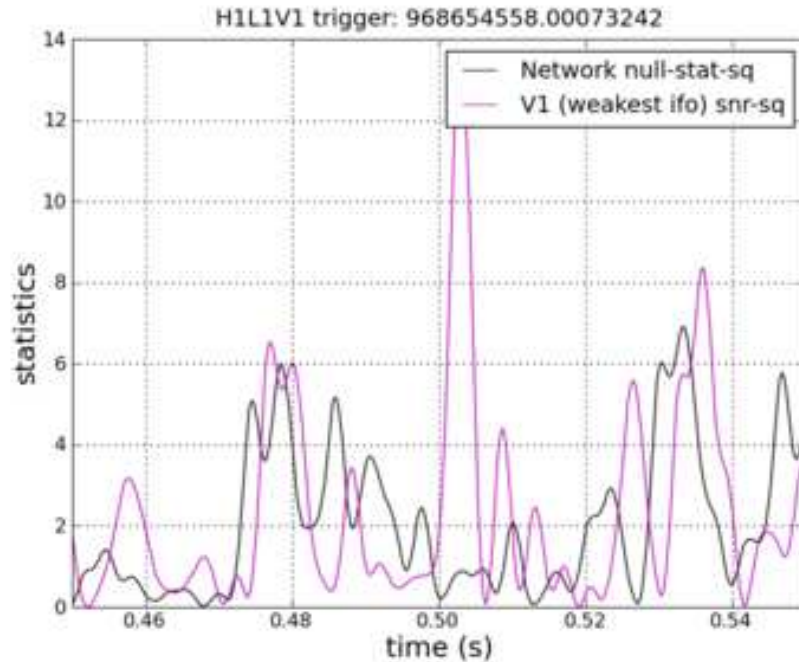
Figure 5.8: Comparison of the multi-detector null-stream-squared time series to the SNR-squared time series data of the weakest detector. In this case, Virgo had the weakest signal among all three detectors.

Therefore , the diagonal of both figures represent double coincident events. The loudest foreground event in both figure indeed is the blind injection recovered by the pipeline. In Fig. 5.10 it is clear that this events is slightly above the diagonal. Although the original ihope search found the blind injection as a double-coincident event, the coherent search converted it to a triple-coincident event with the contribution of the third detector, which is Virgo in this case. However, the signal in Virgo is too weak to give a significant contribution.

5.3 Search for Binary Black Holes in 2009-2010 LIGO, Virgo data

5.3.1 Overview

Similar to the low mass search presented in the previous section, the LIGO-Virgo collaboration also searched for GW signals from BBHs in LIGO S6 and Virgo VSR 2/3 Science data. Due to the nature of the search this is also known as high-mass search as it looks for GW signals from relatively higher mass binary compact objects. Most promising sources for such GW signals are BBHs. As discussed in earlier chapters, recent development in numerical relativity allows for GW signal modeling with more accurate, full Inspiral-Merger-Ringdown (IMR) waveforms. The highmass search in LIGO S6 and Virgo VSR 2/3 data shares some common search strategies with its lowmass counterpart.

When we search for GW signals in detector data, it is important to simulate some known waveforms and inject in to detector noise to analyse the performance of the data analysis pipeline in recovering them. Also it helps to compute upper limits for the source populations in case we fail to detect any GW signals. In this search we used two recently developed IMR waveform families. These families are know as EOBNRv2 (second version of Effective One Body-Numerical Relativity) and IMRPhenomB [114, 115]. The main difference of EOBNRv2 waveforms compared to the EOBNR waveforms used for Gauusian studies presented in chapter 3 is that type of numerical relativity waveforms used to calibrate two different families of waveforms. However, banks of templates for matched-filtering were

generated using EOBNRv1 family. The total mass in that bank ranges from $25M_\odot$ to $100M_\odot$, with individual component masses ranging from $1M_\odot$ to $99M_\odot$.

One notable change in this search is the reduced low frequency cutoff of Virgo. This was implemented due to improved low-frequency sensitivity of Virgo. It was reduced to 30 Hz compared to 40 Hz for LIGO. The background estimation procedure is exactly similar in this search to its low mass counterpart. To obtain background events 100 time-shifted analyses were performed by shifting L1 and V1 triggers relative to H1 triggers by multiples of 5 and 10 seconds, respectively.

5.3.2   Ranking Statistic

A ranking statistic helps to quantify the significance of GW and background events found by the matched-filtering algorithm. We optimize the ranking statistic so that it separates GW events from background events and improves the efficiency of the search. This is where simulated signal injections become useful. From the time of previous versions of highmass searches it is well known that signal-based vetoes such as the χ^2 test will not perform effectively for highmass signals. The higher the mass of the binary system the shorter the GW signal from its coalescence. For short signals with less number of cycles the χ^2 test can not discriminate them from noise artifacts well.

In the S6, VSR 2/3 the highmass data analysis team came up with a strategy to separate GW events found by *ihope* pipeline into two different bins based on the template duration of the events. Detailed studies showed that the template durations of both foreground and background triggers vary from 0.05 to several seconds.

125

Template with short durations are occurring from higher mass systems while low mass systems have relatively longer templates. Moreover, performance of χ^2 is worse for events with template duration shorter than 0.2 seconds. This was the main motivation behind binning triggers based on their template durations. The bin with long duration events contains all participating triggers from H1 or L1 (or V1, in VSR3 data) with template durations above $0.2s$. If at least one trigger from H1 or L1 (or V1, in VSR3) had a template duration below 0.2 seconds, such events were classified as short duration events. Due to two different distributions of background events, different choice of ranking statistic were introduced as below. For long duration events,

$$
\hat{\rho} = \begin{cases} \dfrac{\rho}{[(1 + (\chi_r^2)^3)/2]^{1/6}} & \text{for } \chi_r^2 > 1, \\ \rho & \text{for } \chi_r^2 \leq 1, \end{cases}
$$
(5.2)

was used as the ranking statistic and for short duration events. Above, χ_r^2 is reduced χ^2 [7].

$$
\rho_{\text{eff}} = \frac{\rho}{[\chi_r^2(1 + \rho^2/50)]^{1/4}}.
$$
(5.3)

was used as the ranking statistic.

The multi-detector detection statistic, *combined SNR ρ_c*, is then the square-root of the quadrature sum of single-detector SNRs, of the coincident triggers contributing to an event.

5.3.3 Search Results

The GW strain data recorded by detectors contains large number of various transient noise events that can have features very similar to GW signals. Data quality studies were conducted to recognize such events and remove potentially corrupted parts of data. After careful investigation of data quality studies, we removed (" i.e., vetoed") portions of GW detector data that were corrupted. Approximately $0.47yr$ of coincident data remained after applying all the vetoes. Additionally 10% of data, known as "playground", was preserved for tuning studies. All the vetoes were applied and after excluding playground, there was $0.09yr$ of H1L1V1 coincident time, $0.17yr$ of H1L1 time, $0.10yr$ of H1V1 time and $0.07yr$ of L1V1 time contributing to total analysis time of $0.42yr$.

There were no significant events above the background to claim a detection. All the loudest events were consistent with the background. The event found at GPS time 939789782 can be considered as the most significant event for the overall search. This is a H1V1 coincident event in H1V1 time with lowest estimated FAR of $0.41yr^{-1}$. The next few loudest events had estimated FAR of a few per year and hence were consistent with the background. The null result of the search led us to calculate observational upper limits for the event rates. Section V of Ref. [7] presents details about upper limit calculations and the results, which are also compared with the finding of the S5 highmass search.

5.4 Discussion

Although there were no GW candidates detected in the lowmass search its upper limit has been improved by a factor 1.4 compared to the S5 lowmass search. Additionally, this exercise was useful in identifying some of the factors that can be improved in time for the ADE searches. Clearly, background estimation will require a lot of attention due to its complex nature. Here we applied different methods to estimate the background accurately. In many occasions we did not get enough background events to assign a meaningful FAR value to a loud candidate.

For highmass searches there are a few issues that need to be addressed before moving to ADE searches. One main piece of work is to develop the template placement metric used by the ihope pipeline. The current version of the metric uses only the inspiral portion of the waveform to calculate the metric. Implementing a metric that is based on IMR waveforms will improve the detection efficiency of future searches. Another way to improve the detection efficiency is to use spinning waveforms for our templates. That, however, is computationally very expensive. Moreover, it can incur a worse background. For reasons like this, less ambitious template banks that use spin-aligned waveforms are being experimented with currently [116, 117].
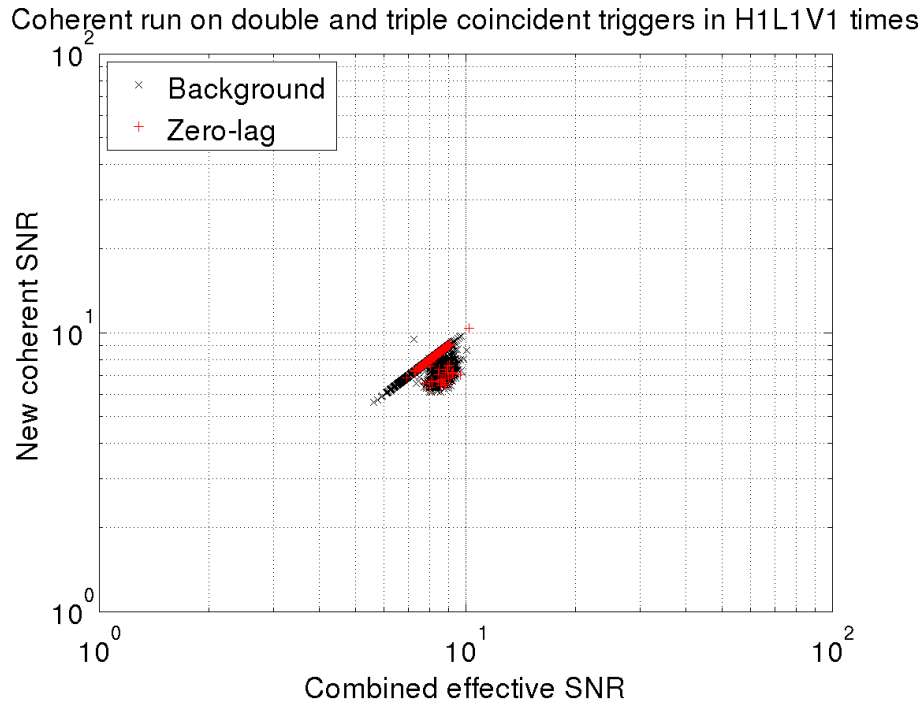
Figure 5.9: Scatter plot of foreground and background triggers for two weeks of data that had the blind injection. The plot was produced with the results of the coherent pipeline. The x-axis represents a detection statistic used for earlier searches, namely, effective SNR. The effective SNR is given in Eqn. 5.3. The y-axis represent χ^2 weighted coherent SNR. The red pluses and the black crosses represent foreground and background triggers respectively. These triggers can be triple coincident or double coincident events. For double coincident triggers coherent SNR and effective SNR are the same in this plot. Therefore, triggers along the diagonal are the double coincident triggers found by the pipeline for these two weeks of data. The loudest foreground event is the blind injection.

129
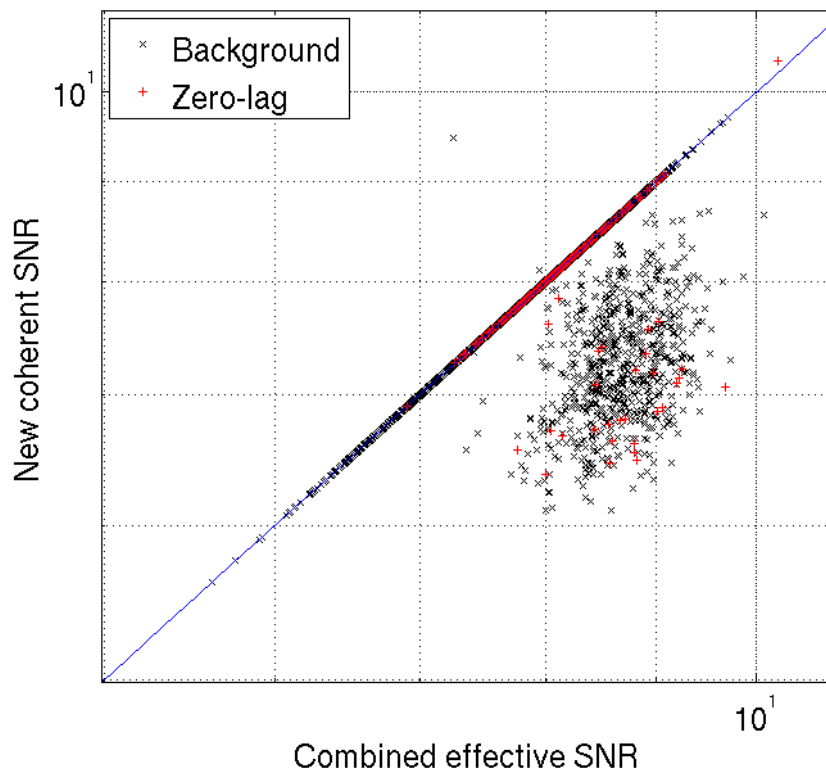
Figure 5.10: Zoomed version of Fig. 5.9. All the triggers on diagonal are double coincident events. No clear separation of foreground and background triggers suggests all the foreground triggers are consistent with the background of the search. Only exception is the blind injection event.

Chapter 6

Future developments

In earlier chapters we gave details of GW searches for CBC sources. Following the discussion of data analysis pipelines, we presented results from those studies. In this chapter we briefly summarize how some of our findings can benefit future searches. Powerful insights from past searches always help the next step of the process to improve the quality of the data analysis efforts towards the first direct detection of a GW signal.

The version of the ihope pipeline that was used for the studies presented in previous chapters contains two matched filtering steps. Therefore, this version of the pipeline is also known as two-stage ihope pipeline. The main idea behind running two steps of the matched filtering process is to save computational power by doing the more expensive signal-based veto calculation only for a selected set of GW triggers found by the first stage of matched the filtering process. However, with currently available computational resources it is possible to combine both these steps of matched filtering into a single step, thereby, saving time required

for data analysis. Different data analysis groups have already started experimenting with the single stage ihope pipeline [41]. In addition to saving time, a single stage pipeline makes it easier to track GW triggers for follow-up analysis. While the current version of the ihope pipeline is not an on-line search, for ADE searches it will be critical to detect GWs with low latency. The version of the ihope pipeline employed for the most recent science run data analysis determines GW trigger coincidences based on an ellipsoidal parameter consistency check algorithm presented in Ref. [21]. Some of the current efforts try to recover GW signals based on exact match methods, in which GW triggers that are coincident in different detectors are found by the same template. One disadvantage of the ellipsoidal method is that it requires higher dimensional ellipsoids for spinning GW searches. In ADE searches due to improvement of the sensitivity of the low frequency region of the detector band, GW signals will spend several minutes in sensitive region compared to seconds in initial ground-based detectors. This demands capability of data analysis algorithms to handle significantly long waveforms.

The blind hierarchical all-sky all-time coherent analysis demonstrated expected results for the searches presented in this thesis. However, there is still room for improvements for future searches, two of the main ones (a) removing the coincident step and (b) finding a computationally efficient method for assessing the background. With these improvements ADE searches with three or more participating detectors would gain in detection efficiency. By performing the analyses presented in this thesis we identified limitations of blind hierarchical coherent searches and how to improve them for an implementation of fully coherent searches. One major drawback of current version of the coherent pipelines comes from its own struc-

ture. Running in a hierarchical manner following the traditional ihope pipeline does not create an opportunity to recover new GW signals. Owing to the pipeline's current setup, the coherent stage analyses only those GW triggers that are selected by the ihope search as candidates. Therefore, the only way it performs better compared to a coincident search is by reducing the strength of the background triggers compared to that of GW signals. A fully coherent search will not have this limitation. In chapter 3 with pN-NR simulations we compute how many signals were not recovered owing to single detector threshold criterion in the matched filtering step. It is clear that a GW signal with individual detector SNRs of 6.0, 5.3 and 5.4, the hierarchical search pipeline will not utilize triggers from two of the three detectors due to their lower SNR compared to the threshold of 5.5. However, a fully coherent search will recover such a signal, with a relatively large network SNR.

In recent analyses the template bank placement metric of CBC searches was calculated by using only the inspiral portion of the waveform. To obtain more accurate results we can calculate a new metric based on the full inspiral-merger-ringdown waveforms. Since the blind hierarchical coherent search runs as a part of ihope pipeline it also uses the same template placement metric. Reference [28] presents a new metric calculated based on the multi-detector F-statistics for coherent searches. Employing such a metric for future searches will increase detection efficiencies of GW searches. In ihope searches we use different template banks in every detector. Therefore, triggers that survive till the start of the coherent analysis can possibly have three different mass pairs in the three different detectors for a given GW coincidence. Currently we use the mass pair that has highest single-

detector SNR in all participating detectors. However, theoretically, for coherent searches, it is possible to compute a network signal template using the metric presented in Ref. [28] to achive a better sensitivity.

Most of the ground-based GW detectors will start collecting data as advanced detectors in a few years. At least two LIGO detectors will start their initial Science runs in 2015. It is important to notice that with two detectors in different sites coherent SNR is the same as the combined SNR. Therefore, the time when at least three detectors start collecting data will be the perfect time to introduce fully coherent searches of the all-sky, all-time type.

Another advantage of coherent searches is that they provide for signal consistency tests such as the null-stream. In a multi-detector search it is possible to combine individual detector data streams in such way that the combination will have the GW signal absent. In earlier chapters we described how to compute null-stream in a multi-detector search and presented results from NINJA-2 simulations in Gaussian and stationary data, which prove that we can use it effectively as a multi-detector consistency test [118]. Reference [24] demonstrates how to use null-stream in targeted coherent searches. For all-sky all-time (blind) searches we have to verify the performance improvement in real detector data before it can be effectively used in future searches. Joint searches for GWs with EM telescopes will play an important role in ADE searches. To understand the nature of events such as GRBs, joint searches can reveal more information compared to just GW detections alone. Data analysis pipelines employed for detector characterization in the past, such as the daily ihope pipeline [38], can do relatively quicker analysis to search for odd behaviors of detectors. If effectively used, the null-stream can be

a very handy tool for detector characterization in the ADE.

The coming few years will be a very exciting time for GW community. A few ground-based interferometers will start collecting data as advanced detectors. With improved sensitivity advanced detectors will be able to make the first direct detection of GWs. Those observations will allow scientist to usher in the era of gravitational-wave astronomy in the near future.

Bibliography

[1] Paul A. Lynn. *An introduction to the analysis and processing of signals*. Hemisphere Publishing Corporation, 79 Madison Avenue, NY, USA, 1989.

[2] Carl W. Helstrom. *Elements of signal detection and estimation*. Prentice-Hall, Inc., Upper Saddle River, NJ, USA, 1995.

[3] Advanced LIGO anticipated sensitivity curves. `https://dcc.ligo.org/cgi-bin/DocDB/ShowDocument?docid=2974`.

[4] Advanced Virgo Baseline Design. `https://pub3.ego-gw.it/itf/tds/file.php?callFile=VIR-0027A-09.pdf`.

[5] Ilya Mandel, Duncan A. Brown, Jonathan R. Gair, and M. Coleman Miller. Rates and Characteristics of Intermediate-Mass-Ratio Inspirals Detectable by Advanced LIGO. *Astrophys.J.*, 681:1431–1447, 2008.

[6] The LIGO Scientific Collaboration The NINJA-2 Collaboration and the Virgo Scientific Collaboration. The NINJA-2 project: Detecting and characterizing gravitational wave signals from numerical binary black hole simulations, LIGO-P1300199. *In preparation*, 2013.

[7] J. Aasi et al. Search for Gravitational Waves from Binary Black Hole Inspiral, Merger and Ringdown in LIGO-Virgo Data from 2009-2010. *Phys. Rev.*, D87:022002, 2013.

[8] S. Bose, T. Dayanga, S. Ghosh, and D. Talukder. A blind hierarchical coherent search for gravitational-wave signals from coalescing compact binaries in a network of interferometric detectors. *Class. Quant. Grav.*, 28:134009, 2011.

[9] J. Abadie et al. Search for Gravitational Waves from Low Mass Compact Binary Coalescence in LIGO's Sixth Science Run and Virgo's Science Runs 2 and 3. *Phys. Rev.*, D85:082002, 2012.

[10] D.F. Chernoff and L.S. Finn. Gravitational radiation, inspiraling binaries, and cosmology. *Astrophys. J. Lett.*, 411:L5–L8, 1993.

[11] S. Ghosh and S. Bose. Toward finding gravitational-wave signals from progenitors of short hard gamma-ray bursts and orphaned afterglows. *arXiv*, 1308.6081, 2013.

[12] A. Einstein. Approximative Integration of the Field Equations of Gravitation. *Preuss. Akad. Wiss. Berlin*, page 688, 1916.

[13] A. Einstein. Über Gravitationswellen. *Preuss. Akad. Wiss. Berlin*, pages 154–167, 1918.

[14] R. A. Hulse and J. H. Taylor. Discovery of a pulsar in a binary system. *Astrophys. J.*, 195:L51 –L53, 1975.

[15] J. Aasi et al. A search for long-lived gravitational-wave transients coincident with long gamma-ray bursts. *arXiv*, 1309.6160, 2013.

[16] J. Weber. Gravitational radiation. *Phys. Rev. Lett.*, 18(13):498–501, March 1967.

[17] Laser Interferometer Gravitational Wave Observatory. `www.ligo.caltech.edu`.

[18] European Gravitational Observatory. `http://www.ego-gw.it/public/virgo/virgo.aspx`.

[19] J. Aasi et al. Prospects for Localization of Gravitational Wave Transients by the Advanced LIGO and Advanced Virgo Observatories. 2013.

[20] S. Babak, R. Biswas, P.R. Brady, D.A. Brown, K. Cannon, et al. Searching for gravitational waves from binary coalescence. *Phys.Rev.*, D87:024033, 2013.

[21] C. A. K. Robinson, B. S. Sathyaprakash, and Anand S. Sengupta. A geometric algorithm for efficient coincident detection of gravitational waves. *Phys. Rev.*, D78:062002, 2008.

[22] Sukanta Bose, Archana Pai, and Sanjeev V. Dhurandhar. Detection of gravitational waves from inspiraling compact binaries using a network of interferometric detectors. *Int. J. Mod. Phys. D*, 9:325–329, 2000.

[23] Archana Pai, Sanjeev Dhurandhar, and Sukanta Bose. A data-analysis strategy for detecting gravitational-wave signals from inspiraling compact bi-

naries with a network of laser-interferometric detectors. *Phys. Rev. D*, 64:042004, 2001.

[24] Ian Harry and Stephen Fairhurst. A targeted coherent search for gravitational waves from compact binary coalescences. *Phys. Rev. D*, 83:084002, 2011.

[25] Bernard F. Schutz. Networks of gravitational wave detectors and three figures of merit. *Class. Quant. Grav.*, 28:125023, 2011.

[26] S. Klimenko, I. Yakushin, A. Mercer, and G. Mitselmakher. A coherent method for detection of gravitational wave bursts. *Class. Quant. Grav.*, 25:114029, 2008.

[27] Patrick S. Sutton et al. X-Pipeline: an analysis package for autonomous gravitational-wave burst searches. *New Journal of Physics*, 12:122002, 2010.

[28] Drew Keppel. Metrics for multi-detector template placement in searches for short-duration nonprecessing inspiral gravitational-wave signals. *arXiv*, 1307.4158, 2013.

[29] Aaron M. Rogan. *Gravitational wave detection, detector characterization, and parameter estimation using a network of interferometer detectors*. PhD thesis, Washington State University, Pullman, WA, 2006.

[30] Shawn E. Seader. *Multi-interferometer search methods for gravitational waves*. PhD thesis, Washington State University, Pullman, WA, 2005.

[31] Shaon Ghosh. *Improving the detectability of gravitational wave counterparts of Short-hard Gamma Ray Bursts*. PhD thesis, Washington State University, Pullman, WA, 2013.

[32] Dipongkar Talukder. *Multi-baseline searches for stochastic sources and black hole ringdown signals in LIGO-Virgo data*. PhD thesis, Washington State University, Pullman, WA, 2012.

[33] Ian W. Harry. *Can we hear black holes collide?* PhD thesis, Caltech, Cardiff, Wales, United Kingdom, 2011.

[34] Y. Guersel and M. Tinto. Near optimal solution to the inverse problem for gravitational wave bursts. *Phys. Rev.*, D40:3884–3938, 1989.

[35] LSC Algorithms Library. `https://www.lsc-group.phys.uwm.edu/daswg/projects/lalsuite.html`.

[36] Numerical INJection Analysis (NINJA) Project. `https://www.ninja-project.org/doku.php`.

[37] Drew Keppel. *Signatures and dynamics of compact binary coalescences and a search in LIGO's S5 data*. PhD thesis, Caltech, Pasadena, CA, 2009.

[38] Larne Pekowsky. *Characterization of enhanced interferometric gravitational-wave detectors and studies of numeric simulations for compact-binary coalescences*. PhD thesis, Syracuse University, Syracuse, NY, 2011.

[39] L. S. Finn. Detection, measurement, and gravitational radiation. *Physical Review D*, 46(12):5236–5249, December 1992.

[40] Duncan A Brown. *Search for gravitational radiation from black hole MACHOs in the Galactic halo*. PhD thesis, University of Wisconsin–Milwaukee, 2004.

[41] Collin D. Capano. *Searching for gravitational waves from compact binary coalescence using LIGO and Virgo data*. PhD thesis, Syracuse University, Syracuse, NY, 2011.

[42] Benjamin J. Owen. Search templates for gravitational waves from inspiraling binaries: Choice of template spacing. *Phys. Rev. D*, 53:6749–6761, 1996.

[43] Bruce Allen. A chi^2 time-frequency discriminator for gravitational wave detection. *Phys. Rev. D*, 71:062001, 2005.

[44] Luc Blanchet, Thibault Damour, Bala R. Iyer, Clifford M. Will, and Alan. G. Wiseman. Gravitational radiation damping of compact binary systems to second postNewtonian order. *Phys. Rev. Lett.*, 74:3515–3518, 1995.

[45] Luc Blanchet, Bala R. Iyer, Clifford M. Will, and Alan G. Wiseman. Gravitational wave forms from inspiralling compact binaries to second-postNewtonian order. *Class. Quant. Grav.*, 13:575–584, 1996.

[46] P. Jaranowski, A. Krolak, K. D. Kokkotas, and G. Tsegas. On the estimation of parameters of the gravitational-wave signal from a coalescing binary by a network of detectors. *Class. Quant. Grav.*, 13:1279–1307, 1996.

[47] P. Ajith and Sukanta Bose. Estimating the parameters of non-spinning binary black holes using ground-based gravitational-wave detectors: Statistical errors. *Phys. Rev.*, D79:084032, 2009.

[48] Piotr Jaranowski, Andrzej Krolak, and Bernard F. Schutz. Data analysis of gravitational-wave signals from spinning neutron stars. I: The signal and its detection. *Phys. Rev.*, D58:063001, 1998.

[49] Malik Rakhmanov. Rank deficiency and Tikhonov regularization in the inverse problem for gravitational-wave bursts. *Class. Quant. Grav.*, 23:S673–S686, 2006.

[50] S. Klimenko, S. Mohanty, Malik Rakhmanov, and Guenakh Mitselmakher. Constraint likelihood analysis for a network of gravitational wave detectors. *Phys. Rev.*, D72:122002, 2005.

[51] Soumya D. Mohanty, Malik Rakhmanov, Sergei Klimenko, and Guenakh Mitselmakher. Variability of signal to noise ratio and the network analysis of gravitational wave burst signals. *Class. Quant. Grav.*, 23:4799–4810, 2006.

[52] W. H. Press, S. A. Teukolsky, W. T. Vetterling, and B. P. Flannery. *Numerical Recipes 3rd Edition: The Art of Scientific Computing*. Cambridge University Press, 2007.

[53] Gregory M. Harry (for the LIGO Scientific Collaboration). Advanced LIGO: the next generation of gravitational wave detectors. *Class. Quant. Grav.*, 27:084006, 2010.

[54] The Virgo Collaboration. Advanced Virgo Technical Design Report. 2012.

[55] Kentaro Somiya. Detector configuration of KAGRA: The Japanese cryogenic gravitational-wave detector. *Class.Quant.Grav.*, 29:124007, 2012.

[56] Jeffrey M. Silverman and Alexei V. Filippenko. On IC 10 X-1, the Most Massive Known Stellar-Mass Black Hole. *Astrophys.J.*, 678:L17–L20, 2008.

[57] P. A. Crowther et al. NGC 300 X-1 is a Wolf-Rayet/Black-Hole binary. *MN-RAS*, page L11, 2010.

[58] Sean Farrell, Natalie Webb, Didier Barret, Olivier Godet, and Joana Rodrigues. An Intermediate-mass Black Hole of Over 500 Solar Masses in the Galaxy ESO 243-49. *Nature*, 460:73–75, 2009.

[59] J. Abadie et al. Search for gravitational waves from binary black hole inspiral, merger and ringdown. *Phys. Rev.*, D83:122005, 2011.

[60] Sukanta Bose, Shaon Ghosh, and P. Ajith. Systematic errors in measuring parameters of non-spinning compact binary coalescences with post-Newtonian templates. *Class.Quant.Grav.*, 27:114001, 2010.

[61] Benjamin Aylott, John G. Baker, William D. Boggs, Michael Boyle, Patrick R. Brady, et al. Testing gravitational-wave searches with numerical relativity waveforms: Results from the first Numerical INJection Analysis (NINJA) project. *Class.Quant.Grav.*, 26:165008, 2009.

[62] P. Ajith et al. The NINJA-2 catalog of hybrid post-Newtonian/numerical-relativity waveforms for non-precessing black-hole binaries . *Class. Quant. Grav.*, 29:124001, 2012.

[63] Alessandra Buonanno, Yi Pan, John G. Baker, Joan Centrella, Bernard J. Kelly, et al. Toward faithful templates for non-spinning binary black holes using the effective-one-body approach. *Phys.Rev.*, D76:104049, 2007.

[64] P. Ajith et al. Addendum to 'The NINJA-2 catalog of hybrid post-Newtonian/numerical-relativity waveforms for non-precessing black-hole binaries'. *Class. Quant. Grav.*, 30:199401, 2013.

[65] D. Talukder, S. Bose, S. Caudill, and P. Baker. Improved Coincident and Coherent Detection Statistics for Searches for Gravitational Wave Ringdown Signals. *arXiv*, 1310.2341, 2013.

[66] N. Arnaud et al. Coincidence and coherent data analysis methods for gravitational wave bursts in a network of interferometric detectors. *Phys. Rev. D*, 68:102001, 2003.

[67] S. Klimenko et al. Localization of gravitational wave sources with networks of advanced detectors . *Phys. Rev. D*, 83:102001, 2011.

[68] Alessandra Buonanno and Thibault Damour. Transition from inspiral to plunge in binary black hole coalescences. *Phys. Rev. D.*, 62:064015, 2000.

[69] The LIGO Scientific The NINJA-2 and The Virgo collaborations. The NINJA-2 Blind Injection Challenge, in preparation. 2013.

[70] Mark Hannam, Sascha Husa, Frank Ohme, and P. Ajith. Length requirements for numerical-relativity waveforms. *Phys.Rev.*, D82:124052, 2010.

[71] Michael Boyle. Uncertainty in hybrid gravitational waveforms: Optimizing initial orbital frequencies for binary black-hole simulations. *Phys.Rev.*, D84:064013, 2011.

[72] Sebastiano Bernuzzi, Marcus Thierfelder, and Bernd Bruegmann. Accuracy of numerical relativity waveforms from binary neutron star mergers and their comparison with post-Newtonian waveforms. *Phys.Rev.*, D85:104030, 2012.

[73] Ilana MacDonald, Samaya Nissanke, and Harald P. Pfeiffer. Suitability of post-Newtonian/numerical-relativity hybrid waveforms for gravitational wave detectors. *Class.Quant.Grav.*, 28:134002, 2011.

[74] Frank Ohme, Alex B. Nielsen, Drew Keppel, and Andrew Lundgren. Statistical and systematic errors for gravitational-wave inspiral signals: A principal component analysis. 2013.

[75] J. Abadie et al. Predictions for the Rates of Compact Binary Coalescences Observable by Ground-based Gravitational-wave Detectors. *Class.Quant.Grav.*, 27:173001, 2010.

[76] P. Ajith et al. A template bank for gravitational waveforms from coalescing binary black holes: non-spinning binaries. *Phys. Rev. D*, 77:104017, 2008.

[77] Michael Boyle, Duncan A. Brown, Lawrence E. Kidder, Abdul H. Mroue, Harald P. Pfeiffer, et al. High-accuracy comparison of numerical relativity simulations with post-Newtonian expansions. *Phys. Rev.*, D76:124038, 2007.

[78] Wolfgang Tichy and Pedro Marronetti. A Simple method to set up low eccentricity initial data for moving puncture simulations. *Phys. Rev.*, D83:024012, 2011.

[79] Bernd Bruegmann, Jose A. Gonzalez, Mark Hannam, Sascha Husa, Ulrich Sperhake, and Wolfgang Tichy. Calibration of Moving Puncture Simulations. *Phys. Rev.*, D77:024027, 2008.

[80] Pedro Marronetti, Wolfgang Tichy, Bernd Bruegmann, Jose A. Gonzalez, Mark Hannam, Sascha Husa, and Ulrich Sperhake. Binary black holes on a budget: Simulations using workstations. *Class.Quant.Grav.*, 24:S43–S58, 2007.

[81] Bernd Bruegmann, Wolfgang Tichy, and Nina Jansen. Numerical simulation of orbiting black holes. *Phys.Rev.Lett.*, 92:211101, 2004.

[82] James Healy, Frank Herrmann, Ian Hinder, Deirdre M. Shoemaker, Pablo Laguna, and Richard A. Matzner. Superkicks in Hyperbolic Encounters of Binary Black Holes. *Phys.Rev.Lett.*, 102:041101, 2009.

[83] James Healy, Pablo Laguna, Richard A. Matzner, and Deirdre M. Shoemaker. Final Mass and Spin of Merged Black Holes and the Golden Black Hole. *Phys. Rev.*, D81:081501, 2010.

[84] Tanja Bode, Roland Haas, Tamara Bogdanovic, Pablo Laguna, and Deirdre Shoemaker. Relativistic Mergers of Supermassive Black Holes and their Electromagnetic Signatures. *Astrophys. J.*, 715:1117–1131, 2010.

[85] Frank Herrmann, Ian Hinder, Deirdre M. Shoemaker, Pablo Laguna, and Richard A. Matzner. Binary Black Holes: Spin Dynamics and Gravitational Recoil. *Phys. Rev.*, D76:084032, 2007.

[86] James Healy, Janna Levin, and Deirdre Shoemaker. Zoom-Whirl Orbits in Black Hole Binaries. *Phys. Rev. Lett.*, 103:131101, 2009.

[87] Tanja Bode, Tamara Bogdanovic, Roland Haas, James Healy, Pablo Laguna, et al. Mergers of Supermassive Black Holes in Astrophysical Environments. *Astrophys. J.*, 744:45, 2012.

[88] Ian Hinder, Birjoo Vaishnav, Frank Herrmann, Deirdre Shoemaker, and Pablo Laguna. Universality and final spin in eccentric binary black hole inspirals. *Phys. Rev.*, D77:081502, 2008.

[89] Sascha Husa, José A. Gonzalez, Mark Hannam, Bernd Brügmann, and Ulrich Sperhake. Reducing phase error in long numerical binary black hole evolutions with sixth order finite differencing. *Class. Quantum Grav.*, 25:105006, 2008.

[90] Mark Hannam, Sascha Husa, Bernd Bruegmann, and Achamveedu Gopakumar. Comparison between numerical-relativity and post-Newtonian waveforms from spinning binaries: the orbital hang-up case. *Phys. Rev.*, D78:104007, 2008.

[91] P. Ajith, M. Hannam, S. Husa, Y. Chen, B. Bruegmann, et al. Inspiral-merger-ringdown waveforms for black-hole binaries with non-precessing spins. *Phys. Rev. Lett.*, 106:241101, 2011.

[92] Mark Hannam, Sascha Husa, Frank Ohme, Doreen Muller, and Bernd Bruegmann. Simulations of black-hole binaries with unequal masses or

nonprecessing spins: Accuracy, physical properties, and comparison with post-Newtonian results. *Phys. Rev.*, D82:124008, 2010.

[93] Bernd Brügmann et al. Calibration of Moving Puncture Simulations. *Phys. Rev.*, D77:024027, 2008.

[94] Mark Hannam, Sascha Husa, Ulrich Sperhake, Bernd Brugmann, and Jose A. Gonzalez. Where post-Newtonian and numerical-relativity waveforms meet. *Phys. Rev.*, D77:044020, 2008.

[95] Ulrich Sperhake. Binary black-hole evolutions of excision and puncture data. *Phys. Rev.*, D76:104015, 2007.

[96] Ulrich Sperhake et al. Eccentric binary black-hole mergers: The transition from inspiral to plunge in general relativity. *Phys. Rev.*, D78:064069, 2008.

[97] Denis Pollney and Christian Reisswig. Gravitational memory in binary black hole mergers. *Astrophys. J.*, 732:L13, 2011.

[98] C. Reisswig, N. T. Bishop, D. Pollney, and B. Szilagyi. Characteristic extraction in numerical relativity: binary black hole merger waveforms at null infinity. *Class. Quantum Grav.*, 27:075014, 2010.

[99] Denis Pollney, Christian Reisswig, Erik Schnetter, Nils Dorband, and Peter Diener. High accuracy binary black hole simulations with an extended wave zone. *Phys. Rev.*, D83:044045, 2011.

[100] Manuela Campanelli, C. O. Lousto, P. Marronetti, and Y. Zlochower. Accu-

rate evolutions of orbiting black-hole binaries without excision. *Phys. Rev. Lett.*, 96:111101, 2006.

[101] Carlos O. Lousto, Hiroyuki Nakano, Yosef Zlochower, and Manuela Campanelli. Intermediate Mass Ratio Black Hole Binaries: Numerical Relativity meets Perturbation Theory. *Phys. Rev. Lett.*, 104:211101, 2010.

[102] Carlos O. Lousto, Hiroyuki Nakano, Yosef Zlochower, and Manuela Campanelli. Intermediate-mass-ratio black hole binaries: intertwining numerical and perturbative techniques. *Phys. Rev.*, D82:104057, 2010.

[103] Hiroyuki Nakano, Yosef Zlochower, Carlos O. Lousto, and Manuela Campanelli. Intermediate-mass-ratio black hole binaries II: Modeling Trajectories and Gravitational Waveforms. *Phys. Rev.*, D84:124006, 2011.

[104] Harald P. Pfeiffer, Lawrence E. Kidder, Mark A. Scheel, and Saul A. Teukolsky. A Multidomain spectral method for solving elliptic equations. *Comput. Phys. Commun.*, 152:253–273, 2003.

[105] Mark A. Scheel et al. Solving Einstein's equations with dual coordinate frames. *Phys. Rev.*, D74:104006, 2006.

[106] Geoffrey Lovelace, Michael Boyle, Mark A. Scheel, and Bela Szilagyi. High-accuracy gravitational waveforms for binary-black-hole mergers with nearly extremal spins. *Class. Quantum Grav.*, 29:045003, 2012.

[107] Bela Szilagyi, Lee Lindblom, and Mark A. Scheel. Simulations of Binary Black Hole Mergers Using Spectral Methods. *Phys. Rev.*, D80:124010, 2009.

[108] Geoffrey Lovelace, Mark. A. Scheel, and Bela Szilagyi. Simulating merging binary black holes with nearly extremal spins. *Phys. Rev.*, D83:024010, 2011.

[109] Mark A. Scheel, Michael Boyle, Tony Chu, Lawrence E. Kidder, Keith D. Matthews, and Harald P. Pfeiffer. High-accuracy waveforms for binary black hole inspiral, merger, and ringdown. *Phys. Rev.*, D79:024003, 2009.

[110] Spectral Einstein Code. `http://www.black-holes.org/SpEC.html`.

[111] Lee Lindblom, Mark A. Scheel, Lawrence E. Kidder, Robert Owen, and Oliver Rinne. A New Generalized Harmonic Evolution System. *Class. Quantum Grav.*, 23:S447–S462, 2006.

[112] Michael Boyle and Abdul H. Mroue. Extrapolating gravitational-wave data from numerical simulations. *Phys. Rev.*, D80:124045, 2009.

[113] Z. B. Etienne, Y. T. Liu, S. L. Shapiro, and T. W. Baumgarte. General relativistic simulations of black-hole-neutron-star mergers: Effects of black-hole spin. *Phys. Rev.*, D79(4):044024, February 2009.

[114] Yi Pan et al. Inspiral-merger-ringdown waveforms of spinning, precessing black-hole binaries in the effective-one-body formalism. *arXiv*, 1307.6232, 2013.

[115] Parameswaran Ajith et al. Phenomenological template family for black-hole coalescence waveforms. *Class. Quant. Grav.*, 24:S689–S699, 2007.

[116] P. Ajith, P. Fotopoulos, S. Privitera, A. Neunzert, and A.J. Weinstein. An effectual template bank for the detection of gravitational waves from inspiralling compact binaries with generic spins. 2012.

[117] S. Privitera et al. Improving the sensitivity of a search for coalescing binary black holes with non-precessing spins in gravitational wave data. *arXiv*, 1310.5633, 2013.

[118] T. Dayanga and S. Bose. Preparations for detecting and characterizing gravitational-wave signals from binary black hole coalescences. *arXiv*, 1311.4986, 2013.